INVESTIGATION OF VIBRATION BASED FAULT DETECTION METHODS FOR SPINDLE BEARINGS

A THESIS SUBMITTED TO
THE GRADUATE SCHOOL OF NATURAL AND APPLIED SCIENCES
OF
MIDDLE EAST TECHNICAL UNIVERSITY

BY

MERT KARAKAŞ

IN PARTIAL FULFILLMENT OF THE REQUIREMENTS
FOR
THE DEGREE OF MASTER OF SCIENCE
IN
MECHANICAL ENGINEERING

DECEMBER 2022

Approval of the thesis:

INVESTIGATION OF VIBRATION BASED FAULT DETECTION METHODS FOR SPINDLE BEARINGS

submitted by **MERT KARAKAŞ** in partial fulfillment of the requirements for the degree of **Master of Science** i**n Mechanical Engineering, Middle East Technical University** by,

Prof. Dr. Halil Kalıpçılar
Dean, Graduate School of **Natural and Applied Sciences** _____

Prof. Dr. Sahir Arıkan
Head of the Department, **Mechanical Engineering** _____

Assist. Prof. Dr. Orkun Özşahin
Supervisor, **Mechanical Engineering, METU** _____

Examining Committee Members:

Assoc. Prof. Dr. Mehmet Bülent Özer
Mechanical Engineering, METU _____

Assist. Prof. Dr. Orkun Özşahin
Mechanical Engineering, METU _____

Assist. Prof. Dr. Hakan Çalışkan
Mechanical Engineering, METU _____

Assist. Prof. Dr. Gökhan Özgen
Mechanical Engineering, METU _____

Assist. Prof. Dr. Samet Akar
Mechanical Engineering, Çankaya Uni. _____

Date: 06.12.2022

I hereby declare that all information in this document has been obtained and presented in accordance with academic rules and ethical conduct. I also declare that, as required by these rules and conduct, I have fully cited and referenced all material and results that are not original to this work.

Name Last name : Karakaş Mert

Signature :

ABSTRACT

INVESTIGATION OF VIBRATION BASED FAULT DETECTION METHODS FOR SPINDLE BEARINGS

Karakaş, Mert
Master of Science, Mechanical Engineering
Supervisor : Assist. Prof. Dr. Orkun Özşahin

December 2022, 123 pages

Spindles are hearth of the CNC lathes and condition of them are critical for the industry. In this thesis, effects of bearing defect on spindles are investigated and condition of spindles are determined using vibration data collected at working conditions. After a comprehensive literature survey, a bearing model including effects of defects is constructed. Afterwards, a finite element model of a spindle is created, and outputs of the bearing model are used as inputs for the FEM. Using the model, effects of bearing defects on point FRF of spindle and tool point FRF are observed. Results are compared with the experiment done on a spindle before and after maintenance. In addition, vibration data measured from five different spindles at different working conditions are analyzed in detail for detecting bearing defects alongside with the common shaft faults.

Keywords: Fault Detection, Condition Monitoring, Bearing Defect

ÖZ

SPINDLE RULMANLARI İÇİN TİTREŞİM TABANLI HATA TESPİT YÖNTEMLERİNİN ARAŞTIRILMASI

Karakaş, Mert
Yüksek Lisans, Makina Mühendisliği
Tez Yöneticisi: Assist. Prof. Dr. Orkun Özşahin

Aralık 2022, 123 sayfa

İş milleri CNC tezgahlarının en önemli kısımlarından biridir ve durumları endüstri için kritiktir. Bu tezde rulman arızalarının iş milleri üzerindeki etkisi incelenmiştir. Bununla birlikte, çalışma koşullarına toplanmış titreşim verisi kullanılarak iş millerinin durumunun belirlenmesi üzerine çalışılmıştır. Kapsamlı bir kaynak araştırmasının ardından, arızaların etkisini de içeren bir rulman modeli oluşturulmuştur. Ardından bir iş milinin sonlu elemanlar modeli oluşturulmuştur ve bu modelde rulman modelinin çıktıları da kullanılmıştır. Rulman arızalarının iş milinin frekans davranış fonksiyonu ve kesici uç noktası frekans davranış fonksiyonu üzerine etkileri gözlemlenmiştir. Sonuçlar bakım öncesi ve sonrası yapılan deneylerle karşılaştırılmıştır. Bunların yanında, beş farklı iş milinden çalışma koşullarında toplanan titreşim verisi kullanılarak rulman hatalarının ve diğer sık karşılaşılan mil hatalarının belirlenmesi için ayrıntılı bir analiz gerçekleştirilmiştir.

Anahtar Kelimeler: Hata bulma, Durum İzleme, Rulman Arızası

To My Beloved Family

ACKNOWLEDGMENTS

I wish to express my deepest gratitude to Assist. Prof. Dr. Orkun Özşahin for his, encouragements ,advice, criticism, guidance , and insight throughout the research.

I want to thank Dr. Şükrü Doruk Merdol for his suggestions and comments. I also want to thank Senkronize Professional Spindle Service for hosting me and letting me to be a part of spindle maintenance and conduct experiments.

TABLE OF CONTENTS

LIST OF TABLES

TABLES

LIST OF FIGURES

FIGURES

LIST OF ABBREVIATIONS

ABBREVIATIONS

CNC	Computer Numerical Control
FFT	Fast Fourier Transform
FMEA	Failure Mode Effects and Critically Analysis
RPM	Revolution per minute
Hz	Hertz
FEM	Finite Element Method
RMS	Root Mean Square
ISO	International Organization for Standardization
WT	Wavelet Transform
CWT	Continuous Wavelet Transform
FRF	Frequency Response Function
FTF	Fundamental Train Frequency
BPFO	Ball Passing Frequency Outer Race
BPFI	Ball Passing Frequency Inner Race
BSF	Ball Spin Frequency
DOF	Degrees of Freedom
HRS	Harmonics of Rotational Speed

LIST OF SYMBOLS

SYMBOL	
δ	Deformation
Q	Normal Load
K	Equivalent Contact Stiffness
δ_i	Deformation At the Ball-Inner Race Interface
δ_o	Deformation At the Ball-Outer Race Interface
K_i	Contact Stiffness at the Ball-Inner Race Interface
K_o	Contact Stiffness at the Ball-Outer Race Interface
r_i	Inner Radii of Raceway Groove Curvature
r_o	Outer Radii of Raceway Groove Curvature
d_m	Pitch Diameter
α	Contact Angle
$\sum\rho_i$	Curvature Sum of Inner Race
$\sum\rho_o$	Curvature Sum of Outer Race
$F(\rho)_i$	Inner Race Curvature Difference
$F(\rho)_o$	Outer Race Curvature Difference
ξ_1, ξ_2	Poisson's Ratio
E_1, E_2	Young's Modulus
q	Relative Displacement
h	Depth of Defect
R_o	Outer Race Radius

r_b Radius of the Ball

δ_j Contact Deformation

A_0 Relative Distances Between Groove Curvature Centers of Inner and Outer Races at the Unloaded Condition

A Relative Distances Between Groove Curvature Centers of Inner and Outer Races at the Loaded Condition

r_L Radial Clearance

r_d Distance of Inner Race Groove Curvature Center in Radial Direction

K_{xx} Stiffness at x Direction

K_{yy} Stiffness at y Direction

K_{zz} Stiffness at z Direction

$K_{\theta x\theta x}$ Rotational Stiffness around x Axis

$K_{\theta y\theta y}$ Rotational Stiffness around y Axis

CHAPTER 1

INTRODUCTION

1.1 Literature Review

Demands of industry from computer numerical control (CNC) machines are increasing every passing day. Increasing need of high precision-quality, low-cost products, and safe production pushes machine maintenance strategy from corrective over preventive via condition monitoring [1]

Faults at the beginning stage should be monitored, as it advances from minor to major defect, until it requires a maintenance action. The condition of a machine, component, part, or a system can be monitored, and the certain happening of failure can be avoided, providing zero downtime performance.

Tse et al.[2] illustrates trend of amplitude of vibration versus time as in Figure 1.1. Planned maintenance prevents breakdown of a machine, but it is not as efficient as maintenance at the right time. Maintenance at right time can be achieved with condition-based maintenance.

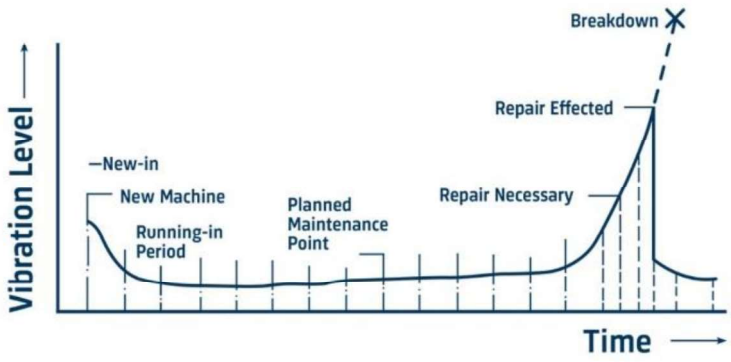

Figure 1.1 Trend of Vibration Signals Showing the Rate of Deterioration of a Machine [3]

Concepts of diagnostics and prognostics are originated from medical area. Diagnostics is conducted to analyze the reason of a situation or problem. Prognostics is interested with calculating the future considering the rational study of the permanent data. Diagnostics is the action of detecting a failure mode while prognostics is action of making a logical estimation of remaining useful life. Prognostics is simply to monitor and detect the beginning of a failure in a component to be able to make meaningful predictions [4].

The first step of constructing a condition monitoring system is to identify the critical subsystems. The purpose of this procedure is to determine which subsystem or component has the highest effect on system from the point of view of performance and downtime cost. Creating a four-quadrant chart (Figure 1.2) is one of tools to identify critical subsystems and components of a system. Four quadrant chart demonstrates the average downtime versus frequency of failure. The two lines dividing the chart horizontally and vertically creating four quadrants are determined by used according to their need on production and maintenance. In Figure 1.2, Quadrant 1 contains the subsystems and components which fail frequently and cause significant downtime. Normally there shouldn't be any component at this region since such conditions should be notices and fixed at design stage. However, reasons like manufacturing faults, wrong use or installation, improper environmental conditions may result in frequent and long downtime. Quadrant 2 is consisted of subsystems and components that has high failure rate but low downtime cost. Standard maintenance strategy is to have spare parts for this type of components. Quadrant 3 is consisted of ow frequency of failure and low downtime cost which means that maintenance strategy is working for them, and no change is needed. Quadrant 4 is consisted of the most critical subsystems and components. Their failure is rare, but downtime is long. For subsystems and components like these, prognostics and condition monitoring should be applied [5].

Spindle is a system in the quadrant 4 since failure of the spindle is rare but generally downtime is long. Quadrants and example machine parts can be seen from Figure 1.2.

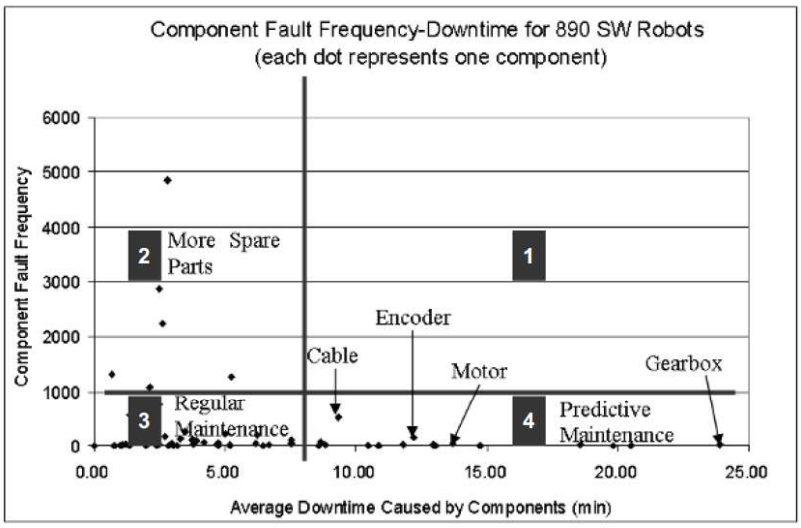

Figure 1.2 Chart for Detecting Sensitive Components [5]

Thoppil et al. [6] puts forward that spindle is the most critical part among subsystems of a CNC machine tool. Failure mode effects and critically analysis (FMEA)done by them concludes that spindle is by far most critical subsystem of a CNC lathe and bearings of a spindle is the most critical CNC lathe component.

According to FMEA done by Chen et. al [7] spindle is the most critical component followed by encoder, disc spring and solenoid valve. Therefore, fault detection and condition monitoring of bearings is the key section of health assessment of a spindle.

The spindle must transfer torque and power, provide high rotational speed to the tool during its lifetime continuously. Constant forces cause most of the breakdowns in the spindles components which the bearings are one of the most critical and vital ones. Faults are generally developed because of irregularities on the radial and axial loads, lack of lubrication, vibration, high temperature etc. [8].

1.1.1 Modeling of Bearing Dynamics Including the Effects of Defects

A bearing one of the most used mechanical parts of machines. It is used for limiting motion of two different bodies to designed motion and decreasing friction between two rotating parts. Rolling element bearings are extensively used in rotating

machinery and has a critical role in them, such as spindles, gearboxes, railways, wind turbines. Different type of bearings has been preferred at different industries according to their advantages among others. Angular contact ball bearings (Figure 1.3) that encounter trust load at only one direction, are commonly used at spindles. Angular contact ball bearings can handle high radial forces and single direction axial forces at the same time at high rotational speed.

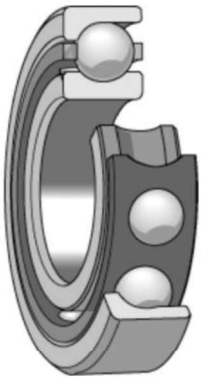

Figure 1.3 Angular Contact Ball Bearing [9]

The fundamental components of the angular contact ball bearings are balls, inner-outer rings and a cage and can be seen from Figure 1.3. Surfaces that touches the balls are raceways. In order to carry the axial load at one direction, races touch balls with a contact angle and this angle can be seen from Figure 1.4. As this contact angle increases, axial load carrying capacity of the bearing also increases but at the same time speed and operational life decreases so a decision must be made selecting the angle of the bearing [10].

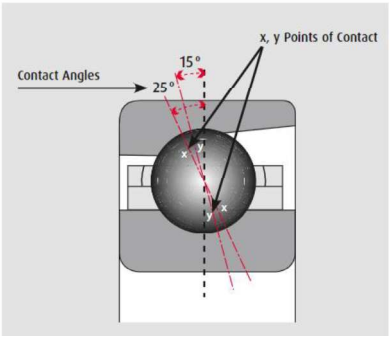

Figure 1.4 Cross-section of an Angular Contact Ball Bearing and Contact Angle[10]

The bearing is a fundamental element of rotating machines. A failure at the bearing most of the time leads to failure of the machine so reliability of this machine element is important. During operation bearings overcome high forces generated by machines. Thus, condition of bearings is a critical information. Any defect arises must be identified to avoid failure of the machine, increase downtime and production. These defects can be separated into two: distributed defects and local defects [11].

Distributed defects are mainly waviness, misaligned races, surface roughness, uneven balls, and rollers. These kinds of defects are generally result of abrasive wear, improper manufacturing, and installation. Figure 1.5 shows an example for waviness defect. The contact force between elements of the bearing varies during the operation resulting vibration. This vibration can be detected with the help of condition monitoring techniques.

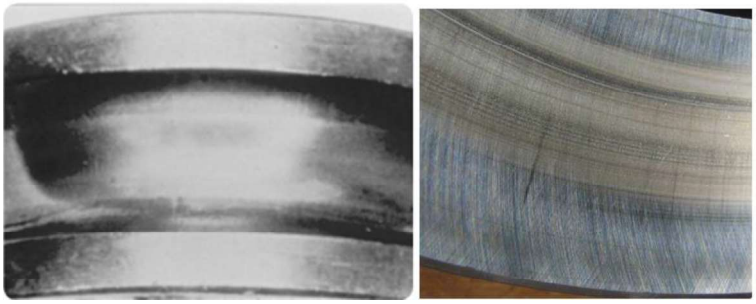

Figure 1.5 Waviness at races [12]

Local defects do not cover a surface but instead they appear as a discontinuity at a surface. Metal to metal contact occurring between races and rolling elements generates stress at the contact area. Cyclic stress at the material causes fatigue. It should be noted that, even in the good condition where bearing faces no contamination, cyclic stress acting on the surfaces of races and rolling elements can be high enough to cause fatigue. Overloading or shock loading accelerates fatigue failure seriously.

A crack begins below the surface generally result of fatigue and propagates through the surface until a small part of a material breaks off and creates a localized defect.

This type of defect s called spalling. Figure 1.6 shows a typical spalling reasoning from an indentation in a deep grove ball bearing. Another spalling starting at the back of the V shape can be seen . 90% of bearing defects are localized defects that occur at raceways or balls result of localized defects [11].

Figure 1.6 Spalling [12]

There are different methods to determine the stiffness matrix of a bearing. These methods can be analytical, finite element, experimental. Determining stiffness of defected bearings are established on these methods.

Hernot [13] and Lim [14] both finds loads and moments as a function of rotation and displacement. Loads-deflection relation acting on every ball is summed to get loads and moments. Afterwards calculated load and moment formulas are rewritten depending on three displacements and two rotations which can be seen from Figure 1.7. Hernot et al. [13] presented 2 DOF analytical model, and applications of it. Subsequently, stiffness matrix associated to 5 DOF model is given. Lim et al, [14] proposed a compressive stiffness matrix of dimension 6 that bearing preload and bearing type are included. It should be noted that coefficients related to the free rotation of the bearing are all zero at the stiffness matrix proposed by Lim et al. [14].

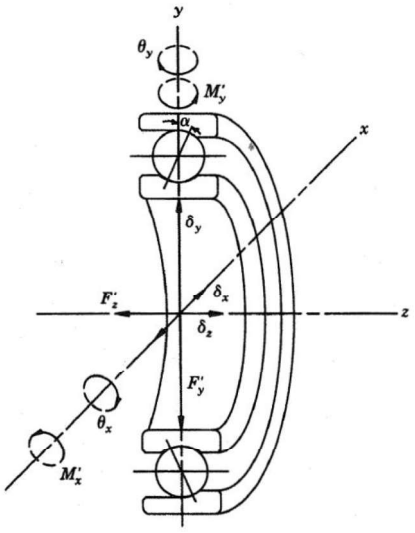

Figure 1.7 Coordinate System Associated with 5 DOF model [9]

Aini et al. [15] derived equations for spindle in a grinding machine. System is modeled using an axle, two bearings and grinding wheel. Equations involve mass moments of inertia and mass forces of the grinding wheel and axel as well as loads and moments on the bearings.

Kang et al.[16] introduced a model using neural networks. Stiffness data of a bearing subjected to different loads is used as training points of the model. New data is obtained by using proper weighting functions and training points. The biggest drawback of this method is that it can only be used if there is data available.

Yi Guo et al. [17] proposed a finite element and contact mechanism model for bearings using contact algorithm for elastic bodies. Contact which is dependent to load, between races and balls all over the bearing is solved. The model includes critical bearing details as well as basic geometric details, for instance, race and rolling element crowning, clearance, race thickness and width, raceway shoulder. It has shown that these parameters affect the bearing stiffness significantly. A section view from finite element model can be seen from Figure 1.8. Using finite element model, the stiffness values of rolling element bearings are determined, and an iteration scheme is proposed without knowing the solution. The method is validated with experimental results from literature and compared against published models.

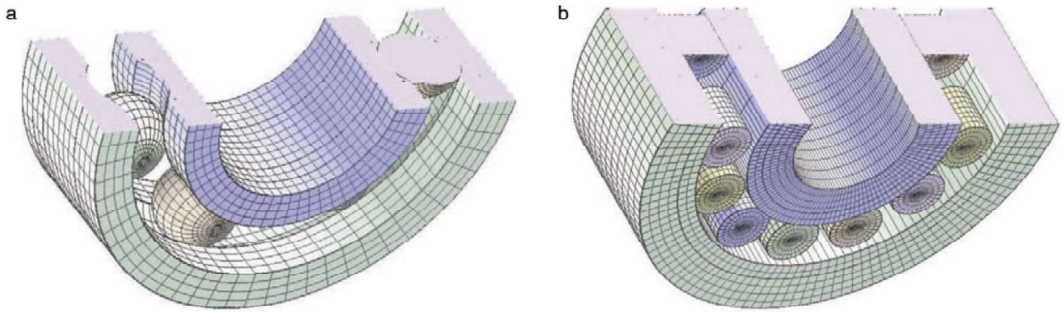

Figure 1.8 Section View of a Ball Bearing and a Double Row Cylindrical Bearing [17]

Petersen et al. [18] presented an analytical formulation of the varying stiffness of an angular contact ball bearing with an outer race defect of varying size. Static load is applied to the bearing at 5 degrees of freedom which can be seen form Figure 1.9. In the model, the moment at the free degree of freedom of the ball bearing is not considered. Defect is defined as a variable at the analytical formulations and effect of change of defect size on the load distribution and varying stiffness of the bearing is studied. The model developed by Petersen et al. [19] considers a square shaped defect at the outer race at the load zone and they showed that as defect size increases, balls at the defect-free region caries more load since balls at the defected region, completely or partially, lose contact with the race. Analysis further indicates that when defect is present or as defect size increases, the radial stiffness decreases at the loaded and axial directions, whereas increases at the unloaded radial direction. It is also stated that, the stiffness changes while a ball passing through the defect zone are substantially larger than the defect free bearing. These stiffness variations generate excitations that can be seen from frequency response.

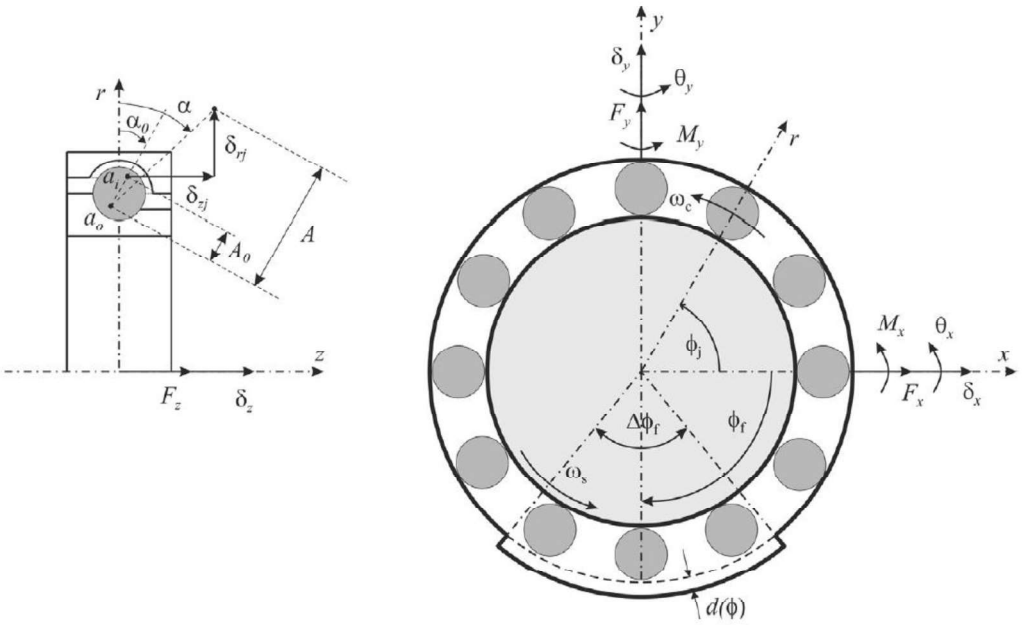

Figure 1.9 Diagram Showing Coordinate System of The Bearing [18]

Hongyang Xu et al. [19] presented a calculation method of radial stiffness of cylindrical roller bearings considering the flexibility of the balls and races. To do that, analytical model and finite element model are used together. Localized defects are modeled as displacement excitations in order to calculate the defected cylindrical roller bearings. Influence of different angles of local defect width to the varying stiffness is also presented.

Jing liu et al. [20] proposed a new defect model that relates force and deflection different than Hertzian force-deflection relation. Effect of defect size on stiffness and on the vibrations are studied using the proposed model. Defect size is altered not only in one direction, instead effect of changes at length, width, depth, and their combinations are studied and some of defect geometries can be seen. Kurtosis and RMS is used to determine the effect of defect at the surface to the response of the deep groove ball bearing. Jing liu et al. [20] showed that, proposed models outer race ball passing frequency prediction is consistent with experiment.

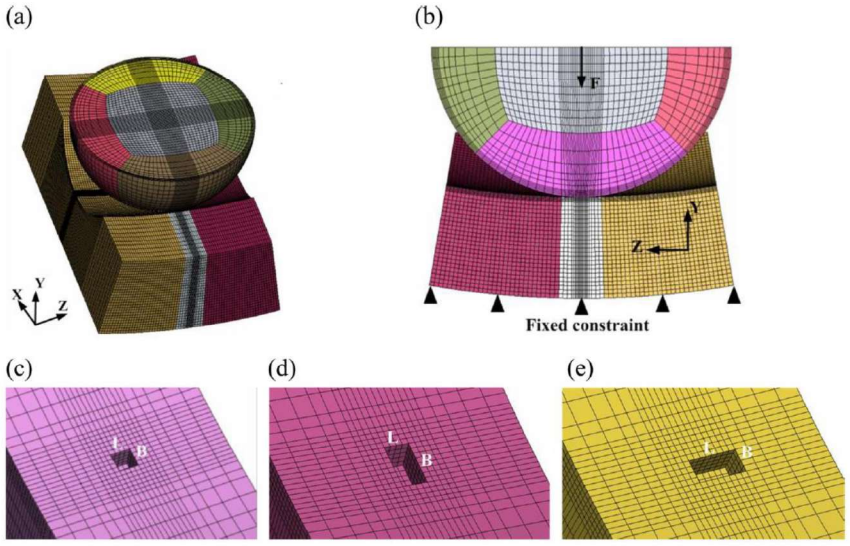

Figure 1.10 Finite Element Model Visuals of Ball, Race and Different Defects at Outer Race [20]

Petersen et al. [21] suggested a method for examining the load distribution and varying stiffness for a loaded doble row rolling element bearing which is radially loaded and has a defect at the outer race. Analysis showed that the balls positioned at the outside of the defect exposed to increased load compared to defect free bearing. Analysis also showed that at the loading direction stiffness decreases but at the unloaded region it increases. Stiffness changes cause parametric excitations of the bearing that effects frequency response. Sudden stiffness variations that happen at the sharp defect exit, creates impulsive events in the response. Slow stiffness changes reasoned waviness of long spall create low frequency parametric excitations. This low frequency response is better seen at velocity spectra.

1.1.2 Modeling of Spindle-Bearing Assembly Dynamics

A typical bearing system is consisting of two sets of bearings, generally angular contact ball bearings, attached to the motorized shaft with a cutting tool attached at the end. Dynamics of the spindle-bearing assembly can be obtained using FEM ([22][23][24][25][26][27]), analytical models [15][28][29][30][31][32]) or experimental methods ([33]) such as model testing. Results can b1e used to predict

the response of the system to ext1ernal loads[34]. A great number of studies have investigated characteristics of spindle, some of them are done in the name under rotor-bearing systems for generality, experimentally and theoretically will be explained.[35]

Aini et al. [15] propounded a five degree of freedom spindle model which are two radials, axial, yawning and pitching. This work let the study of different loading cases. Tandon et al. [28] added sixth degree of freedom by adding waviness of inner race, outer race, and balls. Effects of load dependent and independent components of moments because of friction to the angular ball bearings supported by a rigid shaft is also examined.

Chang et el. [22] proposed a finite element model of a spindle system and compared the model with experiments. Radial and tilting spring-dashpot couples are used at the model which can be seen from Figure 1.11. The model showed that tilting has important effect on higher-order modes of the system. Parameters considered are bearing spacings, preloads, mass inserts on the shaft and damping and it is shown that performance improvements can be done by adjusting these parameters.

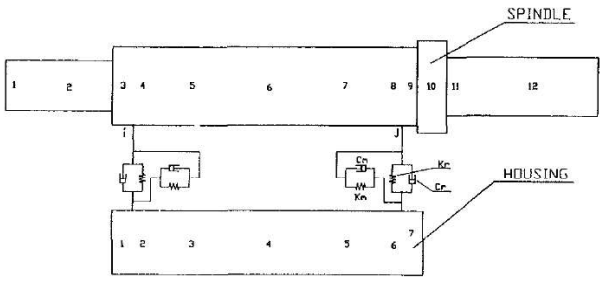

Figure 1.11 Finite Element Model of the Spindle System [22]

Jiang et al. [29] put forward a double-shaft model for analyzing relations between drawbar-shaft bearings. Quasi-static bearing model which includes gyroscopic effects and centrifugal forces is used of modeling the effect of bearings. The double-shaft model can be seen from Figure 1.12. The hollow shaft that carries motor rotor and encapsulates drawbar, and drawbar are divided into lumped masses, motor-rotor

is modeled as a rigid disk. The effects of preload of bearings to the whole system is also investigated.

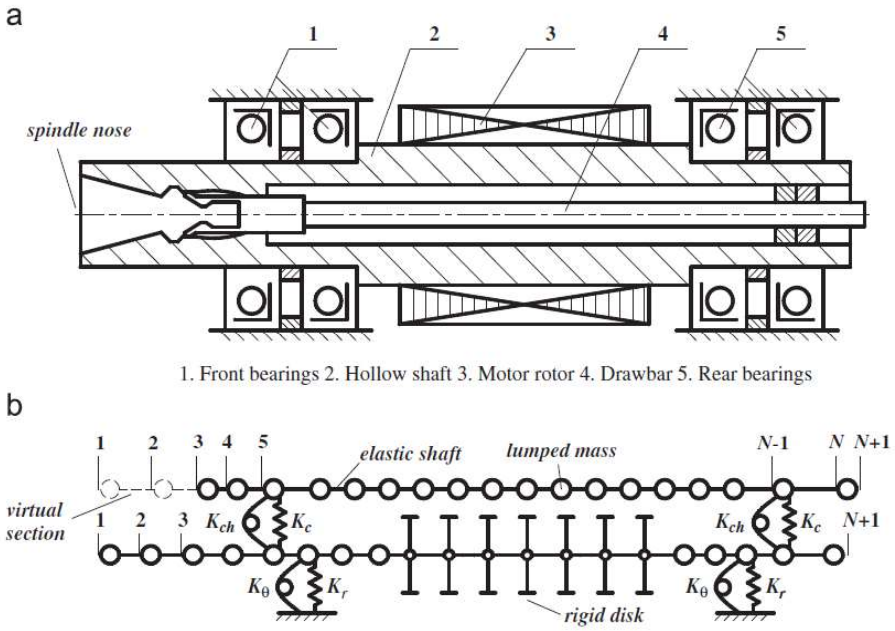

Figure 1.12 The Double-Shaft Spindle Model [29]

Shin et al. [36] presented a coupled bearing-spindle system model which can be solved numerically. In this study, dynamics of spindle is modeled using the influence coefficient method of lumped masses. In addition, rotational and linear bearing stiffnesses are included in the developed model. The parameters of total load, cutting speed and rotational speed of the spindle are analyzed and effect of these parameters to natural frequencies are discussed. Results of analysis are compared with experimental data and an excellent agreement is presented.

Shin et al. [23] also presented a thermos-dynamic model for spindles. With the help of a finite element perspective, a thermal model is generated which can calculate temperature distribution of high-speed motorized spindles. Heat sources and sinks at a typical motorized spindle can be seen from Figure 1.13. The thermal dimensional changes of housing, shaft and bearings are considered and bearing preloads are recalculated depending on the working conditions.

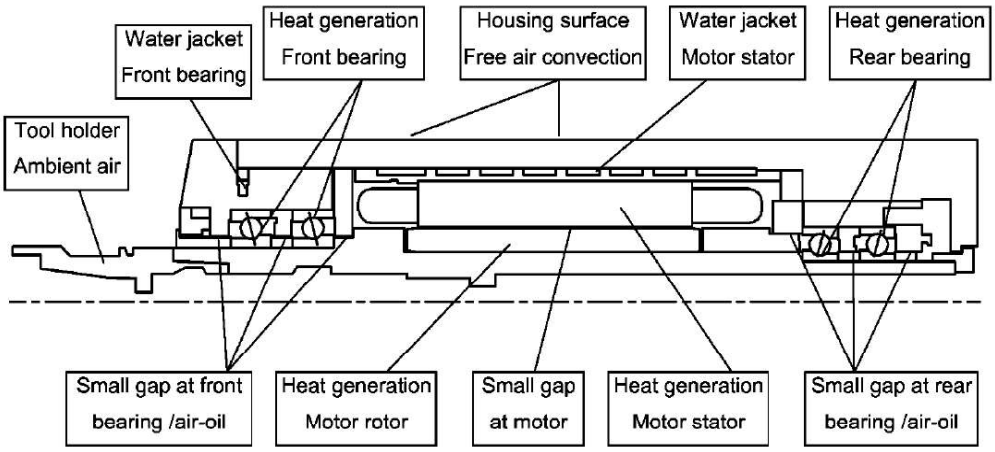

Figure 1.13 Heat Sinks and Sources of a Motorized Spindle [23]

Cao et al.[24] presents an integrated model of spindle consisting of angular contact ball bearings, a shaft, tool holder, housing, and machine tool mounting. The proposed model calculates the stiffnesses of bearings, mode shapes and frequency response function, deflections at cutter and shaft, contact forces at the bearings result of cutting forces. They [24] showed that predictions give better results when all the spindle elements and mounting are considered at the model. Spindle elements included at finite element model can be seen from Figure 1.14. In addition, it is shown that working conditions of the spindle like rotational speed, bearing preload, cutting conditions and material which is being cut effects the vibrations [24].

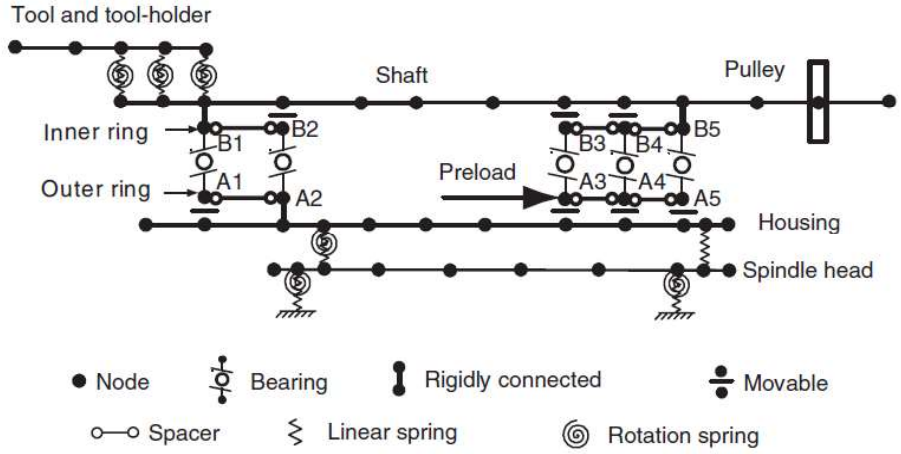

Figure 1.14 Finite Element Model of The Spindle [24]

Hongrui Cao et al. [25] proposed a method that updates the finite element model of existing coupled model of the machine tool-spindle system. The characteristics of joints are investigated with the help of iteration process and finite element model is updated at the same time. Experiments prove that, without knowing dynamics of joints between spindle and machine tool, response of the spindle attached to the machine tool can be predicted.

Hongrui Cao et al. [26] put forward a finite element model to predict the response of a spindle system with localized bearing defect. Localized defects at outer ring of the bearings are modeled and response of the spindle system is simulated. Sensor placement for localized defects at bearings is optimized. It is shown that perfect place for sensor depends on the vibration modes effected by boundary conditions and path between the input and sensor.

Mathieu Ritou et al. [33] introduced an experimental and original approach for revealing effect of spindle condition (repaired or damaged) on the dynamics of the spindle. Failure modes of a high-speed machining spindle are identified and their effects on FRF are observed on simulation environment. It is concluded that the main effect is because of preload changes rather than bearing defects. It is shown that bearing faults mainly effects the amplitudes of modes. The effect of spindle condition on cutting performance is also studied.

Songtao Xi et al. [27] introduced a model for spindle systems that include angular contact ball bearing and floating displacement bearing considering defects at the bearings. The dynamic model of floating displacement bearing, and angular contact ball bearing is developed using geometrical relations and Hertz theory. The shaft of the spindle is modeled using finite element method. Using the introduced method, response of spindle system with defected and good conditioned bearings can be simulated. The model can be seen from Figure 1.15. The model is compared with a machine tool spindle unit that has a defect at the inner ring of the bearing because of a collision occurred during operation. Results of the study shows that model can simulate response of the system and forces between defected bearings accurately.

The proposed can be used as a useful tool for condition monitoring of the spindle system.

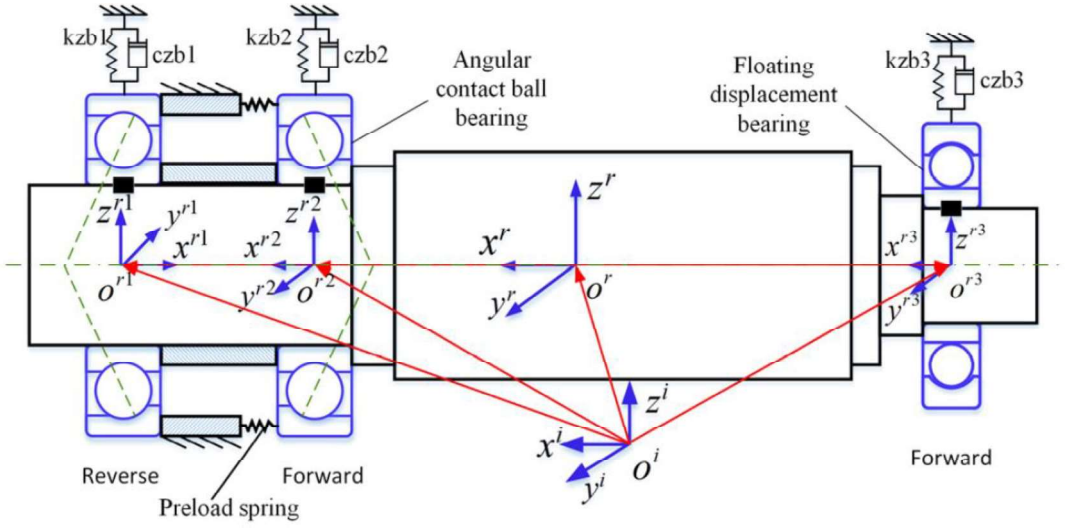

Figure 1.15 The Model of Spindle System Supported by Angular Contact Ball Bearings and Floating Displacement Bearing [27]

Fawzi et al. [37] presented formulation for the total stiffness and damping matrices of a shaft carried by angular contact ball bearings, carrying a disk which has a center of mass is not at the center. The analysis considered bearing non-linearities, cage movement and preload of bearings. The results are applied to a spindle that has already been studied by other researchers and perfect agreements between results are obtained. Effect of using full stiffness matrix and diagonal stiffness matrix is compared and full matrix is recommended. At appendix A and B, every element of stiffness and damping matrixes are given on by one.

Xuening Zhang et al. [30] showed that unbalance at rotor of a rotor-bearing system changes stiffness of the bearings periodically. Finite number of balls at a bearing also changes stiffness of a bearing periodically. When these two effects are added up, the excitations coming from chancing stiffness of the bearing can result severe vibrations under operating conditions. The paper extended 5 degree of freedom angular contact ball bearing model and added forces related to unbalance at shaft. Schematic diagram can be seen from Figure 1.16, torsional stiffness normal to Z direction is not defined.

Stability analysis is done, and effect of forces result of unbalance, damping and bearing loads are discussed.

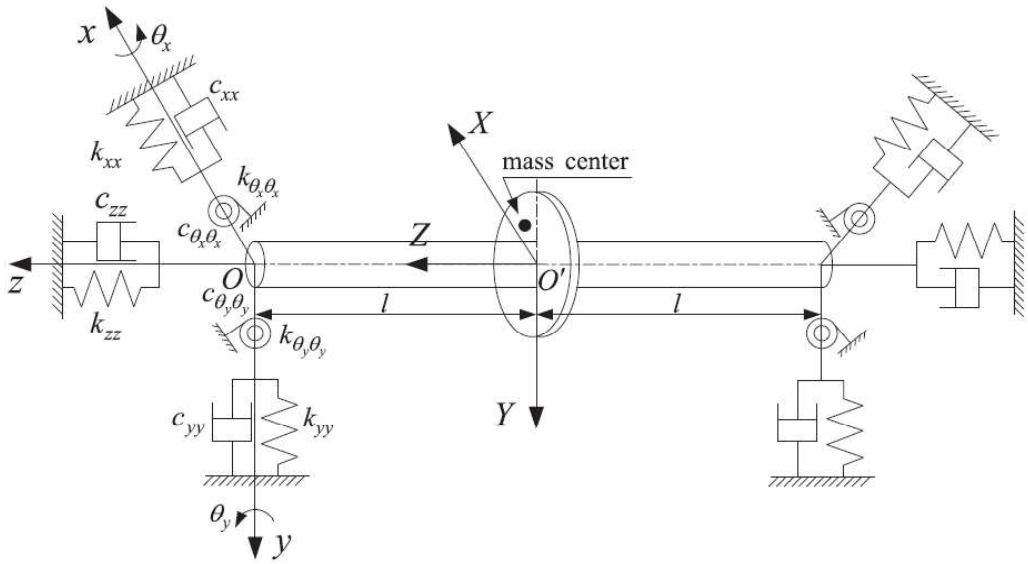

Figure 1.16 Diagram of Rotating Rotor-Bearing System Showing Degree of Freedoms [30]

Rahman et al. [31] proposes a system of differential equations for analyzing shaft-bearing assemblies. The contact between balls and inner-outer races are described using Hertz theory. Response of the multi-support spindle system have obtained. Design parameters are bearing specifications, magnitude of preload and number of bearings supporting the shaft. As a result of study, significance of these parameters to frequencies and amplitudes are shown.

Lynagh et al. [32] presents a model of bearing vibration including waviness of races and off-sized rolling elements. The vibrations moments and forces are formulated, and principal and side-band contributions are displayed. The proposed model predicted vibration related to manufacturing faults with satisfying success. Vibration measurements are done with high-precision non-contact eddy current probes.

1.1.3 Bearing Fault Detection

Bearings are one of the most important parts of rotary machines, their failure is often and most of the time results with downtime, so condition monitoring of bearings is critical [38][39]. Some of condition monitoring techniques used for bearings are acoustic measurement, temperature monitoring, vibration analysis, oil debris monitoring. Among these vibration monitoring is most frequently used.

The vibration coming from a defected bearing can be analyzed in frequency or time domain. Time domain analysis are generally dependent to prediction of statistical criteria like kurtosis, crest factor, skewness, RMS etc. Frequency domain analysis detects faults at the bearings using fundamental bearing frequencies which are calculated using geometry of the bearing and the rotational speed difference between outer and inner rings [40].

1.1.3.1 Time Domain Approaches

The vibration signal in time domain (acceleration, velocity or displacement) of defected and good bearing contains different vibration signatures. These signatures can be used to distinguish good and faulty bearings.

Root mean square (RMS) is a measure of overall level of a signal. It is an indicator of amount of power in the signal. Besides bearings, RMS is also used to detect defected rotary machines. ISO 10816 is a standard for vibratory machines which vibration is measured from non-rotating parts. There are also more specified standards, for instance, ISO 17243 is a standard for spindles. Both standards classify RMS values and helps evaluating condition of a machine. RMS is calculated as follows,

$$RMS = \sqrt{\frac{1}{n}\sum_{i=1}^{n} x_i^2} \tag{1.1}$$

where n is number of samples, x_i is the amplitude at the n'th sample [41].

Crest factor is the ratio between peak value and RMS. It is a measure of spikiness or impulsive nature of a signal. It indicates sharp peaks. Crest factor can detect acceleration jumps even if RMS stay constant [41].

Skewness measures absence of symmetry about mean of a signal [42][43]. Skewness is calculated as follows,

$$Skewness = \frac{\frac{1}{n}\sum_{i=1}^{n}(x_i-\bar{x})^3}{\left(\sqrt{\frac{1}{n}\sum_{i=1}^{n}(x_i-\bar{x})^2}\right)^3} \quad (1.2)$$

where $\bar{x}$ is the mean value. $\bar{x}$ can be calculated as follows,

$$\bar{x} = \frac{1}{n}\sum_{i=1}^{n} x_i \quad (1.3)$$

Kurtosis is a metric showing flatness or spikiness of a signal. It shows if a signal is flat or peaked with respect to signals normal distribution [44]. In other words, spiky distributed signals have higher kurtosis whereas flat distributed signals have lower kurtosis. A heathy bearing's kurtosis is three. Kurtosis value greater than three is an indicator of bearing fault. The value three means a waveform of acceleration with a Gaussian amplitude distribution [45]. There is a major drawback of kurtosis. When there is a well-advanced damage at the bearing, kurtosis value starts to decrease. This drop at the kurtosis can come down to the level of an undamaged bearing [11]. Kurtosis can be calculated as follows,

$$Kurtosis = \frac{\frac{1}{n}\sum_{i=1}^{n}(x_i-\bar{x})^4}{\left(\frac{1}{n}\sum_{i=1}^{n}(x_i-\bar{x})^2\right)^2} \quad (1.4)$$

Shao et al. [46] used laser displacement sensor for rolling bearing fault detection. The paper shows that statistical tools combined with power spectrum is an effective way of determining faults. Advantages of using laser displacement sensor instead of a classical accelerometer is emphasized.

Sreejith et al. [47] proposed a neural network method for recognizing localized bearing faults for rolling element bearings. Time domain parameters are used as

input to neural network. Effectiveness of the method is shown using bearing vibration data which is obtained experimentally.

Besides interpretation of statistical parameters, there are different time domain approaches. Gustafsson et al. [48] presented a novel method to detect defects on the surface of balls and raceways. Their method basically searched for number of peaks passing a voltage level.

1.1.3.2 Frequency Domain Approaches

Frequency domain (spectral) analysis are the most popular and widely used approach for bearing fault detection. In frequency domain approach, using famous Fast Fourier Transform (FFT), time data is converted to discrete frequency components. Spectral analysis is good at detecting frequency components in the signal compared to time domain analysis.

When a bearing rotates at constant rotational speed, components of the bearing which are balls, cage, and inner and outer races, moves with respect to each other. This motion creates specific vibration frequencies per the rotational speed of the bearing. Generally outer race of bearing stays still and inner race rotates. If this is not the case, vibration frequencies are generated per difference between rotational speeds of inner and outer races. So, faults at the bearing can be found by searching for these fundamental frequencies and their harmonics at the FFT of the signal [11].

Taylor et al. [49] used frequency domain methods to investigate defects at the outer and inner raceway of a bearing. Defects on the balls and the cage are detected and length of defects at the inner and outer race is predicted within limits. In addition, dry of lubrication bearings are distinguished among others.

Osuagwu et al. [50] demonstrated an example for absence of bearing fundamental frequencies in the spectrum and they showed that absence of bearing fundamental frequencies can occur because of the different effects. One of them is an average and shift effect that results of relocation of fundamental frequencies from the calculated

values. The other one is an inter-modulation effect that translates the defect frequencies to irrelevant locations. Then they proposed a method to detect faults if absence of fundamental frequencies at the spectrum occurs. The proposed method is called power cepstrum.

Linkai Niu et al. [51] proposed a novel method to calculate bearing passing frequencies based on a dynamic model of ball bearings. Unlikely the classic model, the proposed model includes 3D motions, relative slippage of elements, cage effects and localized surface defects. In addition, the proposed model approaches localized defects more accurately considering finite size of the rolling element, the clearance due to material removal at the defected region, and changes of directions of the contact forces. The study shows that shaft speed, friction coefficient, external loads, raceway groove curvatures, defect size and contact angle has effect on the bearing defect frequencies. For a ball bearing under load, the resultant of sliding and rolling motion takes place in the contact region and bearing defect frequencies calculated by kinematic relations are inaccurate, specifically for high rotational speeds, large contact angle conditions occur. The proposed method is validated with two experiments.

Signal processing methods are used to make frequency domain analysis more efficient. Braun et al. [52] introduced a signal decomposition method. Major advantage of the method is its lack of deep information to structural parameters of rotating machinery. Applicability of the method is tested with a roller bearing which has artificially generated fault. McFadden et al. [53] reviewed high frequency resonance technique combined with envelope analysis. The technique helps identifying fundamental bearing frequencies even when they are not noticeable in the spectrum.

Martin et al. [54] introduced a normalizing method which is an extension of an envelope technique, with respect to healthy bearing data. The results shown confirms the effectiveness of envelope technique and normalization gives a sensitive measure of the fault frequency.

Wavelet analysis is one of these signal processing methods. Wavelet Transform is useful for analysis of non-stationary signals since it is an alternative to the classical short time Fourier transform. The biggest difference is STFT uses a single analysis window whereas WT uses long windows at low frequencies and shorth windows at high frequencies[55].

Over the past years, wavelet theory has become one of fast-growing and spreading signal processing and mathematical tool. Morlet was put forward the novel concept of wavelet in 1984 for the first time [56].

In 1996 Mori, Kasashima, Yoshioka and Uneo [57] did one of the first wavelet transform based work for detecting bearing faults via vibration measurement. They presented a method for the prediction of spalling on bearings with discrete wavelet transform. Mori and the others showed that when a ball rolls over pre-spalling region of the raceway at the outer cage, impulsive outputs can be seen at the vibration signal.

Liu et al. [58] proposed a machinery diagnosis method using wavelet packet transform. Studies are done on ball bearings and seen that method is sensitive to faults. They showed that proposed method is useful for the detection of non-stationary faults. This again one of the first studies on bearings using wavelet transform.

Paya and Esat [59] used continuous wavelet transform for preprocess of vibration data. They used the processed data to feed the artificial neural network and managed to automatically detect inner cage faults of a bearing. This work is again one of first ones using wavelet transform to process wavelet data and then use artificial neural network for automatic fault detection.

Nikolaou and Antoniadis [60] showed that nature of faults of rolling element bearing can be identified using wavelet packet transform. Their work stated that, compared to continuous wavelet transform, wavelet packet transform is more efficient when computational time is considered and more flexible.

Li and Ma [61] detected localized bearing defects using wavelet transform. Localized defects are introduced to outer race of a bearing by purpose using electric discharge machine. Using wavelet transform defects at different locations are detected at different working conditions and then compared with theoretical values.

Prabhakar, Mohanty and Sekhar [62] used discrete wavelet transform to detect localized bearing defects at inner and outer cage. Vibration data taken from ball bearings with single and multiple point defects on inner cage, outer cage and combination of defects have been studied at the analysis. Results shows that impulses appear according to associated characteristic defect frequencies.

Shi et al. [63] combined wavelet transform and envelope spectrum and come up with a new method to detecting defects in rolling element bearings. The method decomposes the signal into different signals with wavelet transform and then envelope spectrum is used to extract the characteristic frequency of defect at specified scale. The optimal scale is selected based on Shannon entropy. It is shown that the method is reliable and sensitive to detecting defects on dynamic parts of the bearing.

Zhang, Gao and Lee [64] developed a new technique in order to determine structural defects occurred on spindles using wavelet transform. Vibrations taken from a bearing test system is subjected to the technique. A defect has introduced to the outer cage of a bearing. The defect characteristic frequency is estimated based on geometry of the bearing. The frequency component has seen on the scalogram. In addition, technique is applied to a spindle test bed which impact forces are applied. Frequencies related with the inner cage defect and spindle unbalance caused by impact forces are successfully determined.

Wang et el. [65] presented e new approach to detect faults at incipient stage. Short period and weak amplitude of structural defects at early stages makes it hard to extract features. Wavelet transform is applied to signal to detect fault at incipient stage. And then, Fourier transform is applied in to tell the exact frequency of defect. With combination of wavelet and Fourier transform a localized point defect at a rolling bearing is identified successfully.

Zhu et al. [66] introduce a method that combines continuous wavelet transform and Kolmogorov Smirnov test to detect transients for machine fault detection. Transients are signal components which exists not for a long period of time and span within a broad range of frequency. Transients generally contain information that can used to characterize system dynamics. CWT is used for decomposing time domain signal into time-scale plane. Then, a method based on K-S test is proposed to reveal the transient feature.

Yan and Gao [67] presents a hybrid technique for signal processing to spindle condition monitoring and health diagnosis. The technique includes integration of wavelet packet transforms and principal feature analysis. Different defect conditions are constituted on a spindle test system and vibration signals are measured. The developed technique improves the signal to noise ratio of the data and reduces number of features need to conduct the analysis. This decrease allows for more efficient use for existing sensor data at a lower computing cost.

Nizwan et al. [68] used discrete wavelet transform to detect different types of defects at bearings. They did their work on four bearings which are outer race defected, a point defect at a ball, corroded and a healthy one for comparison. They showed that at high speeds discrete wavelet transform is a good way to detect defects but at low speeds it should be supported by using RMS value. They noted that the suggested technique can be done without shutting down the machine.

Kankar et al. [69] studied on fault detection of bearings having localized defects with wavelet transform. Different methods are examined to distinguish which method better suites to bearing diagnosis. Complex Morlet Wavelet is found to be best suited to the bearing diagnosis among seven different mother wavelets using minimum Shannon Entropy Criterion. Using complex Morlet Wavelet with Support Vector Machine led to 100% success. Related work done so far, starting with Paya et. al. [59], is also covered.

Kumar et al. [70] proposed a technique for measuring outer race defect width of taper rolling bearing. The technique is based on decomposition using Symlet as

mother wavelet. Experimental measurements and analysis afterwards showed that decomposition of signal using Symlet 5th order basic wavelet is proper for measuring width of outer race defect of a taper rolling bearing. The use of Symlet which increases the signal's sharpness, makes it easier to detect the entry point of the defect. Image analysis is used to verify the defect width.

1.2 Scope of Thesis

The aim of the thesis is to investigate effects of bearing faults to spindles and detect them alongside with the shaft faults using vibration data collected at operational conditions. An analytical bearing dynamics model considering faults is constituted. A finite element model of a spindle is created, and outputs of the bearing model are used as inputs to observe effects of bearing defects to spindle point FRF and tool point FRF. In addition, effect of bearing faults to tool point FRF of spindles with different types of tools are explored. After that, results of finite element model are compared with the experiment results. In addition, vibration data collected from different spindles at different operational conditions are analyzed using time-domain and frequency-domain methods. Presence of different faults are discussed.

1.3 Outline of Thesis

Thesis outline is as follows:

In Chapter 2, a bearing model considering a continuous outer race defect is introduced. Then, the model is validated by comparing results with a well-accepted paper from the literature. Case studies are conducted to investigate behavior of stiffness of bearing with changing defect size, preload, and direction of radial force.

In Chapter 3, a finite element model of a spindle is constructed. Bearings are modeled as springs and by equating spring constants to calculated defected bearing stiffness values, effects of defect at bearings to spindle FRF is investigated. A holder and two

different tools are added to the finite element model and tool point FRF for two different tools for different bearing conditions are studied.

In Chapter 4, the experimental setup and measurement procedures are presented. Then, results of performed modal tests to the machine tool spindles before and after maintenance, are presented.

In Chapter 5, frequently used time-domain methods are presented. Vibration data acquisition system is explained and standards that are used in the industry are introduced. In addition, bearing defect frequencies are introduced and formulation to calculate them is given. Common faults for bearing shafts are represented. Five different spindles are analyzed using presented methods.

In Chapter 6, conclusion of the thesis is given and ways to improve the thesis is mentioned.

CHAPTER 2

MODELING OF BEARING DYNAMICS INCLUDING DEFECTS

2.1 Formulation

Hertz asserted that the contact of two bodies, rather than a point or line contact, a contact area must form causing the load at contact to disperse over a surface. At the point contact the formed stress distribution can be seen from Figure 2.1. This distribution creates an ellipsoid at the contact surface [9].

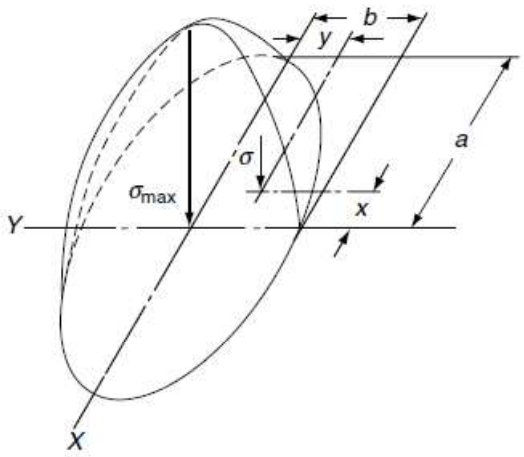

Figure 2.1 Stress Distribution of a Point Contact [9]

Hertz made following assumptions while performing the analysis,

- All the deformations are in the elastic range, the proportional limit of contacting bodies do not exceed.
- Load is perpendicular to the contact surface so shear stress is neglected.
- Dimensions of the contact are smaller than the radius of curvature.
- The radius of curvature of the contact areas at both bodies are very large when comparing with the dimensions of same areas.

The relationship between deformation δ and normal load Q at each rolling element can be defined with the expression,

$$Q = K\delta^n \tag{2.1}$$

where K is the equivalent contact stiffness and n is equal to 1.5 for ball bearings. Total deformation at the bearing can be expressed as follows:

$$\delta_n = \delta_i + \delta_o \tag{2.2}$$

where δ_i and δ_o represents the deformations at the ball-inner race and ball-outer race contacts respectively.

In addition, equivalent contact stiffness can be expressed as follows:

$$K = \left[\frac{1}{\left(\frac{1}{K_i}\right)^{\frac{1}{n}} + \left(\frac{1}{K_o}\right)^{\frac{1}{n}}}\right]^n \tag{2.3}$$

where K_i and K_o represens contact stiffness at the ball-inner race and ball-outer race intersection, respectively.

Section view of a bearing can be seen from Figure 2.2. Some definitions must be made in order to formulate inner and outer ring deflection constants, K_i and K_o.

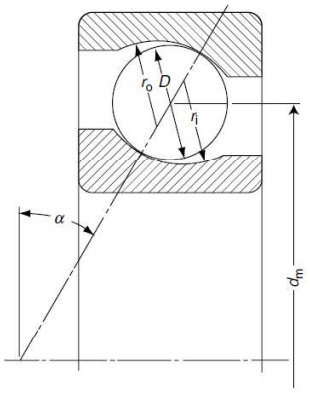

Figure 2.2 Section View of a Bearing [9]

$$f_i = \frac{r_i}{D},\ f_o = \frac{r_o}{D},\ \gamma = \frac{Dcos\alpha}{d_m} \tag{2.4}$$

where D is diameter of the rolling element, r_i and r_o are radii of raceway groove curvature, $d_m$is pitch diameter and α is the contact angle.

According to Hertzian theory, curvature sum of inner and outer races can be expressed with

$$\sum\rho_i = \frac{1}{D}\left(4 - \frac{1}{f_i} + \frac{2\gamma}{1-\gamma}\right) \tag{2.5}$$

$$\sum\rho_o = \frac{1}{D}\left(4 - \frac{1}{f_o} - \frac{2\gamma}{1+\gamma}\right) \tag{2.6}$$

And curvature difference is

$$F(\rho)_i = \frac{\frac{1}{f_i} + \frac{2\gamma}{1-\gamma}}{4 - \frac{1}{f_o} - \frac{2\gamma}{1+\gamma}} \tag{2.7}$$

$$F(\rho)_o = \frac{\frac{1}{f_o} - \frac{2\gamma}{1+\gamma}}{4 - \frac{1}{f_o} - \frac{2\gamma}{1+\gamma}} \tag{2.8}$$

Using above equations K_i and K_o can be expresed as [2]

$$K_i = \frac{2^5}{3\left(\delta_i^*\right)^{3/2}(\sum\rho_i)^{1/2}}\left(\frac{1-\xi_1^2}{E_1} + \frac{1-\xi_2^2}{E_2}\right)^{-1} \tag{2.9}$$

$$K_o = \frac{2^5}{3(\delta_o^*)^{3/2}(\sum\rho_o)^{1/2}}\left(\frac{1-\xi_1^2}{E_1} + \frac{1-\xi_2^2}{E_2}\right)^{-1} \tag{2.10}$$

where ξ_1 and ξ_2 are Poisson's ratio and $E_1$and E_2 are Young's Modulus of the materials of balls and races. δ^* is the dimensionless contact deformation and is a function of curvature difference. Value of δ^* can be determined using Table 1.

Table 1 Dimensionless Contact Parameters [9]

$F(\rho)$	a^*	b^*	δ^*
0	1	1	1
0.1075	1.0760	0.9318	0.9974
0.3204	1.2623	0.8114	0.9761
0.4795	1.4556	0.7278	0.9429
0.5916	1.6440	0.6687	0.9077
0.6716	1.8258	0.6245	0.8733
0.7332	2.011	0.5881	0.8394
0.7948	2.265	0.5480	0.7961
0.83495	2.494	0.5186	0.7602
0.87366	2.800	0.4863	0.7169
0.90999	3.233	0.4499	0.6636
0.93657	3.738	0.4166	0.6112
0.95738	4.395	0.3830	0.5551
0.97290	5.267	0.3490	0.4960
0.983797	6.448	0.3150	0.4352
0.990902	8.062	0.2814	0.3745
0.995112	10.222	0.2497	0.3176
0.997300	12.789	0.2232	0.2705
0.9981847	14.839	0.2072	0.2427
0.9989156	17.974	0.18822	0.2106
0.9994785	23.55	0.16442	0.17167
0.9998527	37.38	0.13050	0.11995
1	∞	0	0

Note that, bearing stiffness expression given by Equations 2.1 to 2.10 are applicable for healthy bearings and do not consider the defects. To include the effect of defects in bearing model, first an outer defect can be included as shown in Figure 2.3. Figure 2.3Figure 2.3 also shows the coordinate system that is used in the analytical formulation [18].

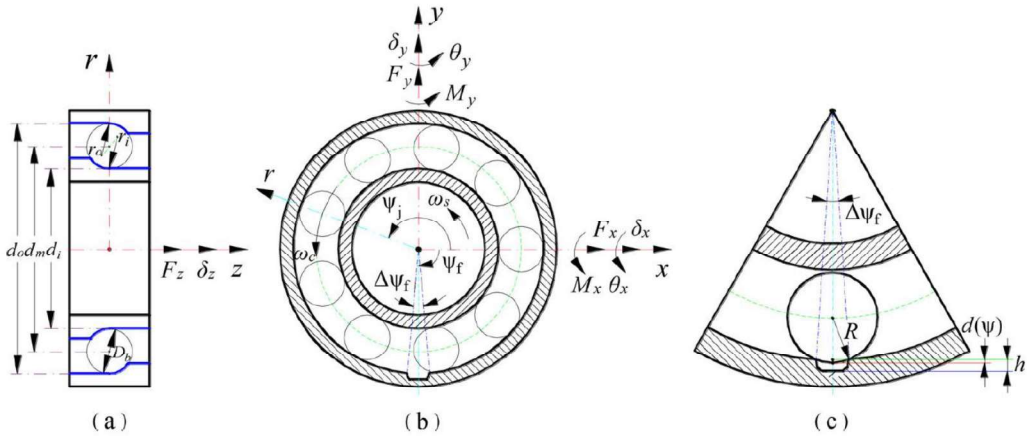

Figure 2.3 Coordinate System of The Bearing to Define Relative Rotations and Displacements; (a) Radial Section View, (b) Axial Section View And (c) Enlarged View of Defect [71]

Relative displacements and rotations between the outer and inner races are defined as;

$$q = [\delta_x \ \delta_y \ \delta_z \ \theta_x \ \theta_y \ ]^T \tag{2.11}$$

Loads and moments applied to the bearing are defined as;

$$F = [F_x \ F_y \ F_z \ M_x \ M_y]^T \tag{2.12}$$

From Figure 2.3 it can be seen that position of the center of the defect is at defined with ϕ_f and extends along $\Delta\phi_f$, depth of the defect is h. Assuming a square shaped defect, for the j'th ball, depth profile can be defined as follows:

$$d(\phi_j) = \begin{cases} h & if\ \phi_f - 0.5\Delta\phi_f < \phi_j \le \phi_f \\ h & if\ \phi_f < \phi_j < 0.5\Delta\phi_f + \phi_f \\ 0 & if\ 0.5\Delta\phi_f + \phi_f \le \phi_j \le \phi_f - 0.5\Delta\phi_f \end{cases} \tag{2.13}$$

where R_o is the outer race radius, r_b is the radius or the ball.

The contact deformation δ_j for j'th ball is

$$\delta_j = \begin{cases} A - A_0, & \delta_j > 0 \\ 0, & \delta_j \le 0 \end{cases} \tag{2.14}$$

where A_0 and A are relative distances between groove curvature centers at inner and outer races at the unloaded and loaded conditions. A_0 can be seen from Figure 2.4.

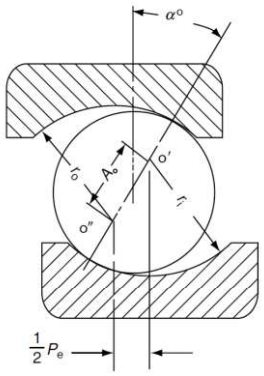

Figure 2.4 Section View of a Ball Bearing Showing Ball-Race Contact [9]

In addition, A and A_0 can be calculated as follows,

$$A_0 = r_i + r_o - D = (f_i + f_0 - 1)D \tag{2.15}$$

$$A = \sqrt{{\delta_{rj}^*}^2 + {\delta_{zj}^*}^2} \tag{2.16}$$

and

$$\delta_{rj}^* = A_0 cos\alpha_0 + \delta_{rj} \tag{2.17}$$

$$\delta_{zj}^* = A_0 sin\alpha_0 + \delta_{zj} \tag{2.18}$$

Displacements of j'th ball at the axial and radial directions are calculated using relative displacements and rotation between the outer and inner races as follows

$$\delta_{rj} = \delta_x \cos\phi_j + \delta_y \sin\phi_j - r_L - d(\phi_j)\, cos\alpha_0 \tag{2.19}$$

$$\delta_{zj} = \delta_z + r_d(\theta_x sin\phi_j - \theta_y cos\phi_j) - d(\phi_j)\, sin\alpha_0 \tag{2.20}$$

r_L is radial clearance and r_d is the distance of inner race groove curvature center in radial direction and can be calculated as follows

$$r_d = \frac{1}{2} d_m + \left(r_i - \frac{1}{2} D_b\right) \cos\alpha^0 \tag{2.21}$$

The relation between the Hertzian normal force for j'th rolling element Q_j and contact deformation δ_j for j'th rolling element is defined as

$$Q_j = K\delta_j^{1.5} \tag{2.22}$$

Q_j is acting on the ball at the direction of loaded contact angle α_j, α_j can be calculated as follows

$$tan\ \alpha_j = \frac{\delta_{zj}^*}{\delta_{rj}^*} \tag{2.23}$$

For static equilibrium sum of all loads and moments acting on every rolling element, resulting Q_j,must be equal to loads and moment acting on the bearing. So, following nonlinear equation can be written

$$\begin{bmatrix} F_x \\ F_y \\ F_z \\ M_x \\ M_y \end{bmatrix} = \sum_{j=1}^{N_b} \begin{bmatrix} F_{xj} \\ F_{yj} \\ F_{zj} \\ M_{xj} \\ M_{yj} \end{bmatrix} = \sum_{j=1}^{N_b} Q_j \begin{bmatrix} cos\alpha_j cos\phi_j \\ cos\alpha_j sin\phi_j \\ sin\alpha_j \\ r_d sin\alpha_j sin\phi_j \\ -r_d sin\alpha_j cos\phi_j \end{bmatrix} \tag{2.24}$$

Putting defined expressions into Q_j and rewriting the equation, forces and moments applied to the bearing can be found as follows

$$F_x = K\sum_{j=1}^{N_b} \left\{ \sqrt{\begin{matrix} \left(A_0 cos\alpha_0 + \delta_x \cos\phi_j + \delta_y \sin\phi_j - r_L - d(\phi_j)\, cos\alpha_0\right)^2 \\ +\left(A_0 sin\alpha_0 + \delta_z + r_d(\theta_x sin\phi_j - \theta_y cos\phi_j) - d(\phi_j)\, sin\alpha_0\right)^2 \end{matrix}} - A_0 \right\}^{1.5} cos\alpha_j cos\phi_j \tag{2.25}$$

$$F_y = K\sum_{j=1}^{N_b} \left\{ \sqrt{\begin{matrix} \left(A_0 cos\alpha_0 + \delta_x \cos\phi_j + \delta_y \sin\phi_j - r_L - d(\phi_j)\, cos\alpha_0\right)^2 \\ +\left(A_0 sin\alpha_0 + \delta_z + r_d(\theta_x sin\phi_j - \theta_y cos\phi_j) - d(\phi_j)\, sin\alpha_0\right)^2 \end{matrix}} - A_0 \right\}^{1.5} cos\alpha_j sin\phi_j \tag{2.26}$$

$$F_z = K\sum_{j=1}^{N_b} \left\{ \sqrt{\begin{matrix} \left(A_0 cos\alpha_0 + \delta_x \cos\phi_j + \delta_y \sin\phi_j - r_L - d(\phi_j)\, cos\alpha_0\right)^2 \\ +\left(A_0 sin\alpha_0 + \delta_z + r_d(\theta_x sin\phi_j - \theta_y cos\phi_j) - d(\phi_j)\, sin\alpha_0\right)^2 \end{matrix}} - A_0 \right\}^{1.5} sin\alpha_j \tag{2.27}$$

$$M_x = Kr_d \sum_{j=1}^{N_b} \left\{ \sqrt{\begin{matrix} \left(A_0 cos\alpha_0 + \delta_x \cos\phi_j + \delta_y \sin\phi_j - r_L - d(\phi_j)\, cos\alpha_0\right)^2 \\ +\left(A_0 sin\alpha_0 + \delta_z + r_d(\theta_x sin\phi_j - \theta_y cos\phi_j) - d(\phi_j)\, sin\alpha_0\right)^2 \end{matrix}} - A_0 \right\}^{1.5} sin\alpha_j sin\phi_j \tag{2.28}$$

$$M_y = -Kr_d \sum_{j=1}^{N_b} \left\{ \sqrt{\begin{matrix} \left(A_0 cos\alpha_0 + \delta_x \cos\phi_j + \delta_y \sin\phi_j - r_L - d(\phi_j)\, cos\alpha_0\right)^2 \\ +\left(A_0 sin\alpha_0 + \delta_z + r_d(\theta_x sin\phi_j - \theta_y cos\phi_j) - d(\phi_j)\, sin\alpha_0\right)^2 \end{matrix}} - A_0 \right\}^{1.5} sin\alpha_j cos\phi_j \tag{2.29}$$

The condition of δ_j being larger than zero must not missed. If inside of the curly braces term in the formulation is less than zero, it must be treated as zero. The stiffness matrix is calculated by linearizing the force and displacement relation. It is defined as K=∂F/∂q (instead of K=F/q) and calculated for given loads and moments. Resulting symmetric stiffness matrix is as follows

$$K_b = \begin{bmatrix} k_{xx} & k_{xy} & k_{xz} & k_{x\theta_x} & k_{x\theta_y} \\ . & k_{yy} & k_{yz} & k_{y\theta_x} & k_{y\theta_y} \\ . & . & k_{zz} & k_{z\theta_x} & k_{z\theta_y} \\ . & . & . & k_{\theta_x\theta_x} & k_{\theta_x\theta_y} \\ . & . & . & . & k_{\theta_y\theta_y} \end{bmatrix} = \begin{bmatrix} \frac{\partial F_x}{\partial \delta_x} & \frac{\partial F_x}{\partial \delta_y} & \frac{\partial F_x}{\partial \delta_z} & \frac{\partial F_x}{\partial \theta_x} & \frac{\partial F_x}{\partial \theta_y} \\ . & \frac{\partial F_y}{\partial \delta_y} & \frac{\partial F_y}{\partial \delta_z} & \frac{\partial F_y}{\partial \theta_x} & \frac{\partial F_y}{\partial \theta_y} \\ . & . & \frac{\partial F_z}{\partial \delta_z} & \frac{\partial F_z}{\partial \theta_x} & \frac{\partial F_z}{\partial \theta_y} \\ . & . & . & \frac{\partial M_x}{\partial \theta_x} & \frac{\partial M_x}{\partial \theta_y} \\ . & . & . & . & \frac{\partial M_y}{\partial \theta_y} \end{bmatrix} \tag{2.30}$$

Expressions for elements of stiffness matrix are as follows:

$$k_{xx} = K \sum_{j=1}^{N_b} \frac{(A-A_0)^{1.5} \cos^2\phi_j \left(\frac{1.5A{\delta_{rj}^*}^2}{A-A_0} + A^2 - {\delta_{rj}^*}^2 \right)}{A^3} \tag{2.31}$$

$$k_{xy} = K \sum_{j=1}^{N_b} \frac{(A-A_0)^{1.5} sin\phi_j \cos\phi_j \left(\frac{1.5A{\delta_{rj}^*}^2}{A-A_0} + A^2 - {\delta_{rj}^*}^2 \right)}{A^3} \tag{2.32}$$

$$k_{xz} = K \sum_{j=1}^{N_b} \frac{(A-A_0)^{1.5} \delta_{rj}^* \delta_{zj}^* \cos\phi_j \left(\frac{1.5A}{A-A_0} - 1 \right)}{A^3} \tag{2.33}$$

$$k_{x\theta_x} = r_d K \sum_{j=1}^{N_b} \frac{(A-A_0)^{1.5} \delta_{rj}^* \delta_{zj}^* sin\phi_j cos\phi_j \left(\frac{1.5A}{A-A_0} - 1 \right)}{A^3} \tag{2.34}$$

$$k_{x\theta_y} = r_d K \sum_{j=1}^{N_b} \frac{(A-A_0)^{1.5}\delta_{rj}^*\delta_{zj}^* cos^2\,\phi_j\left(1-\frac{1.5A}{A-A_0}\right)}{A^3} \tag{2.35}$$

$$k_{yy} = K \sum_{j=1}^{N_b} \frac{(A-A_0)^{1.5}\sin^2\phi_j\left(\frac{1.5A{\delta_{rj}^*}^2}{A-A_0}+A^2-{\delta_{rj}^*}^2\right)}{A^3} \tag{2.36}$$

$$k_{yz} = K \sum_{j=1}^{N_b} \frac{(A-A_0)^{1.5}\delta_{rj}^*\delta_{zj}^* sin\phi_j\left(\frac{1.5A}{A-A_0}-1\right)}{A^3} \tag{2.37}$$

$$k_{y\theta_x} = r_d K \sum_{j=1}^{N_b} \frac{(A-A_0)^{1.5}\delta_{rj}^*\delta_{zj}^* sin^2\phi_j\left(\frac{1.5A}{A-A_0}-1\right)}{A^3} \tag{2.38}$$

$$k_{y\theta_y} = r_d K \sum_{j=1}^{N_b} \frac{(A-A_0)^{1.5}\delta_{rj}^*\delta_{zj}^* sin\phi_j cos\phi_j\left(1-\frac{1.5A}{A-A_0}\right)}{A^3} \tag{2.39}$$

$$k_{zz} = K \sum_{j=1}^{N_b} \frac{(A-A_0)^{1.5}\left(\frac{1.5A{\delta_{zj}^*}^2}{A-A_0}+A^2-{\delta_{zj}^*}^2\right)}{A^3} \tag{2.40}$$

$$k_{z\theta_x} = r_d K \sum_{j=1}^{N_b} \frac{(A-A_0)^{1.5} sin\phi_j\left(\frac{1.5A{\delta_{zj}^*}^2}{A-A_0}+A^2-{\delta_{zj}^*}^2\right)}{A^3} \tag{2.41}$$

$$k_{z\theta_y} = r_d K \sum_{j=1}^{N_b} \frac{(A-A_0)^{1.5} cos\phi_j\left(\frac{{\delta_{zj}^*}^2-1.5A{\delta_{zj}^*}^2}{A-A_0}+A^2\right)}{A^3} \tag{2.42}$$

$$k_{\theta_x\theta_x} = r_d^2 K \sum_{j=1}^{N_b} \frac{(A-A_0)^{1.5}\sin^2\phi_j\left(\frac{1.5A{\delta_{zj}^*}^2}{A-A_0}+A^2-{\delta_{zj}^*}^2\right)}{A^3} \tag{2.43}$$

$$k_{\theta_x\theta_y} = r_d^2 K \sum_{j=1}^{N_b} \frac{(A-A_0)^{1.5} sin\phi_j cos\phi_j\left(\frac{{\delta_{zj}^*}^2-1.5A{\delta_{zj}^*}^2}{A-A_0}+A^2\right)}{A^3} \tag{2.44}$$

$$k_{\theta_y\theta_y} = r_d^2 K \sum_{j=1}^{N_b} \frac{(A-A_0)^{1.5}\cos^2\phi_j\left(\frac{1.5A{\delta_{zj}^*}^2}{A-A_0}+A^2-{\delta_{zj}^*}^2\right)}{A^3} \tag{2.45}$$

2.2 Validation of Bearing Stiffness Model

Length of the defect is defined with an angle along the outer race. Depth and length of the defect are inputs to the model. The position of the defect is defined with the angle between x axis and center point of the defect. For instance, if a defect is defined with an angle 270^0 and with a length of 20^0, it starts at 260^0 and finishes at 280^0 from the x axis.

Balls are positioned starting from x axis and spread along the bearing in counterclockwise with equal angles.

To validate the varying stiffness model, results of Petersen et al. [18] is used. This paper uses the same ball bearing used by Lim et al. [72]. Lim et al. study varying stiffness of a non-defected angular contact ball bearing and a non-defected roller bearing.

The bearing has 12 rolling balls with 6 mm diameter. The radius of groove curvature at the inner raceway is 19.65 mm. The distance between inner and outer raceway groove curvature centers at unloaded condition is 50 μm. The contact angle is 30^0 at unloaded condition and the radial clearance is 0.05 μm. The load-deflection constant, K_n, is 1.45 x 10^{10} $N/m^{1.5}$.

The bearing is only loaded in y axis with -2000 N and at axial direction (z axis) with 500 N, forces at other direction and moments are zero. The defect is located at 270^0. Cage angle vs stiffness graphs are plotted for four different cases ($5^0, 40^0, 70^0$ defects and defect-free cases) and compared with the outputs of Petersen. Graphs of K_{xx}, K_{yy}, K_{zz}, $K_{\theta x\theta x}$, and $K_{\theta y\theta y}$ generated with the model and taken from the article can be seen from Figure 2.5, Figure 2.6, Figure 2.7,Figure 2.8 and Figure 2.9 respectively.

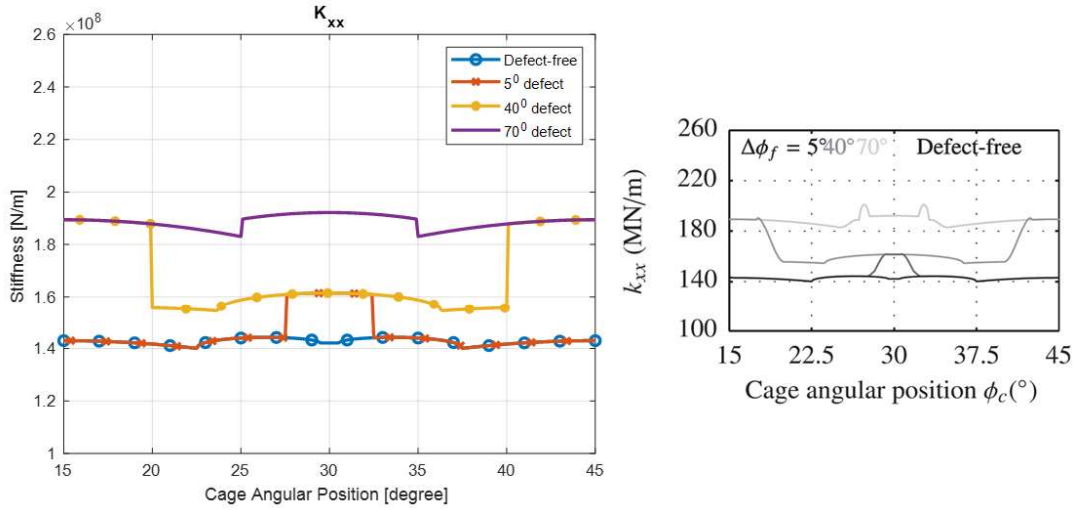

Figure 2.5 K_{xx} Stiffness vs Cage Angle Graph of the Varying Stiffness Model and Output of Petersen [18]

Stiffness value of the bearing at the x direction is given in Figure 2.5. As angle of defect changes, number of balls in the defected region changes. When a ball enters or exits the defected region, a sharp change at the graph occurs. Stiffness value of defect free case is affected from cage angular position but compared to other cases it is stable. Most of 5^0 defected case has same stiffness value with defect-free case since a ball stay in the defected zone for a small period of angle. 40^0 and 5^0 defected cases intersect when only one ball is in the defect. Graph of 40^0 defected case differentiates from graph of 5^0 defected case when second ball also gets in the defected zone. Likewise, graph of 70^0 differs when third ball is in the defect. Stiffness value increases as angle of defect increases. Note that, defect at the bearing is not at this direction. As angle of defect increases, some or all the load needed to be carried by the balls in the defected region is redistributed to the other balls. Since the radial load is also not at this direction, as defect increase load carried by balls at this direction increases and as a result stiffness increases.

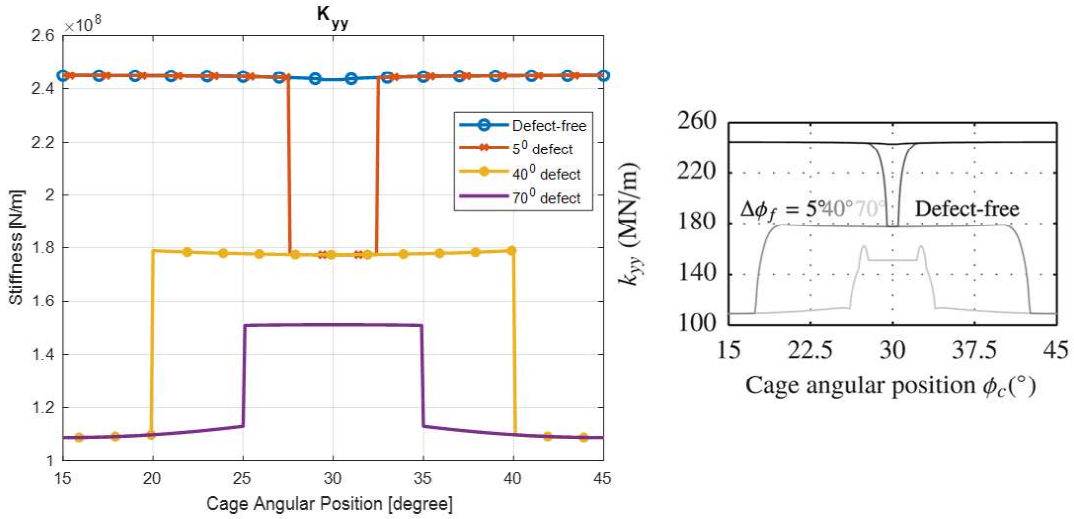

Figure 2.6 K_{yy} Stiffness vs Cage Angle Graph of the Varying Stiffness Model and Output of Petersen [18]

Stiffness at y direction can be seen in Figure 2.6. Defect at the bearing and the radial load is at this direction. Stiffness is decreasing as number of balls in the defected region increases. When a ball enters the defected region, it carries less load and since there is static equilibrium at the system, the load needed to be carried by this ball is carried by other balls. As a result, stiffness at this direction decrease.

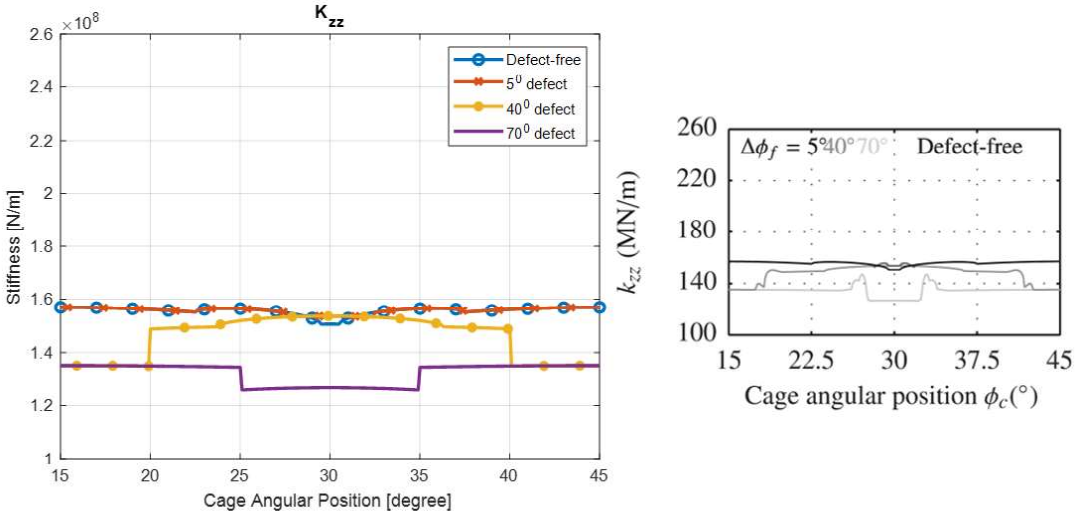

Figure 2.7 Axial Stiffness vs Cage Angle Graph of the Varying Stiffness Model and Output of Petersen [18]

Stiffness at the axial direction is given in the Figure 2.7. Defect at small angles does not affect stiffness value at axial direction as much as radial directions. After a point, when number of balls in the defected region increases, stiffness value decrease. Note that stiffness does not change as much as radial directions.

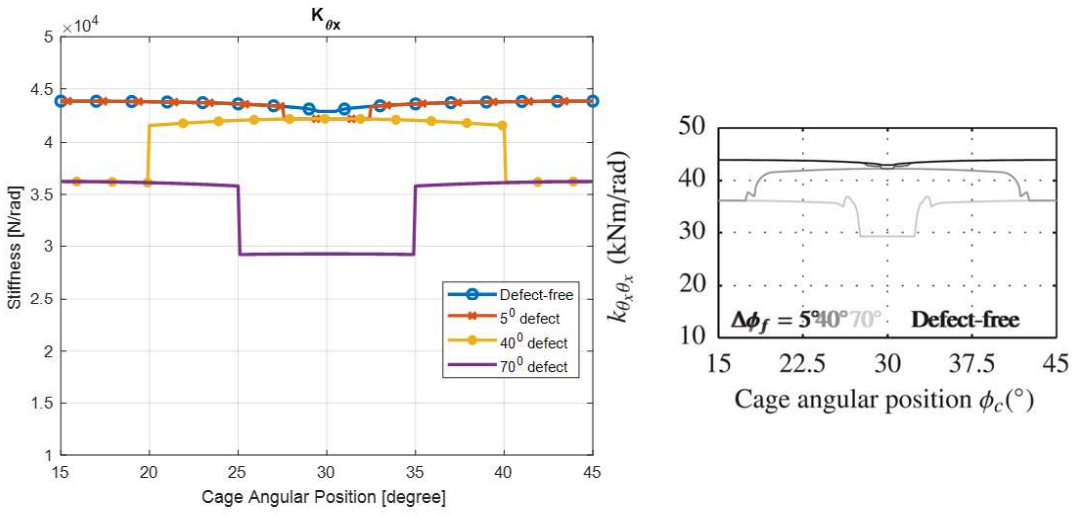

Figure 2.8 Yaw Stiffness vs Cage Angle Graph of the Varying Stiffness Model and Output of Petersen [18]

Stiffness at yaw direction is given in Figure 2.8. As number of balls in the defected region increases stiffness decrease. Defect at the bearing is at this direction so, like y direction, as number of balls in the defected region increase, stiffness decrease. Note that, values are smaller compared to directional stiffnesses.

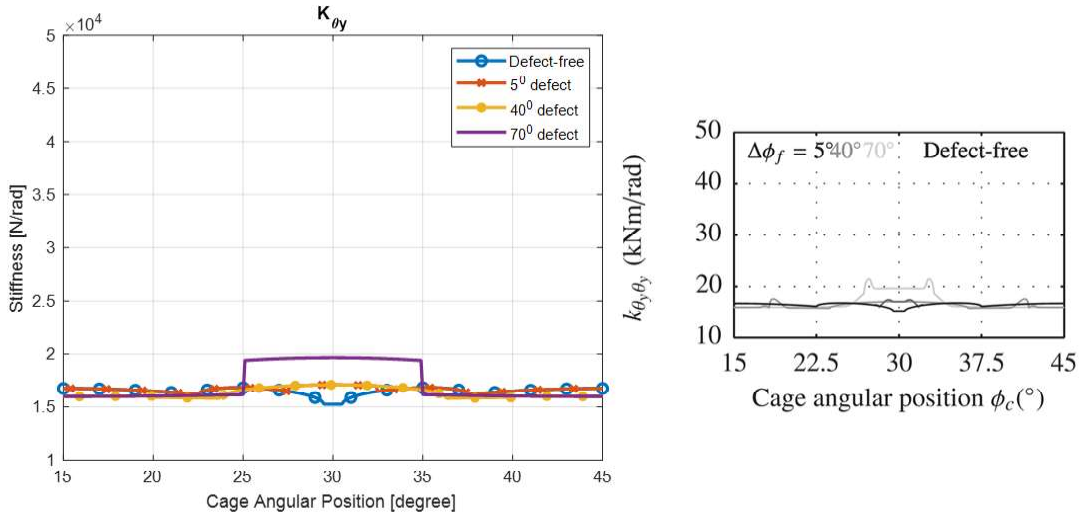

Figure 2.9 Pitch Stiffness vs Cage Angle Graph of the Varying Stiffness Model and Output of Petersen [18]

Stiffness of pitch direction is given in Figure 2.9. Stiffness does not change as much as radial directions with changing defect angle. Since defect at the bearing is not at the pitch direction is not affected as much as yaw direction.

The graphs are plotted only for 30 degrees angle of the cage since there is one ball at every 30 degrees and graphs are symmetrical with 30 degrees period. For instance, graph between 15^0- 45^0 is same with 45^0- 75^0.

Length of defects are selected according to spacing of the balls. At 5^0 defected bearing at some angles there is no ball at the defected region. Because of this, their stiffness values are same at defect-free regions. At 40^0 defected case there is always at least a ball in the defect and sometimes two. At 70^0 defected case there are always at least 2 balls and sometimes 3.

There are pikes at the graphs of Petersen, but graphs of the model has corners instead of spikes. Different than Petersen, at the entrance and exit of the defect, radius of the ball is not considered. At the model, if center of the ball is in the square shaped defect, it is assumed that all of the balls are in the defect zone. This assumption led to sharp corners at the transition parts of the graphs.

2.3 Case Studies

2.3.1 Changing Angle and Depth of Defect vs Stiffness

In addition to presented results in previous section, effect of angle and depth of defect on bearing stiffness is analyzed using the same bearing presented in previous section. The position of the cage is kept constant at zero degree which corresponds to the 30 degrees. Angle of defect is changed from 0 to 70 degrees while depth of the defect is changed from zero to 30μm. Obtained results are shown in Figure 2.10, Figure 2.11, Figure 2.12, Figure 2.13, Figure 2.14. Note that, Figure 2.11 is plotted for opposite direction for better understanding.

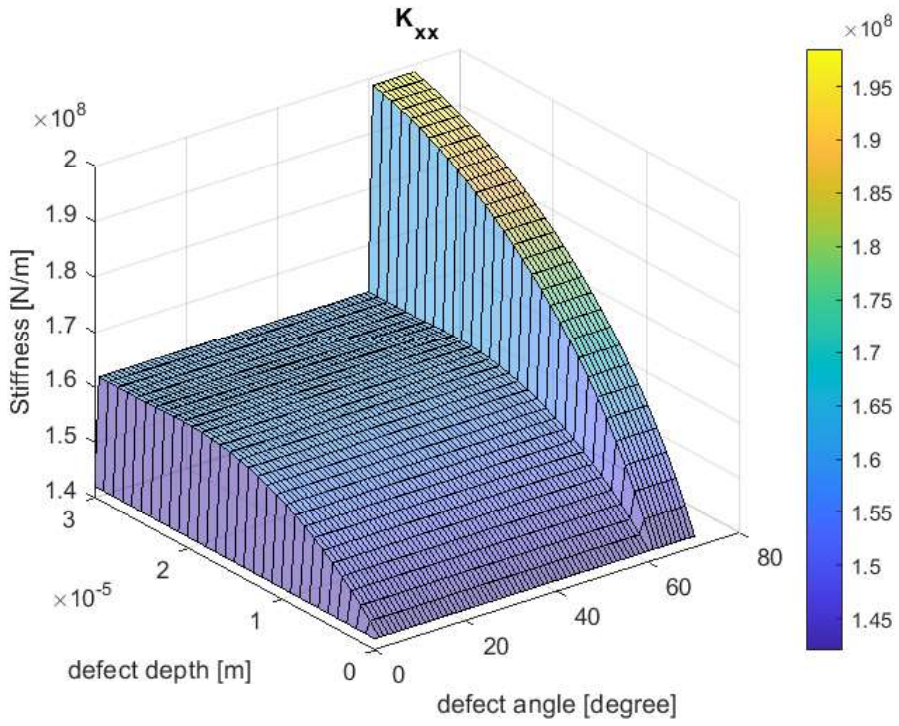

Figure 2.10 Defect Angle & Depth vs K_{xx} Stiffness

Stiffness at x direction can be seen in Figure 2.10. At 0^0 angle and 0 m defect depth graphs show the defect-free stiffness values for the bearing. After these points defect starts. One ball is directly on the defect so from the first angle or depth after zero, effect of the defect starts. Defect angle determines number of the balls inside the

defect. Increasing defect angle do not affect the plot if another ball does not get into the defect or it affects the graph absurdly if another ball gets in the defect. On the other hand, changing defect depth change the graph softly. Increasing defect depth and defect angle both increases the stiffness because defect is not in this direction. When size of defect increases load carried by the balls at this region increases.

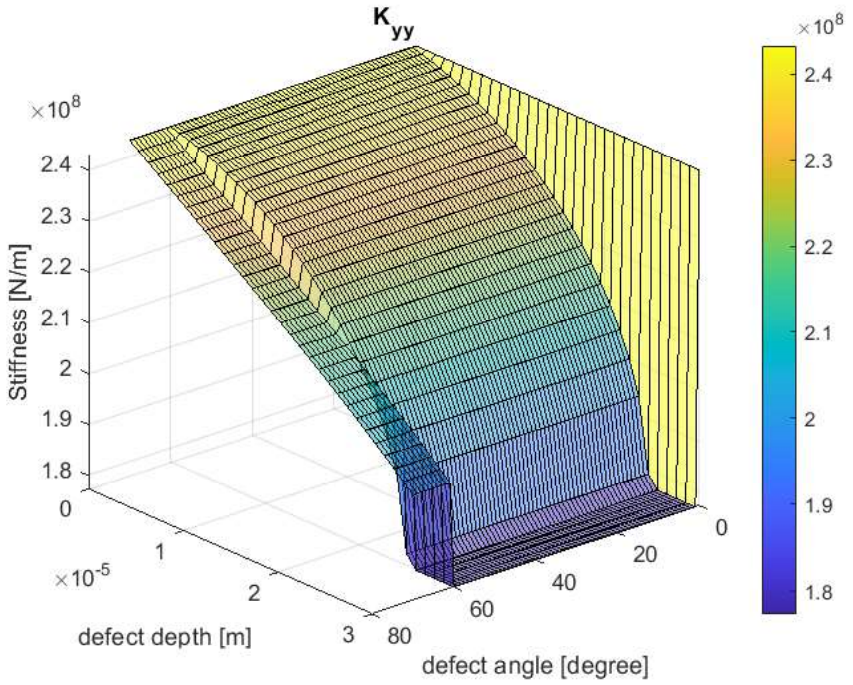

Figure 2.11 Defect Angle & Depth vs K_{yy} Stiffness

Stiffness at y direction can be seen form Figure 2.11. Defect and radial force at the bearing is at this direction. The load that needed to be carried by the balls if there was no defect is not carried by the balls at this region, so stiffness decreases as defect depth and angle increases.

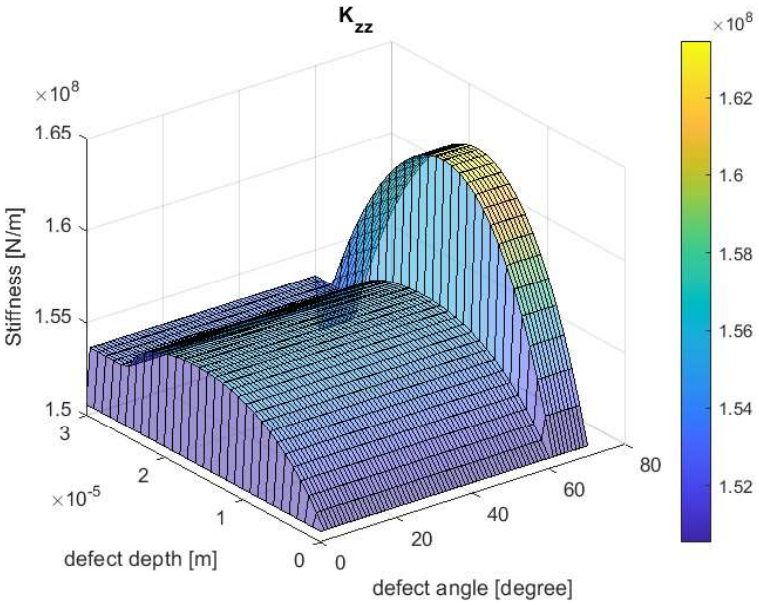

Figure 2.12 Defect Angle & Depth vs Axial Stiffness

Stiffness at axial direction can be seen from Figure 2.12. Stiffness first increases and then decreases as defect depth increase. This is because of non-linear characteristic of Hertz contact. Note that, magnitude of the stiffness change is not as much as radial cases.

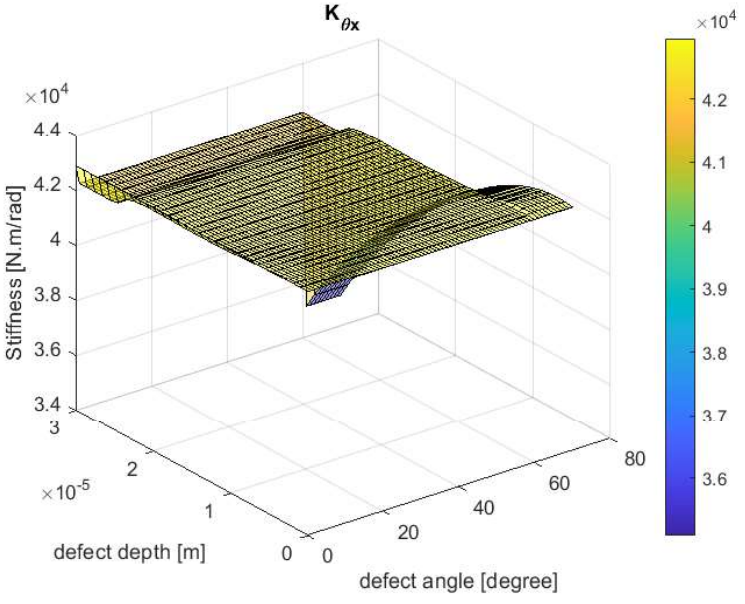

Figure 2.13 Defect Angle & Depth vs Yaw Stiffness

Stiffness at yaw direction can be seen from Figure 2.13. As depth and angle of the defect increase, stiffness at yaw direction decrease. The defect at the bearings is at this direction so an increase at the depth of defect or number of balls at the defected region decreases the stiffness at this direction. When there are there balls at the defect, stiffness changes sharply.

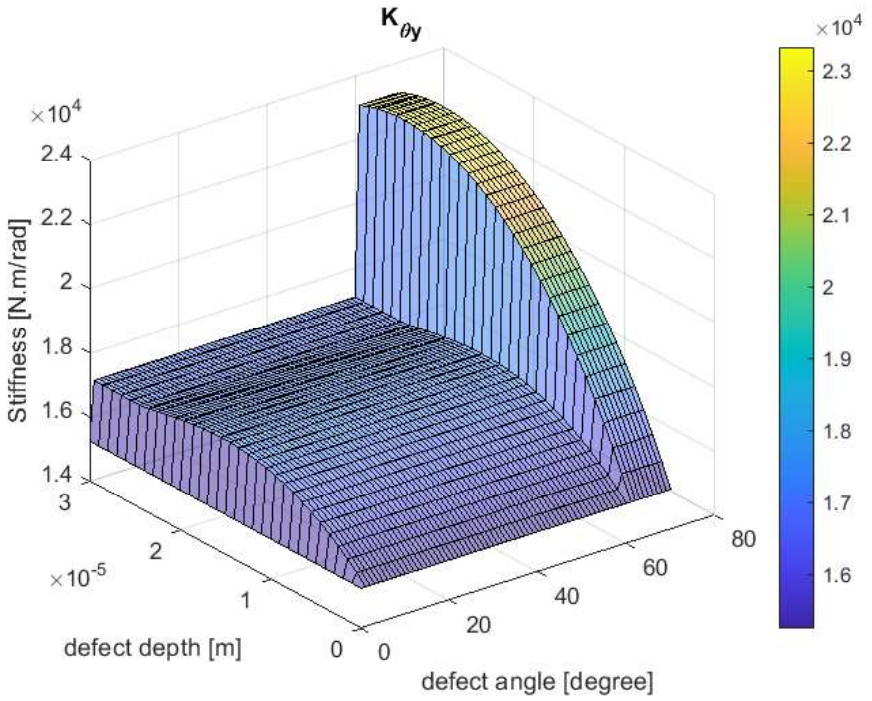

Figure 2.14 Defect Angle & Depth vs Pitch Stiffness

Stiffness at pitch direction can be seen from Figure 2.14. Similarity of graphs of x direction and pitch direction are remarkable. Defect at the bearing is not at these directions so as defect increase, load carried by the balls at this direction increases.

While defect depth increase, balls in the defect lose some part of its load carrying capacity. If depth of the defect continues to increase, load carrying capacity of the ball can become zero, meaning that, all the load which has needed to be carried by the ball, is shared between the other balls. After this point, increasing defect depth does not change the stiffness of the bearing. This phenomenon is called limit depth.

When depth of the defect is constant, if number of balls in the defected region is increase because of increasing defect angle, load carrying capacity of the balls inside the defected region can increase. This directly changes limit depth and stiffness of the bearing.

2.3.2 Effect of the Preload

In this section effect of preload on a defected bearing is investigated. Same bearing is used with a defect at 270^0 but depth and length of defect is changed. 2000 N is applied in the y direction on top of the defect and a load between 0 to 3000 N is applied in the axial direction. Stiffness values of diagonal elements of the stiffness matrix vs defect depth and defect angle are plotted. Graphs of stiffness can be seen from Figure 2.15, Figure 2.16, Figure 2.17, Figure 2.18 and Figure 2.19. In the figures below, at the left graphs the defect angle is 40^0 and at the right graphs the defect depth is 20 μm.

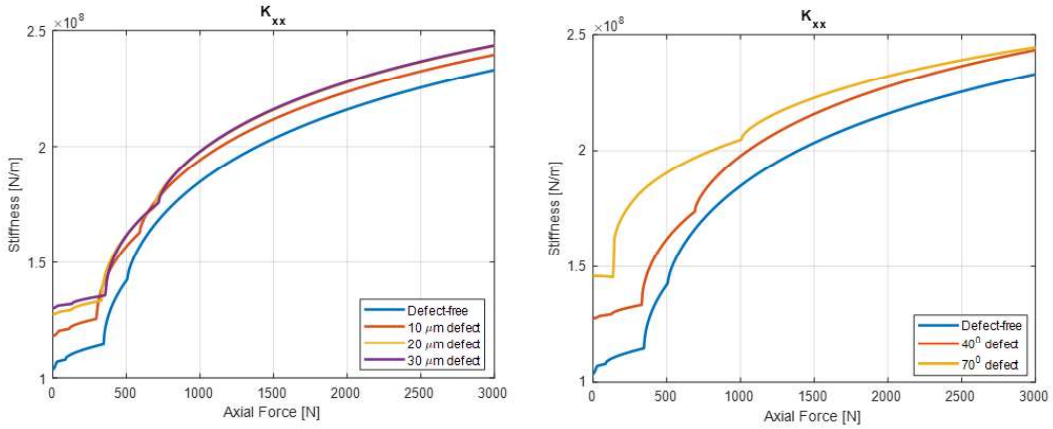

Figure 2.15 K_{xx} Stiffness vs Preload

Stiffness at the x direction can be seen from Figure 2.15. As preload increases, stiffness value increases regardless of defect size or number of balls at defected region.

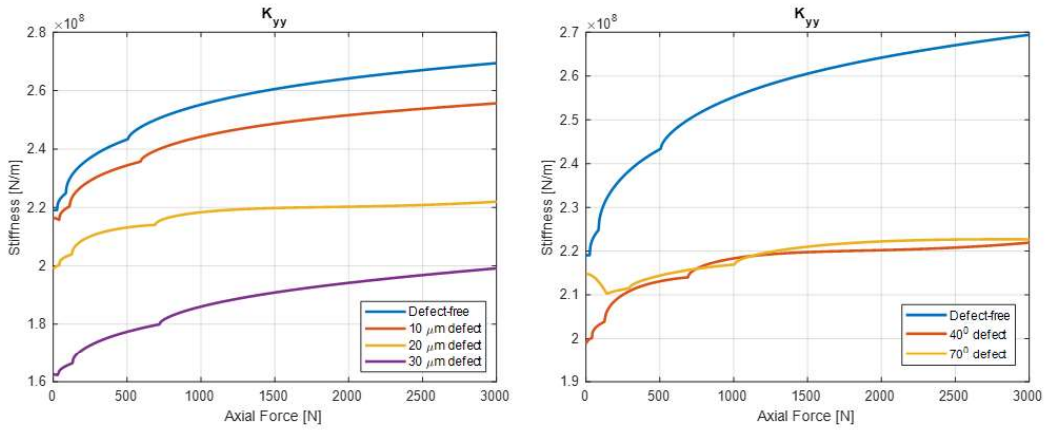

Figure 2.16 K_{yy} Stiffness vs Preload

Stiffness of y direction can be seen from Figure 2.16. Increasing preload does not cause stiffness to increase. Note that, defect is at this direction and there is a radial force acting directly on the defect.

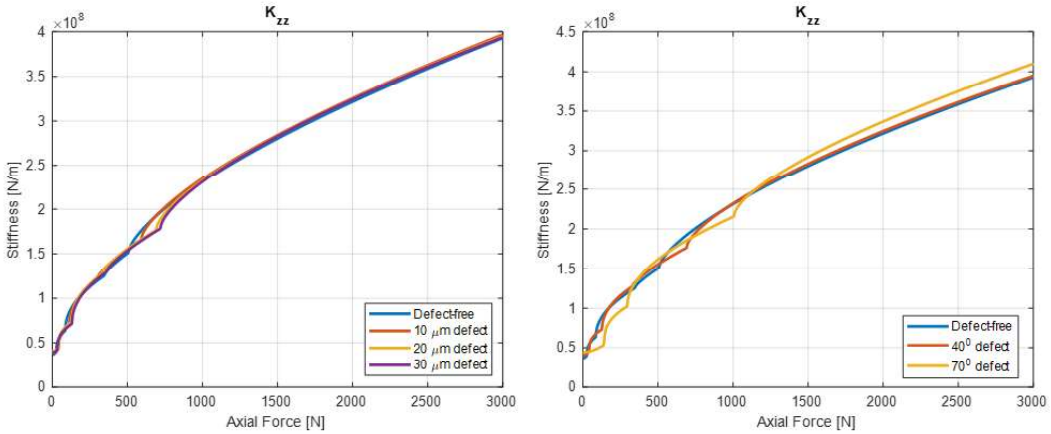

Figure 2.17 Axial Stiffness vs Preload

Stiffness of axial direction can be seen from Figure 2.17. As preload increase, axial stiffness increase as expected. Note that, increase of the magnitude of the stiffness is significantly larger that the radial directions and does not depend on the defect depth and angle.

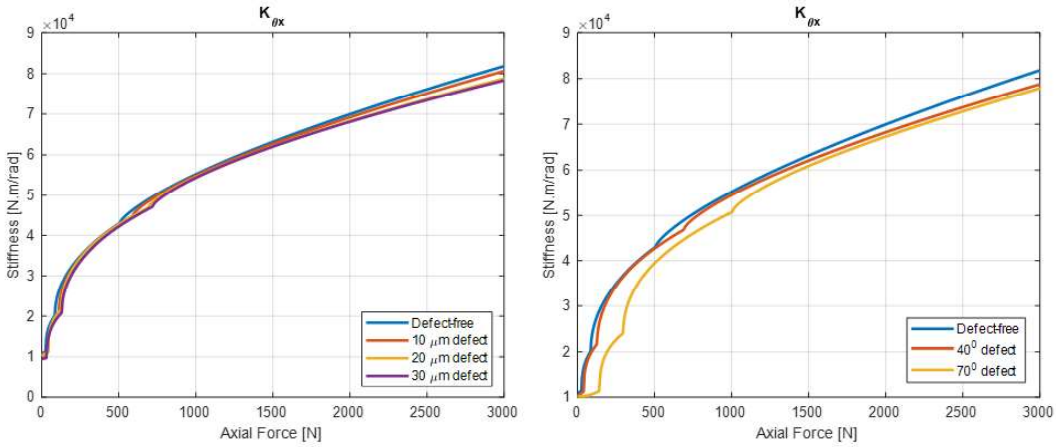

Figure 2.18 Yaw Stiffness vs Preload

Stiffness of yaw direction can be seen from Figure 2.18. As preload reaches to 3000 N, magnitude of the stiffness reaches to nine times of the 0 N value.

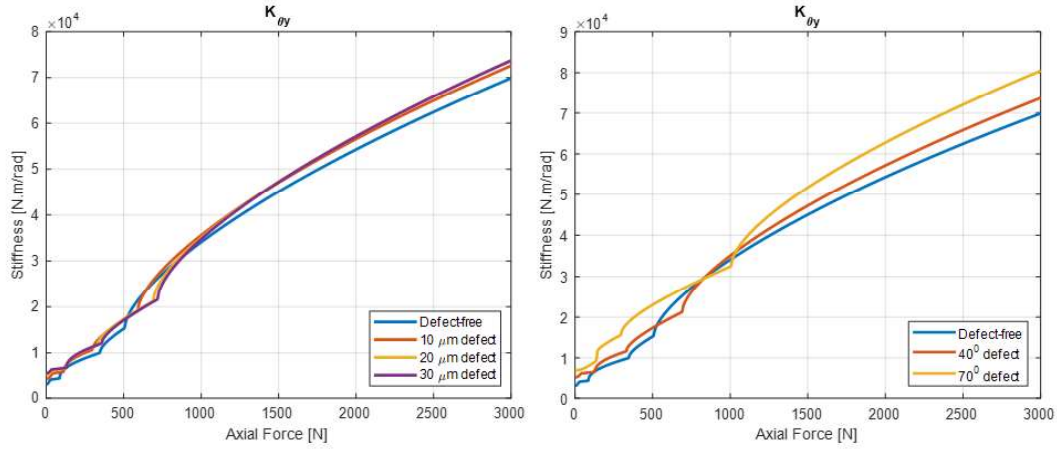

Figure 2.19 Pitch Stiffness vs Preload

Stiffness of pitch direction can be seen from Figure 2.19. As preload increase, stiffness value increase.

At defect free case increase at the preload increases stiffness values at every axes. When a defect is introduced to the bearing, behavior of stiffness values of y direction dissociate from the other axes. It should be noted that, there is a force which has a similar magnitude to preload, directly acting on the defected zone. This is condition is constituted particularly to demonstrate the effect of preload at defected bearings.

2.3.3 Direction of the Force and Position of the Defect

In the previous sections, a radial force acting directly on the defect is introduced to the bearing. In this section, instead of a force acting on the defect, a radial force acting on the defect-free region of the bearing is introduced. At the same time preload is removed. Stiffness values versus depth and angle of defect is plotted and can be seen from Figure 2.20

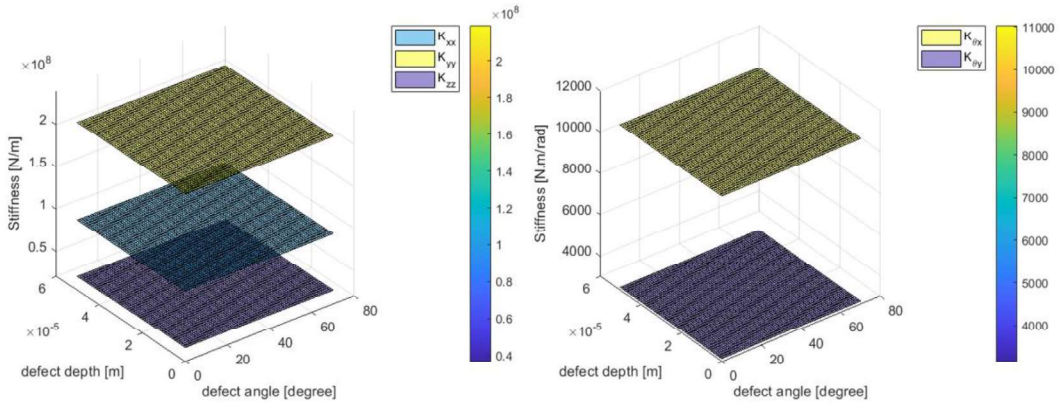

Figure 2.20 Defect Depth & Angle vs Stiffness - Opposite locations of Defect and Loading Zone

As it can be seen from Figure 2.20, stiffness values of the bearing does not change with changing defect depth and length. If loading zone and defected zone of bearing does not intersect, then effect of the defect cannot be seen on the stiffness values. Balls at the defected region loses all or some part of the load on them but since there are no load on the balls at the defected region, size of defect don't effect the stiffness.

CHAPTER 3

MODELING OF SPINDLE-BEARING ASSEMLY

Finite element model of a spindle is constructed. Using the analytical model for bearing stiffness calculation, effect of defected bearings on spindle point FRF is investigated. In addition, effect of bearing damage on tool point FRF is studied with two different tools.

3.1 Spindle Model

A Finite element model of a Royal RD4152 BT40 spindle is constructed. The spindle can be seen from Figure 3.1 is constituted.

Figure 3.1 Royal RD4152 BT40 Spindle

Shaft of the spindle can be seen from Figure 3.2. In addition, solid model of the shaft and dimensions are shown in Figure 3.3 and Figure 3.4 respectively.

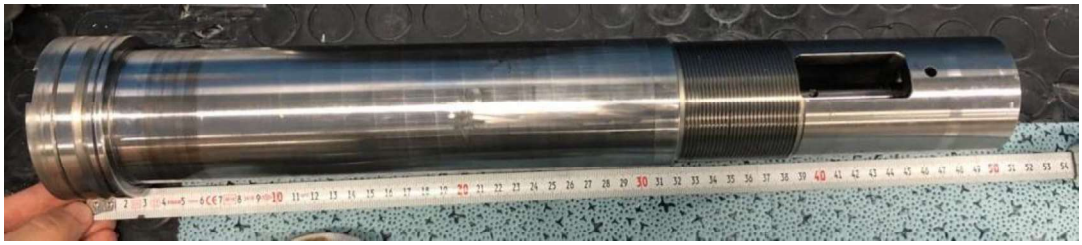

Figure 3.2 Shaft of the Spindle

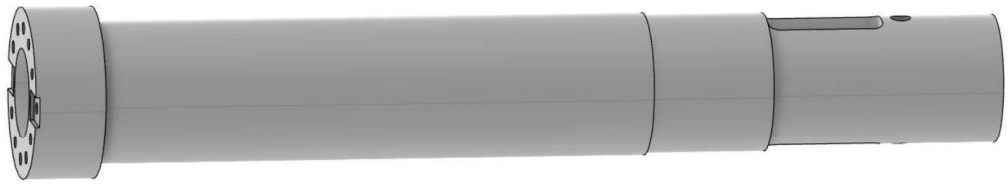

Figure 3.3 Solid Model of the Shaft

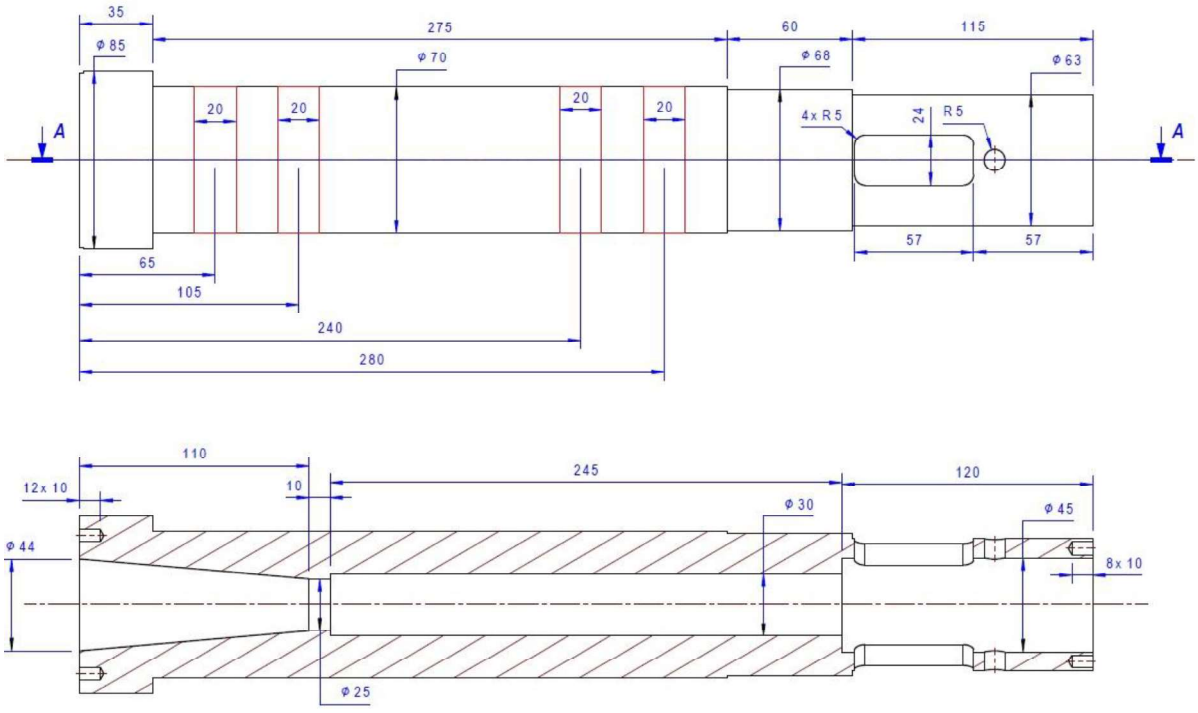

Figure 3.4 Dimensions of the Shaft of the Spindle and Bearing Locations

In addition to spindle shaft, spindle has 4 NSK 70BNR10H bearings between the shaft and housing. Locations of the bearings on the spindle shaft can be seen from Figure 3.4. Red rectangles show the area that bearings sit and distance between face

of the shaft and center points of the areas are shown . These bearings are high-speed angular ball bearings from NSKROBUST Series. They are designed to maintain their high radial rigidity under high-speed operations. Inner and outer races are made of bearing steel (SUJ2) and balls are made of ceramic (Si_3N_4). Poisson Ratio and Young's Modulus of races and balls are given in Table 2. Material of the cage of the bearing is Polyamide resin and it is ball guided. Bearings are placed on the shaft at DBB arrangement with extra light preload. Dimensional accuracy of the bearing is P4 which corresponds to ISO class 4. Dimensions of the bearing are also given in

Table 3.

Table 2 Material Properties of Raceways and Balls

	Bearing Steel (SUJ2)	Ceramic (Si_3N_4)
Young's Modulus	208 GPa	300 GPa
Poisson's Ratio	0.30	0.26

Table 3 Dimensions of the Bearing

Inner Diameter	86 mm
Outer Diameter	94 mm
Ball Diameter	8 mm
Number of Balls	26
Inner Raceway Curvature Radius	4.5 mm
Outer Raceway Curvature Radius	4.5 mm
Radial Clearance	0.05 µm
Contact Angle	18^0

To model the spindle-bearing assembly, a project is created at the ANSYS Workbench to get the natural frequencies, mode shapes and FRF of the shaft of the

spindle. Project schematics can be seen at Figure 3.5. Geometry, modal and harmonic response analysis systems are added to the project.

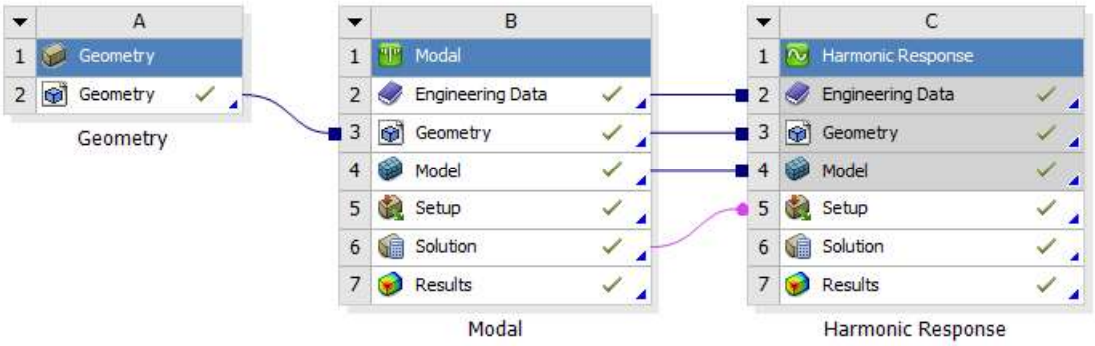

Figure 3.5 Project Schematic

Using ANSYS Mechanical, springs are attached to the shaft at the center of the bearings contact areas aiming to model stiffness of bearings acting on the shaft. Body to ground configuration is selected for the springs. Inner races of the bearings, inner spacers and drawbar which move with the shaft of the spindle, are not included to the model. The model with attached springs can be seen in Figure 3.6.

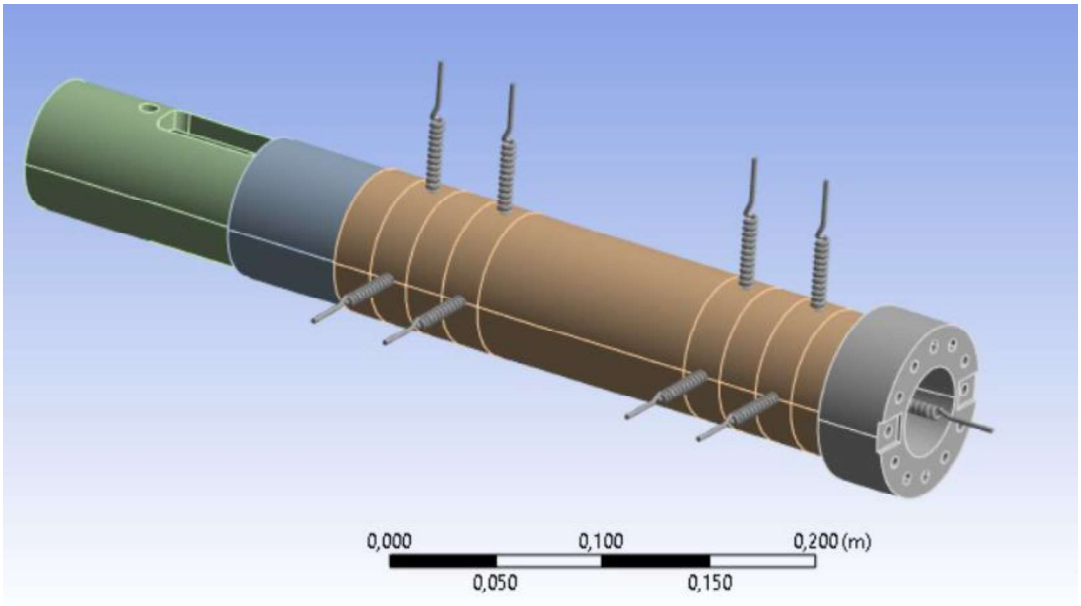

Figure 3.6 Finite Element Model of the Spindle

3.2 Effect of Bearing Defect on Spindle Dynamics

Using the analytical model for bearings, stiffness values for different conditioned bearings are calculated and integrated into the finite element model as inputs to the stiffness values of springs attached to the shaft. Using these stiffnesses different cases are generated for spindle which can be seen from Table 4. Number of bearings are starting from the closest to the tool holding part of the spindle shaft.

Table 4 Bearing Conditions of Cases

	Bearing 1	**Bearing 2**	**Bearing 3**	**Bearing 4**
Case 1	Defect-free	Defect-free	Defect-free	Defect-free
Case 2	30 μm defect	30 μm defect	Defect-free	Defect-free
Case 3	50 μm defect	30 μm defect	Defect-free	Defect-free
Case 4	50 μm defect	50 μm defect	Defect-free	Defect-free
Case 5	100 μm defect	50 μm defect	Defect-free	Defect-free
Case 6	Defect-free	Defect-free	30 μm defect	30 μm defect
Case 7	Defect-free	Defect-free	50 μm defect	50 μm defect

While calculating the stiffness values of bearings only defect depth is changed. Other parameters of stiffness are kept constant. All the calculations are done under 10500 N axial force coming from preload and 25 N force in y direction coming from weight of the shaft.

Resonance frequencies of spindles with different conditioned bearings are calculated for different cases. After that, a point from the tip of the spindle is selected and point FRF is calculated. Structural damping is defined with 0,02 damping ratio and applied to the system. Frequency response (frequency [Hz] vs amplitude [m]) of the spindles are generated for different bearing condition cases. Frequency response functions calculated in ANSYS Mechanical are plotted using MATLAB software.

Stiffness values of defect-free bearings that are on the shaft are calculated using analytical bearing stiffness model and calculated stiffness values are given in Table

5. Then, frequency response function (FRF) at the spindle tip is calculated. Obtained FRF is shown in Figure 3.7.

Table 5 Stiffness Values of Defect-free Bearing

K_{xx}	K_{yy}	K_{zz}	$K_{\theta x \theta x}$	$K_{\theta y \theta y}$
$6.5\ x10^8$ N/m	$6.5\ x10^8$ N/m	$2.4\ x10^8$ N/m	$2.5\ x10^5$ N.rad/m	$2.5\ x10^5$ N.rad/m

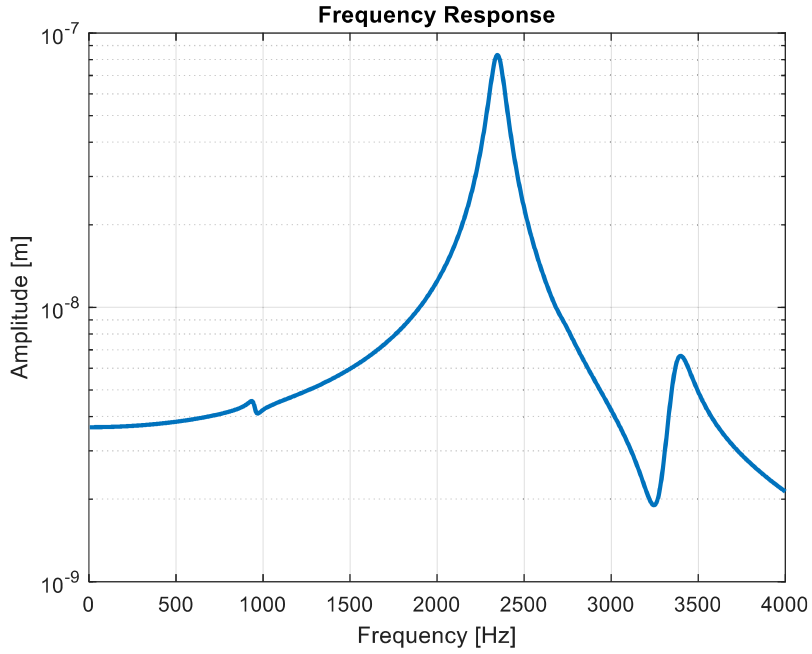

Figure 3.7 Frequency Response of Spindle with Defect Free Bearings

Then, a defect with 30 μm depth and 70^0 length at 270^0 is introduced to the two bearings close to tool clamping part of the shaft. Calculated bearing stiffness values are given in Table 6. Other two bearings, close to the back of the spindle, are kept defect-free.

Table 6 Stiffness Values of a Bearing with Defect depth 30 μm and length 70^0

K_{xx}	K_{yy}	K_{zz}	$K_{\theta x \theta x}$	$K_{\theta y \theta y}$
$6.8\ x10^8$ N/m	$5.6\ x10^8$ N/m	$2.5\ x10^8$ N/m	$2.3\ x10^5$ N.rad/m	$2.8\ x10^5$ N.rad/m

Calculated FRF at the spindle tip is shown in Figure 3.8 along with the defect-free condition.

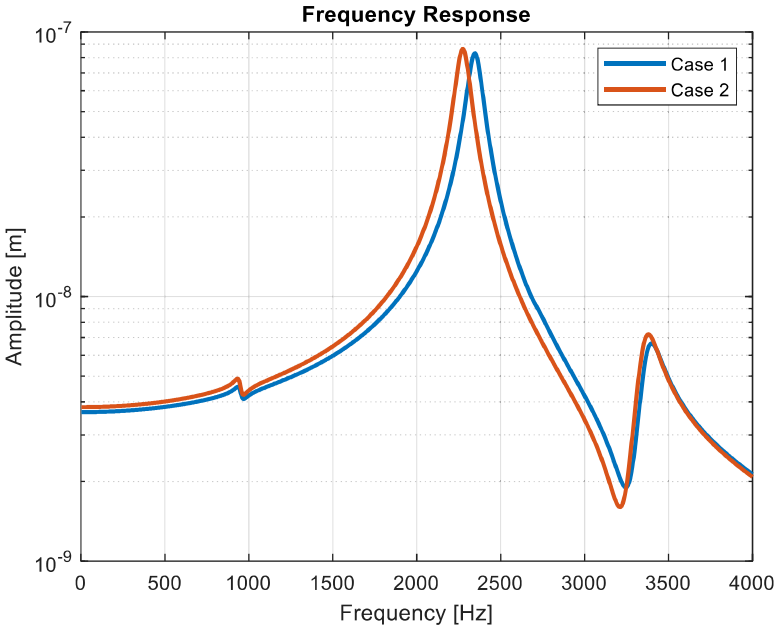

Figure 3.8 Frequency Response of Spindle with 30 Mikron Defected Front Bearings Along with Defect Free Condition

As seen from Figure 3.8, defect in front bearings directly effects the spindle dynamics, hence the spindle tip FRFs. For instance, the dominant mode located at the 2344 Hz is shifted to the 2268 Hz and the third mode located at 3392 Hz is shifted to the 3380 Hz.

In addition, a 50 μm depth and 70^0 depth is introduced to the bearing at the front. Stiffness values of the bearing can be seen from Table 7. Second bearing from the front of the spindle is the defected bearing used in case 2 which has 30 μm defect depth and stiffness values is given in Table 6. Two bearings at the back are defect-free.

Table 7 Stiffness Values of a Bearing with Defect depth 50 μm and length 70^0

K_{xx}	K_{yy}	K_{zz}	$K_{\theta x\theta x}$	$K_{\theta y\theta y}$
6.7 $x10^8$ N/m	4.3 $x10^8$ N/m	2.3 $x10^8$ N/m	1.8 $x10^5$ N.rad/m	2.9 $x10^5$ N.rad/m

Calculated FRF at the spindle tip is shown in Figure 3.9 along with the defect-free and 30 μm defected conditions.

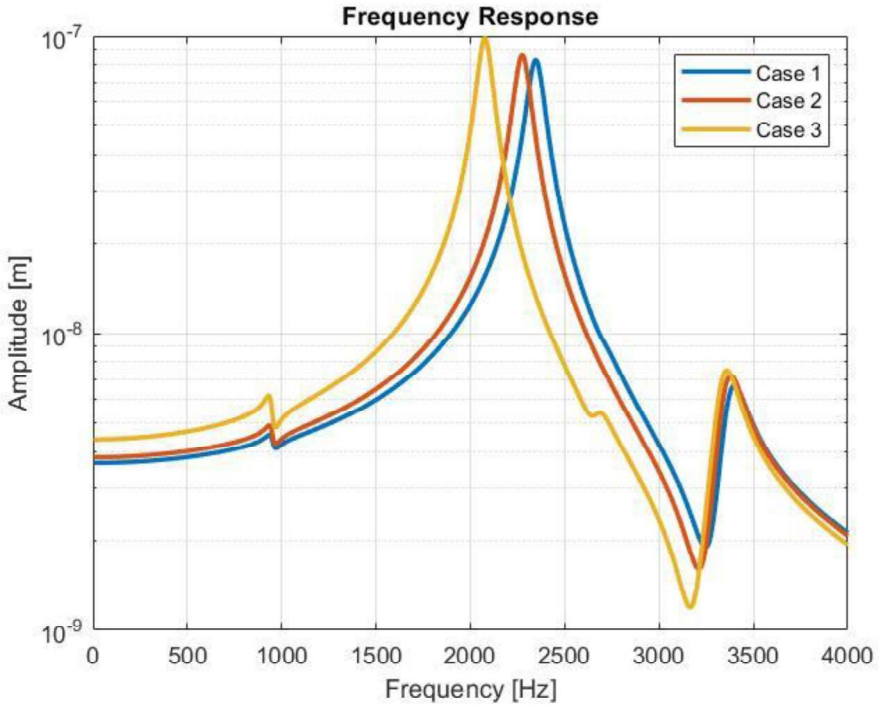

Figure 3.9 Frequency Response of Spindle with 50 Mikron and 30 Mikron Defected Front Bearings Along with Defect Free and 30 Micron Defected Conditions

As seen from Figure 3.9, larger defect at the front bearing effects the FRF of the spindle. For instance, dominant mode located at the 2272 Hz is shifted to 2076 Hz and the third mode at 3384 Hz is shifted to the 3356 Hz.

Same defect that is introduced to the first bearing of the spindle, is introduced to the second bearing of the spindle. FRF of the spindle with 50 μm defected front bearings and defect-free rear bearings are given in Figure 3.10. along with the defect-free and lighter defected conditions.

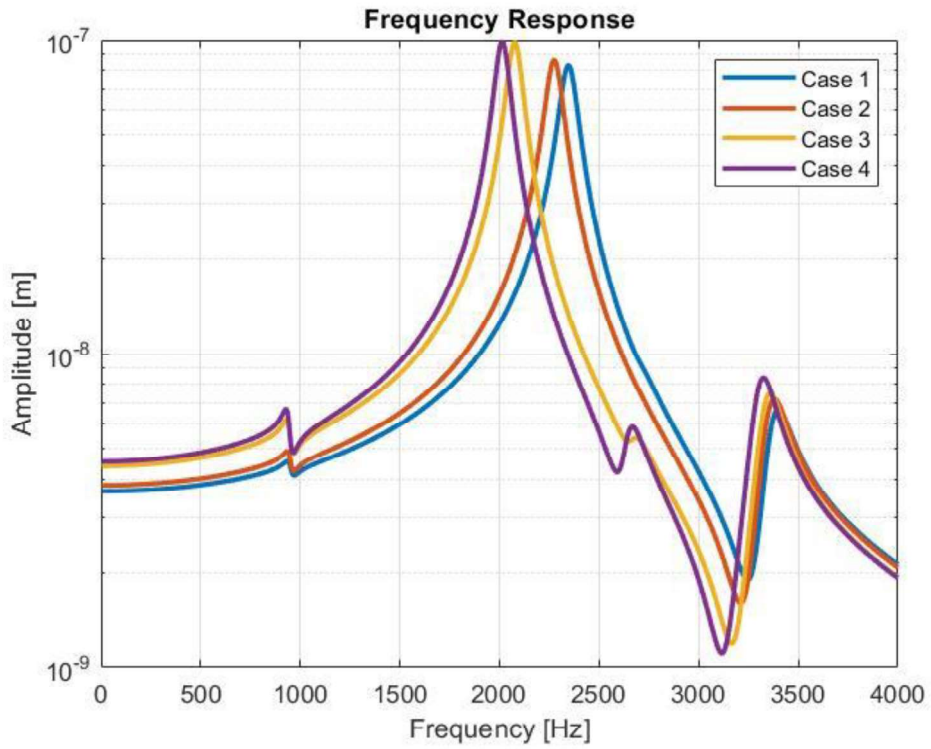

Figure 3.10 Frequency Response of Spindle with 50 Mikron Defected Front Bearings Along with Defect Free, 30 Micron and 50-30 Mikron Defected Conditions

As seen from Figure 3.10, increasing defect depth at the second bearing effects the dynamics of the spindle and changes the tip FRF of the spindle. the dominant mode is shifted to 2016 Hz from 2076 Hz and third mode is shifted to 3324 Hz from 3356 Hz. Note that, effect of the increasing defect depth at the second bearing on the dominant mode, is not as much the effect of the increasing defect depth at the first bearing.

A 100 μm depth is introduced to the bearing at the front. Stiffness values of the bearing can be seen from Table 8. Defects at other bearings are kept constant. Second bearing has 50 μm defect and rear bearings are defect-free. Tip point FRF of the spindle can be seen in Figure 3.11, along with the previous cases.

Table 8 Stiffness Values of a Bearing with Defect depth 100 μm and length 70^0

K_{xx}	K_{yy}	K_{zz}	$K_{\theta x\theta x}$	$K_{\theta y\theta y}$
6.7 $x10^8$ N/m	3.7 $x10^8$ N/m	2.1 $x10^8$ N/m	1.6 $x10^5$ N.rad/m	2.9 $x10^5$ N.rad/m

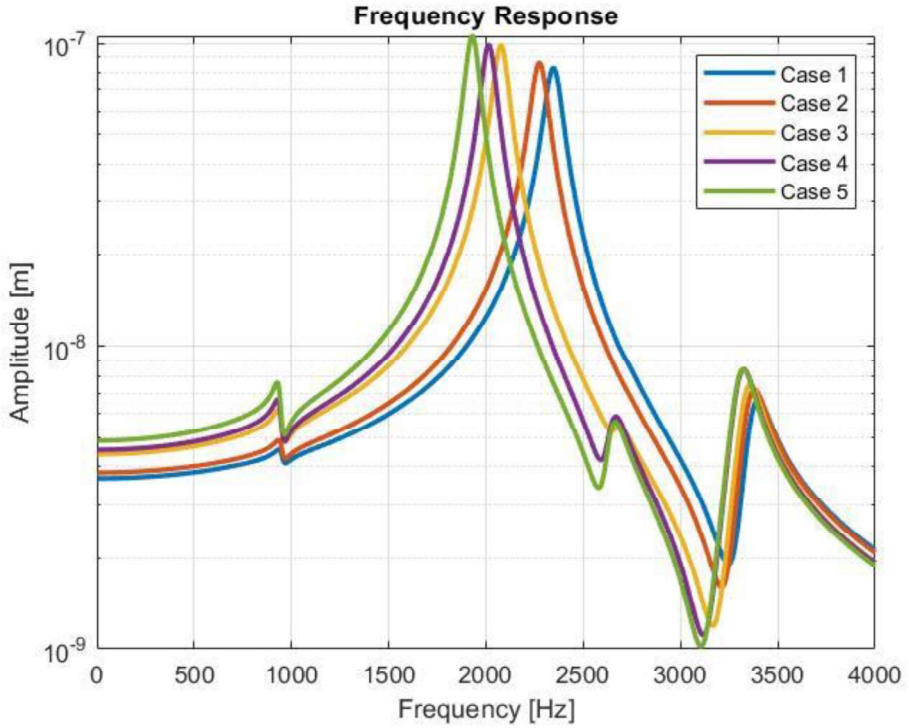

Figure 3.11 Frequency Response of Spindle with 50 Mikron and 100 Micron Defected Front Bearings Along with Defect Free, 30 Micron, 30-50 Mikron and 50 Mikron Defected Conditions

As seen from Figure 3.11, increasing defect depth at the front bearing effects the tip point FRF of the spindle. For example, the dominant mode is shifted to1928 Hz from 2016 Hz and the third mode is shifted to 3324 Hz from 3320 Hz. Note that, increasing defect depth of the front bearing second time did not affected the tip point FRF of the spindle as much as first attempt. Third mode of the spindle changed slightly.

Defect at the front bearings is retrieved and a defect with 30 μm depth is introduced to the rear bearings. Stiffness values of defect-free bearings is given in Table 1 and

stiffness values of 30 µm bearings are given in Table 6. Tip point FRF of the spindle is given in Figure 3.12, alongside with the defect-free condition.

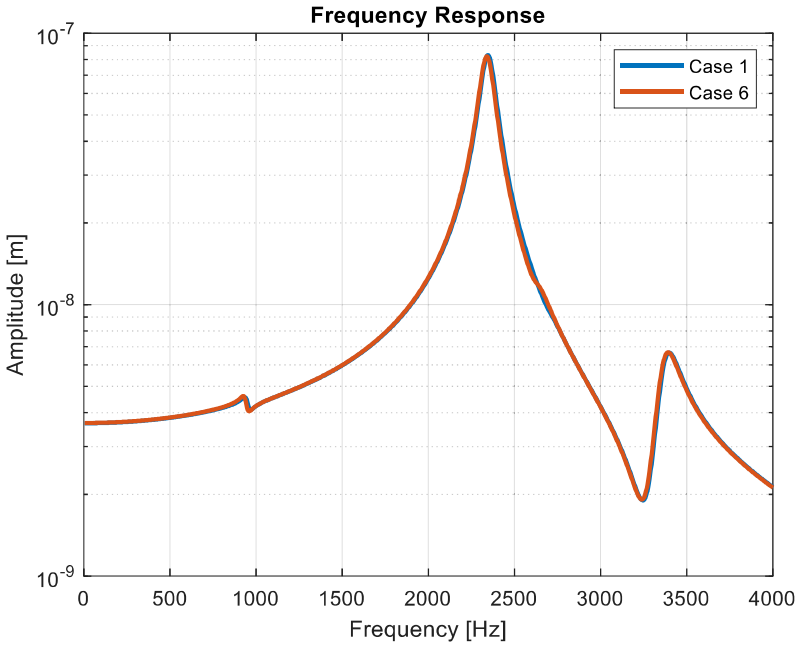

Figure 3.12 Frequency Response of Spindle with 30 Mikron Defected Rear Bearings Along with Defect Free Condition

As seen from Figure 3.12, introducing 30 µm defect at the rear bearings does not change the tip point FRF of the spindle. When tip point FRF is considered, front bearings are more dominant compared to rear bearings.

Depth of defect at the rear bearings are increased to 50 µm while front bearings are kept defect-free. Stiffness values for 50 µm are given in Table 7. Tip point FRF of the spindle is given in Figure 3.13, alongside with the defect-free and 30 µm defect depth conditions.

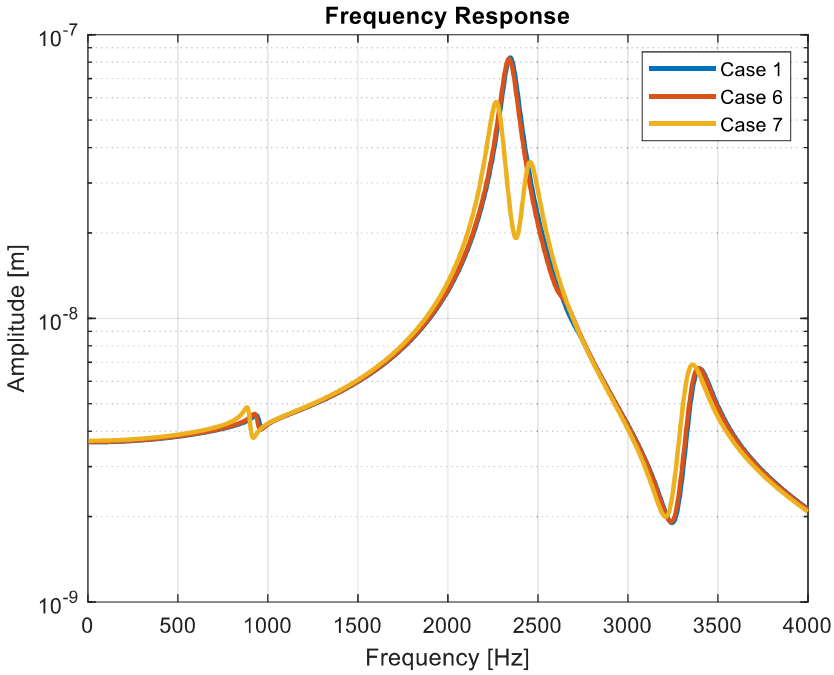

Figure 3.13 Frequency Response of Spindle with 50 Mikron Defected Rear Bearings Along with Defect Free and 30 Micron Defected Conditions

As seen from Figure 3.13, dominant mode of the spindle splits and creates two peaks. Mode at the 3404 Hz shifts to 3372 Hz. There is a slight change at the point FRF of the spindle but when compared to the 50 mikron defected front bearings, change is insignificant.

3.3 Effect of Bearing Defect on Tool Point FRF

In addition to spindle dynamics, to investigate the effect of bearing defects on tool point FRFs, tool holder and tool are modeled using CATIA software and attached to shaft of the spindle. Tool holder can be seen in Figure 3.14.

Two different tools with different geometries (short-thick & long-slender), are modeled and same analysis are conducted on the spindle to investigate the relation between tool geometry and bearing defects on tool point FRF of the spindle.

Figure 3.14 Tool Holder

3.3.1 Short-Thick Tool

Solid model of holder, tool and the shaft can be seen in Figure 3.15. Dimensions of holder and tool is given in Figure 3.16. Note that geometry of the fluted section was not included in the model and tool is modeled as a simple cylinder.

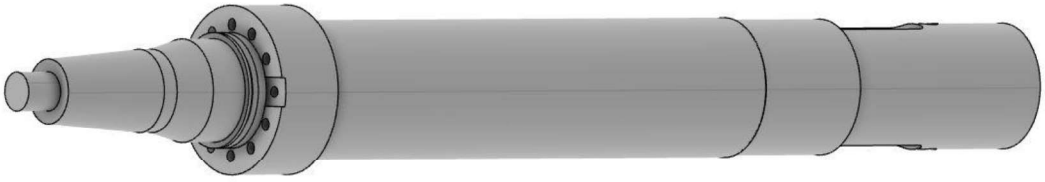

Figure 3.15 Solid Model of Shaft, Tool Holder, and Tool

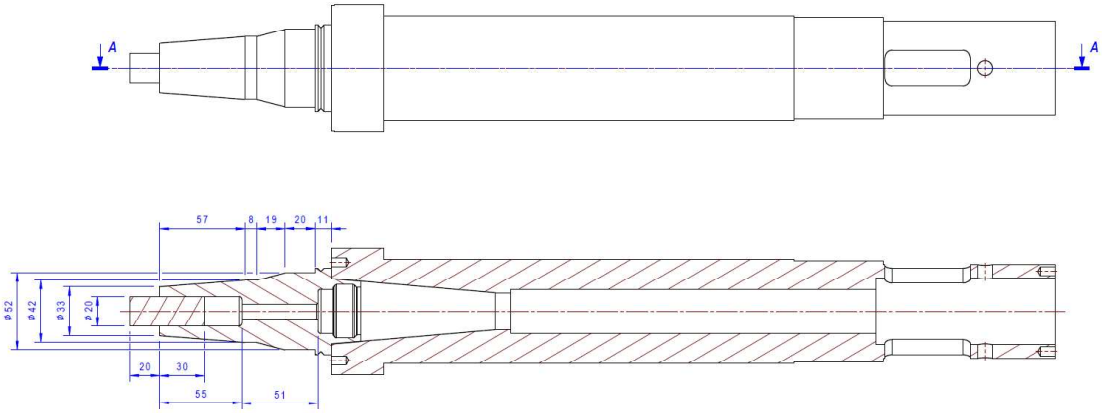

Figure 3.16 Dimensions of Tool Holder and Tool

A point form the tool tip is selected and tool point FRF is calculated. Other than this, all the parameters and assumptions are same with the model of shaft. Same bearings are used at same locations. Finite element model of the spindle can be seen in Figure 3.17.

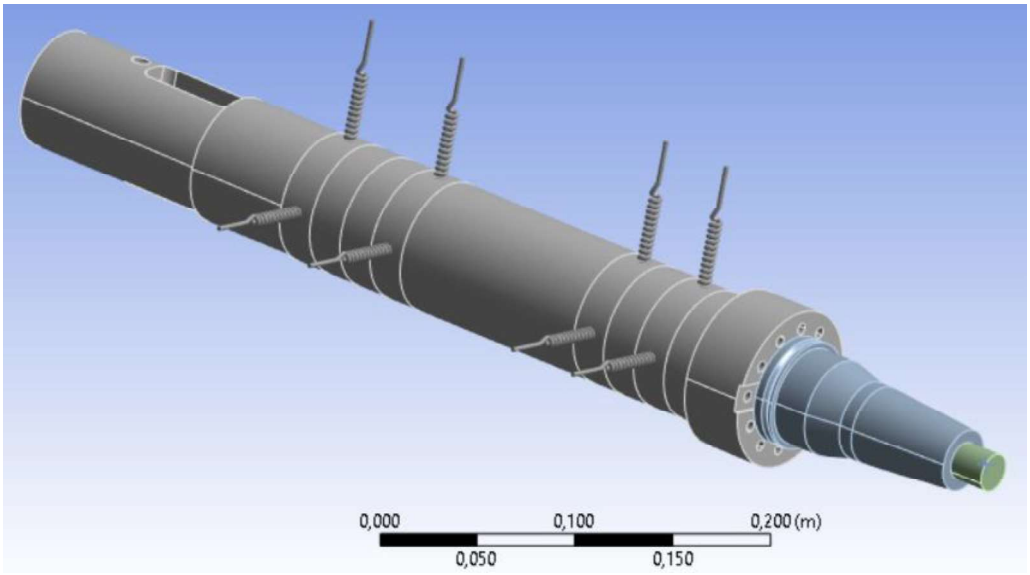

Figure 3.17 Finite Element Model of Shaft, Tool Holder, and Tool

FRF at the tool tip of the shaft-holder-tool assembly is calculated for three different cases. One with defect-free bearings , one with 50 µm defected bearings at front of the shaft and one with 50 µm defected bearings at rear of the shaft . Bearing conditions at the cases are given Table 9.

Table 9 Bearing Condition of Cases

	Bearing 1	**Bearing 2**	**Bearing 3**	**Bearing 4**
Case 1	Defect-free	Defect-free	Defect-free	Defect-free
Case 2	50 µm defect	50 µm defect	Defect-free	Defect-free
Case 3	Defect-free	Defect-free	50 µm defect	50 µm defect

Tool point FRF of the spindle including tool and holder with defect-free bearings is given in Figure 3.18.

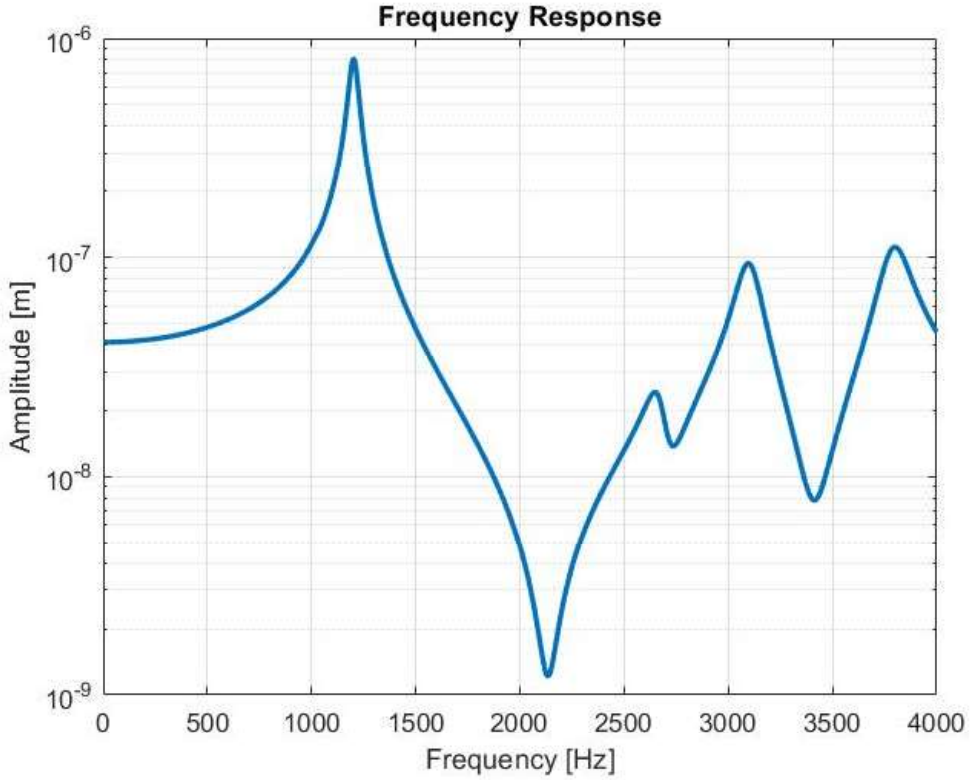

Figure 3.18 Tool point FRF of Spindle with Defect Free Bearings

A defect with 50 µm depth is introduced to the front bearings of the spindle. Rear bearings are defect-free. Tool point FRF of the spindle is plotted and can be seen in Figure 3.19, along with defect-free case.

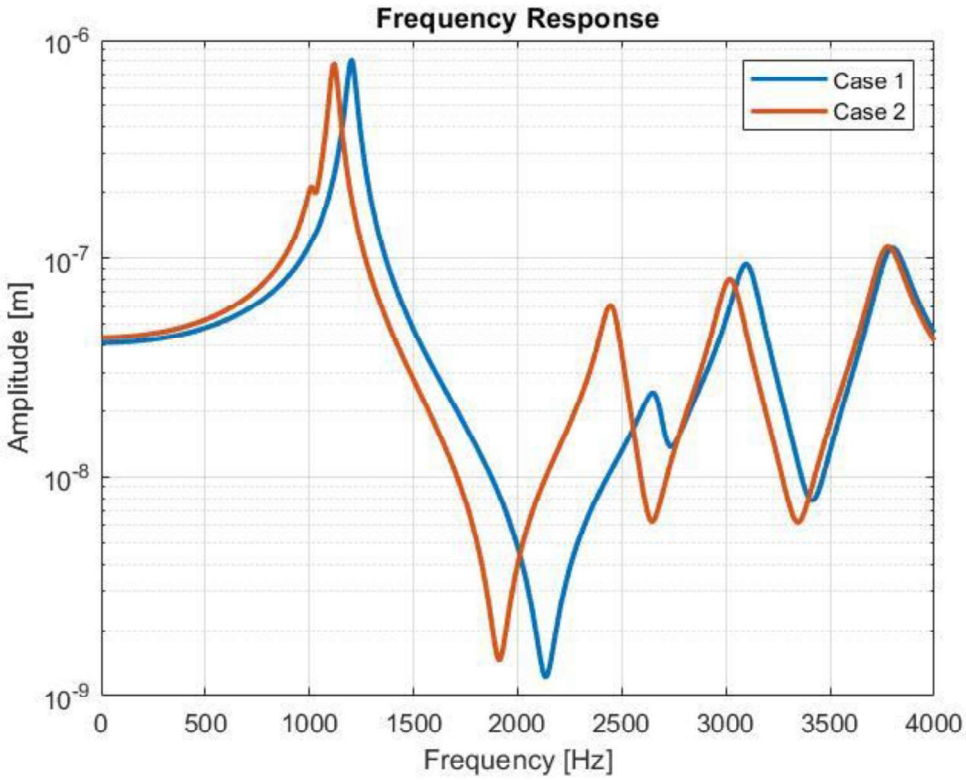

Figure 3.19 Tool point FRF of Spindle with 50 Micron Defected Front Bearings Along with Defect Free Condition

As seen from the Figure 3.19, overall of the plot shifts to the smaller frequencies. Dominant mode of the system shifts to 1116 Hz from 1208 Hz. Mode at the 2656 Hz shifts to 2444 Hz and amplitude increases. Mode at the 3100 Hz shifts to 3012 Hz.

A defect with 50 mikron is introduce to the rear bearings of the spindle and FRF is plotted. FRF of case 3 can be seen from Figure 3.20, alongside with the case 1.

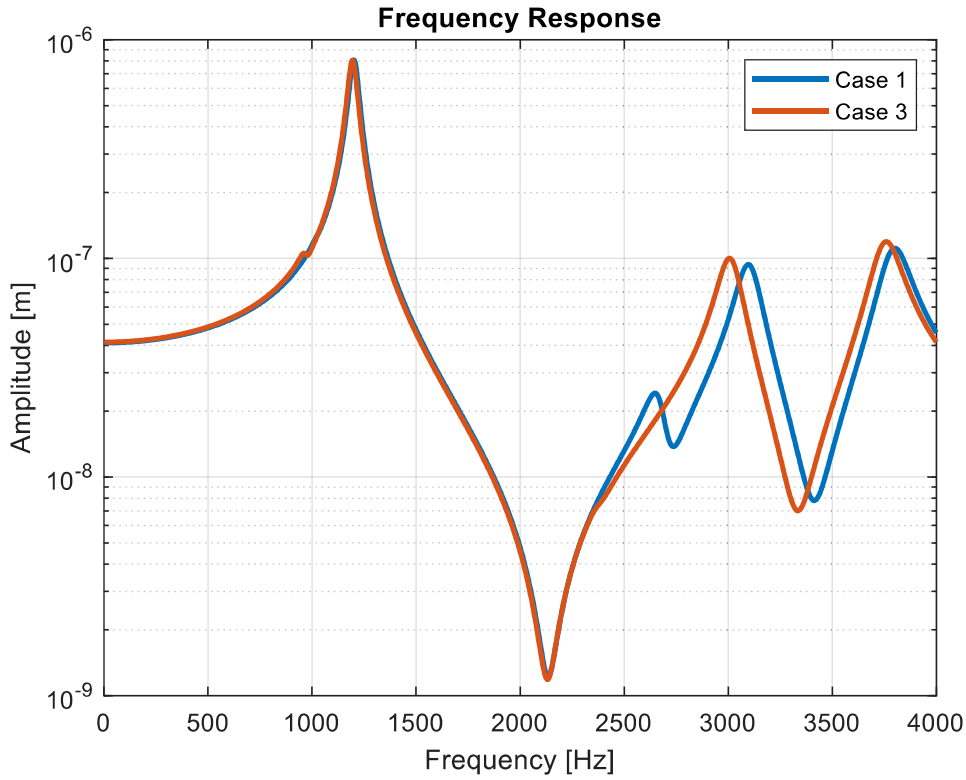

Figure 3.20 Tool point FRF of Spindle with 50 Micron Defected Rear Bearings Along with Defect Free Condition

As seen from Figure 3.20, the dominant mode of the FRF does not change. Mode at the 3100 Hz shifts to 3004 Hz and mode at the 3812 Hz shifts to 3752 Hz. The mode at 2656 Hz disappears. As expected, defected rear bearings effects tool point FRF of the spindle less compared to defected front bearings. Note that, mode splitting does not occur for this case.

3.3.2 Long-Slender Tool

To analyze the effect of bearing defects on tool point FRF for flexible tools, 10 mm diameter solid end mill with 70 mm stick out length is clamped to the same spindle-bearing-holder assembly used in previous section. Solid model of holder, tool and the shaft can be seen in Figure 3.21. Dimensions of the tool is also given in Figure

3.22. Note that geometry of the fluted section was not included in the model and tool is modeled as a simple cylinder.

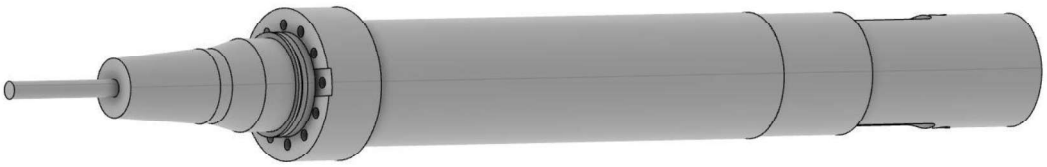

Figure 3.21 Solid Model of Shaft, Tool Holder, and Tool

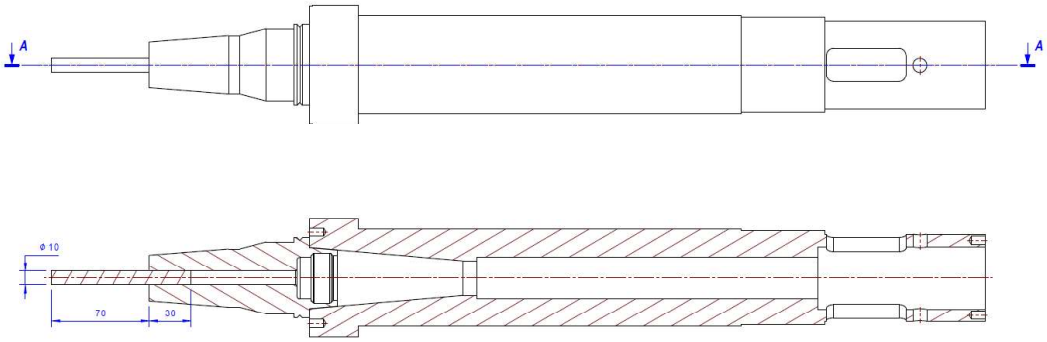

Figure 3.22 Dimensions of the Tool

Harmonic analysis is conducted and tool point FRF is calculated. Note that, same tool holder is used, only tool interface is adjusted according to new tool. Same bearings are used at same locations. Finite element model of the spindle can be seen from Figure 3.23.

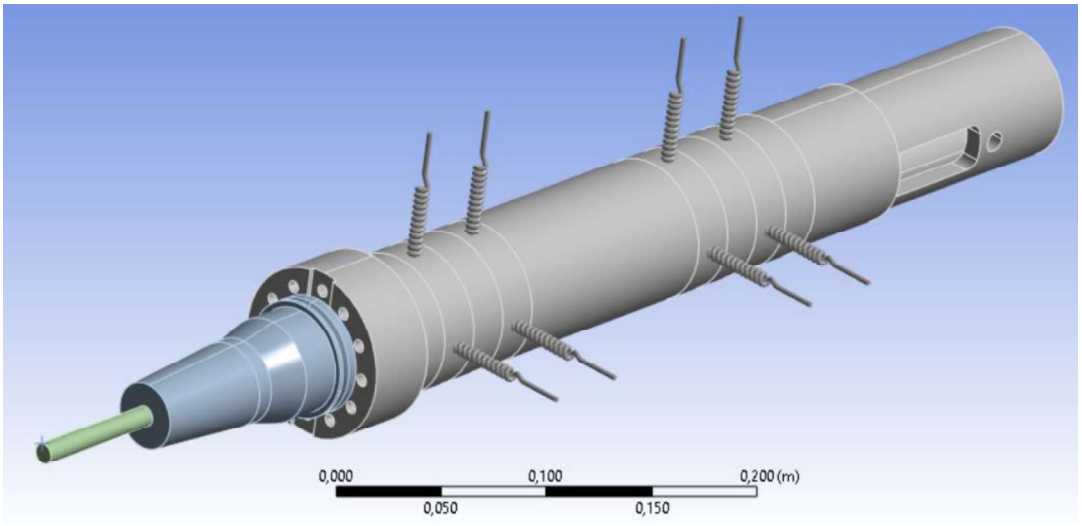

Figure 3.23 Finite Element Model of Spindle and holder with Slender Tool

FRF of the shaft-holder-tool assembly is calculated for two different cases. One with defect-free bearings and one with 50 μm defected bearings at front of the shaft. Bearing conditions at the cases are given in Table 10.

Table 10 Bearing Condition of Cases

	Bearing 1	**Bearing 2**	**Bearing 3**	**Bearing 4**
Case 1	Defect-free	Defect-free	Defect-free	Defect-free
Case 2	50 μm defect	50 μm defect	Defect-free	Defect-free

Tool point FRF of the assembly including slender tool and holder with defect-free bearings is given in Figure 3.24.

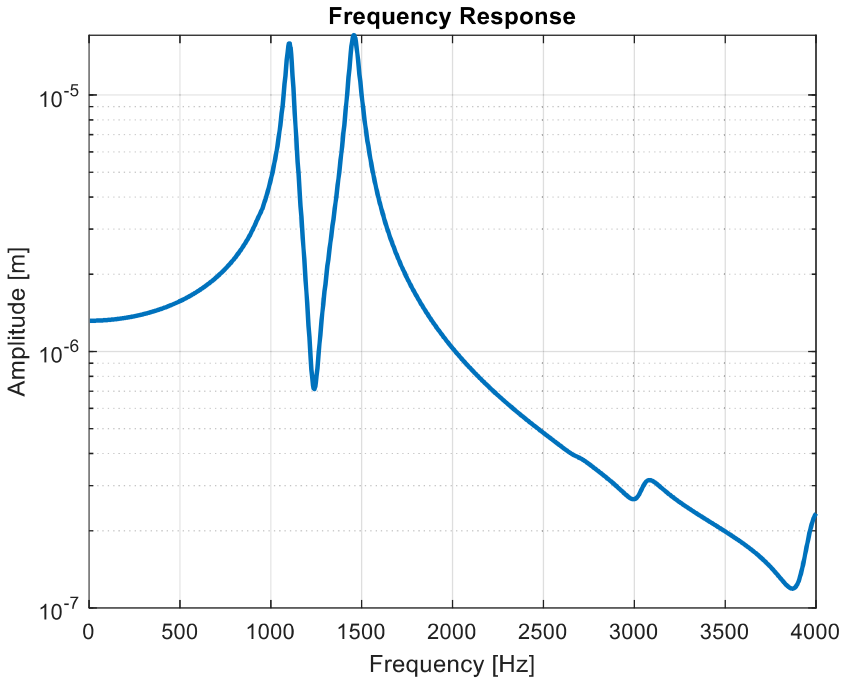

Figure 3.24 Tool point FRF of Spindle with Defect Free Bearings

There are two dominant modes of the system at 1104 Hz and 1160 Hz. Note, that amplitudes of tool point FRF of the spindle with slender tool are 10-20 times larger than previous cases.

A defect with 50 μm depth and 70^0 is introduced to the first two bearings of the spindle. Rear bearing are kept defect free. Tool point FRF of the spindle can be seen in Figure 3.25.

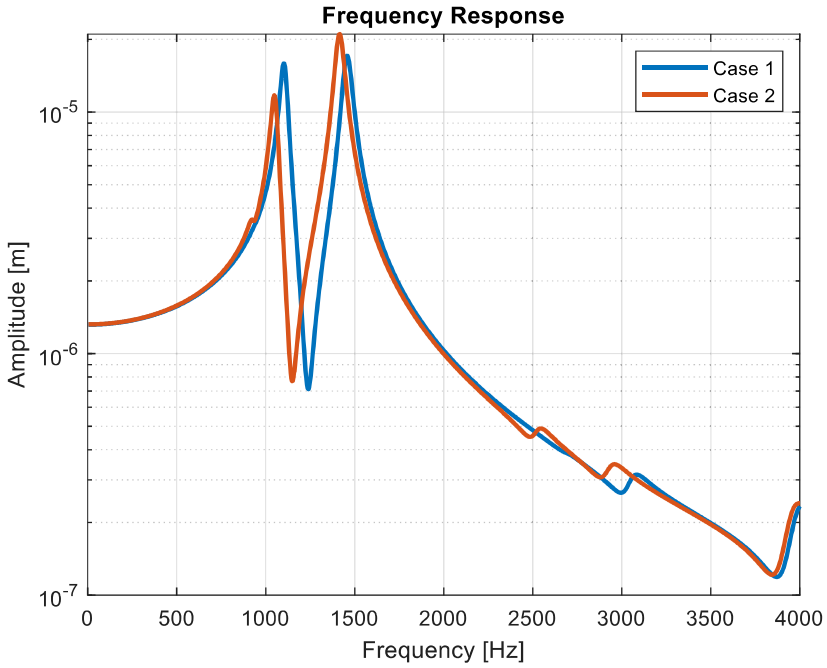

Figure 3.25 Tool point FRF of Spindle with 50 Micron Defected Front Bearings Along with Defect Free Condition

As seen from Figure 3.25, mode at the 1104 Hz is shifted to 1048 Hz and mode at 1160 Hz is shifted to the 1416 Hz. Dominant modes are shifted but compared to thick tool graphs, these shifts can be tiny.

One can conclude that, tool point FRF of the spindle-holder-tool system with a thick tool is more sensitive to the stiffness of the bearings compared to the spindle-holder-tool system with slender tool. Depth of defect directly effects the stiffness of the bearings, so the spindle system with slender tool is less sensitive to bearing faults compared to the spindle system with thick tool.

CHAPTER 4

EXPERIMENTAL

4.1 Modal Test

Modal testing is an accepted way of identifying the vibrations of a system by applying a known force and measuring the response of the system to the force. Measurement of input and output of the system can be used to calculate frequency response of the system.

Impact test is one of the most common types of modal testing. It is started to be used at late 1970's and became popular since it is convenient, non-destructive, fast, and low-cost way of finding modes of systems [73]. A modal hammer is used to apply the force and an accelerometer, attached on the structure, is used for measuring the response. The hammer excites a wide bandwidth by transmitting an impulse type of force to the system. Type of the impact hammer, hardness of the tip is selected according to the structure and bandwidth of focus. The frequency response function (FRF) is plotted using the output of hammer and accelerometer.

4.1.1 Test Setup

An accelerometer is attached to the shaft of the spindle. An impact hammer with plastic tip is used for exiting the system. Data is collected using NI-9425 (National Instruments). CutPro simulation software is used for processing the output of the impact hammer and accelerometer. The data acquisition system, the impact hammer, accelerometer, and the spindle can be seen from Figure 4.1.

Figure 4.1 Test Setup

4.1.2 Test Results Before and After Maintenance

Accelerometer is mounted on outer part of the shaft of the spindle. Location of the accelerometer can be seen in Figure 4.2. Force is applied in the y direction according to given coordinate system in previous chapters, to the shaft directly to the back of the accelerometer. For each measurement 6 hits are done. Same test is repeated for 2 different conditions of the same spindle: before and after the maintenance.

Figure 4.2 Sensor Location

Several tests are conducted, and best results are selected considering coherence. FRF of the spindle before and after the maintenance can be seen in Figure 4.3. Coherence of the test done before and after the maintenance can be seen in Figure 4.4.

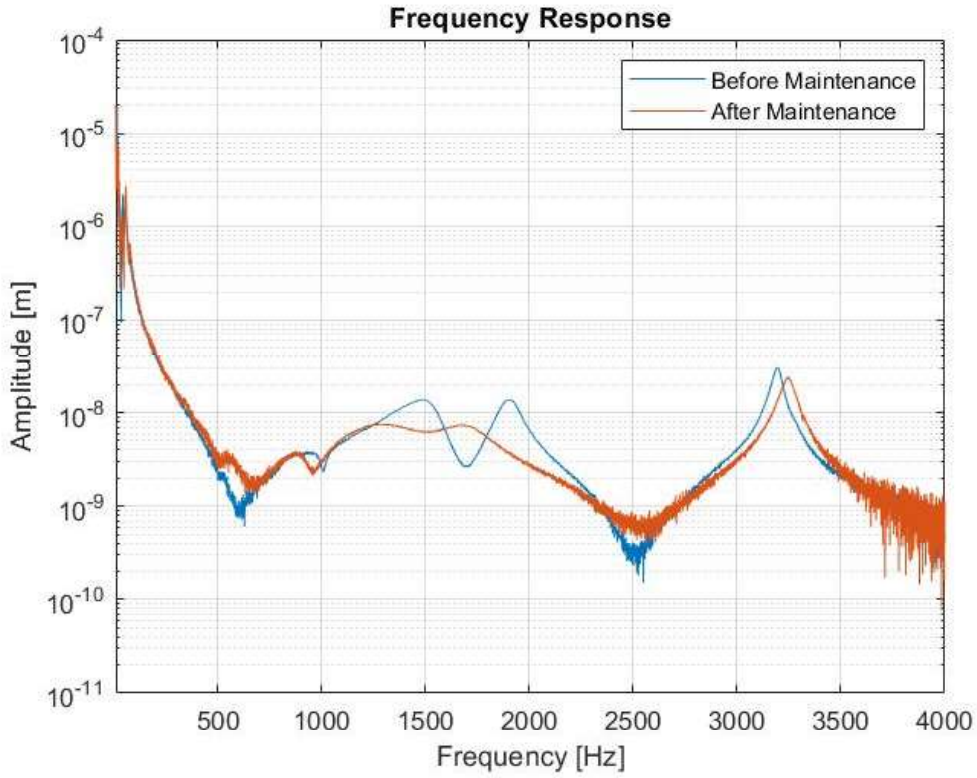

Figure 4.3 FRF of the Spindle Before and After the Maintenance

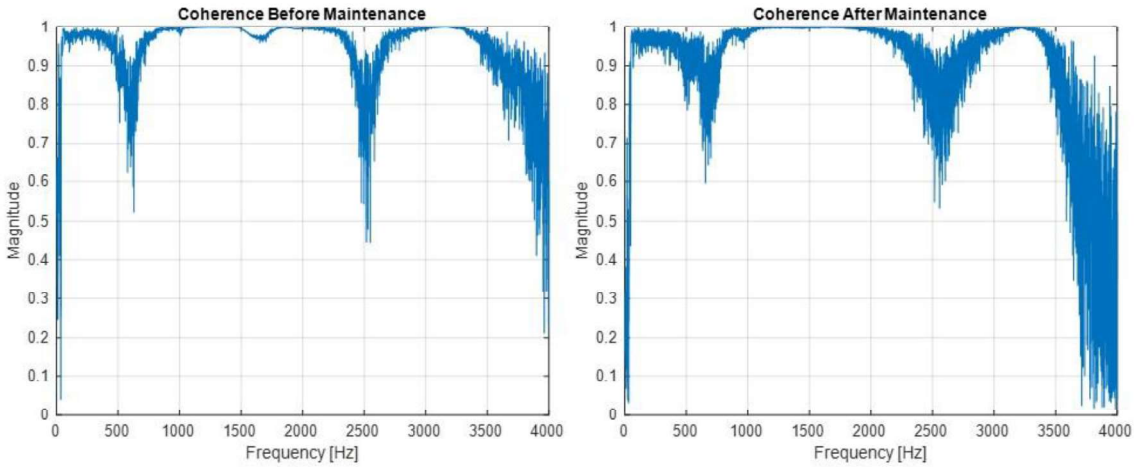

Figure 4.4 Coherence of the Test Before and After Maintenance

As seen from Figure 4.3 and Figure 4.4, coherence drops at antiresonance frequencies as expected and resolution of FRF graphs decrease at these frequencies.

Before maintenance, there are 3 major modes of the spindle. The mode at 3195 Hz arise because of material and geometry of the shaft of the spindle. The modes between 1500 Hz and 2000 Hz are related to the bearings. After the maintenance, magnitude of the mode at 3195 drops to $2.3\,x10^{-8}\,m$ from $3.0\,x10^{-8}\,m$ and frequency of the mode shifts to 3246 Hz. On the other hand, magnitude of peaks between 1500 Hz and 2000 Hz decrease drastically and markedness of these modes significantly diminish. During the maintenance all bearings are removed, and new ones are installed. Stages of the assembly can be seen in Figure 4.5. Details of new bearings are given in previous sections. After disassembly, surfaces of the shaft that bearings lie, are only grinded. Small change at the mode related to shaft and dramatic change at the modes related to bearings can be explained with this.

Figure 4.5 Bearing Assembly Stages of the Spindle

4.1.3 System Identification

Using the analytical model given in Chapter 2, stiffness values of bearings are calculated. These stiffnesses and other spindle parameters are used in the Finite

element model which is presented in Chapter 3 and as a result FRF of the system is obtained. Results are not aligned with the experiment results so a study aiming to find bearings stiffnesses that are aligned with the experiment results, is conducted. Same finite element model is used but stiffness values of springs are changed using trial-and-error method until the output of the model becomes compatible with the experiment. Stiffness values to obtain similar results to the experiment results, are presented in Table 11 and Table 12.

Table 11 Stiffness Values of Bearings Before Maintenance Calculated using The FEM and Trial-and-Error Method

	Bearing 1	**Bearing 2**	**Bearing 3**	**Bearing 4**
K_{yy} [N/m]	$2.1\ x10^8$	$2.1\ x10^8$	$2.4\ x10^8$	$2.4\ x10^8$
$K_{\theta x\theta x}$ [N.rad/m]	$1.0\ x10^5$	$1.0\ x10^5$	$1.0\ x10^5$	$1.0\ x10^5$

Table 12 Stiffness Values of Bearings After Maintenance Calculated using The FEM and Trial-and-Error Method

	Bearing 1	**Bearing 2**	**Bearing 3**	**Bearing 4**
K_{yy} [N/m]	$3.0\ x10^8$	$3.0\ x10^8$	$2.5\ x10^8$	$2.5\ x10^8$
$K_{\theta x\theta x}$ [N.rad/m]	$1.5\ x10^5$	$1.5\ x10^5$	$1.0\ x10^5$	$1.0\ x10^5$

Modal test is conducted only in the y direction so only stiffness values that can be measured at this direction are calculated and presented. The accelerometer is attached to measure in y direction and hammer is hit to the shaft in the same direction. So, with the conducted test, it is not possible to get information about every stiffness value at the stiffness matrix. The test only gives information about the stiffness in the y direction and the rotational stiffness coupled with the stiffness at y axis.

Stiffnesses calculated at zero defect condition using the analytical model at the chapter 2, corresponds to after maintenance values of the experimental results. The results calculated using bearing geometry and material are nearly half of values

calculated using experiment results. This inconsistency is because of assumption of rigid bearing-shaft connection. After calculating stiffness values using the analytical model, stiffness values are directly used for defining relation between housing and the shaft of the spindle. Relation between inner race of bearing and shaft, outer race of the bearing and housing are not considered. These connections can also be modeled as stiffness meaning that there will be 3 springs attached in serial at the finite element model. Serially attached spring will have a smaller equivalent stiffness compared to stiffnesses one by one. Since experiment result gives this equivalent stiffness between shaft and the housing, difference between values of model and experiment is comprehensible.

CHAPTER 5

SPINDLE FAULT DETECTION

Fault detection methods using vibration data can be done in different formats. Time-domain and frequency-domain analyses are the most frequently used ones and will be demonstrated in this section.

5.1 Time Domain Analysis

Time-domain indicates analysis of the data as a function of time. Time-domain analysis is conducted by using waveform indices. These indices are numbers calculated using vibration signal. They are used of comparison of data and understanding the trend. RMS, peak-to-peak and kurtosis are some of these indicators that are widely used.

RMS is one of the most popular time-waveform indicators. It considers time history of the data and also gives an amplitude value that is linked with energy content of the signal. In other words, it gives information about destructiveness of the vibration to the machine. There are standards that are used at the industry that defines RMS values for defining machine condition. These standards will be introduced in detail in oncoming sections.

Peak-to-peak amplitude is another commonly used indicator. It is defined as maximum positive to negative amplitude. RMS and peak-to-peak definitions on a sine wave and a random signal can be seen in Figure 5.1.

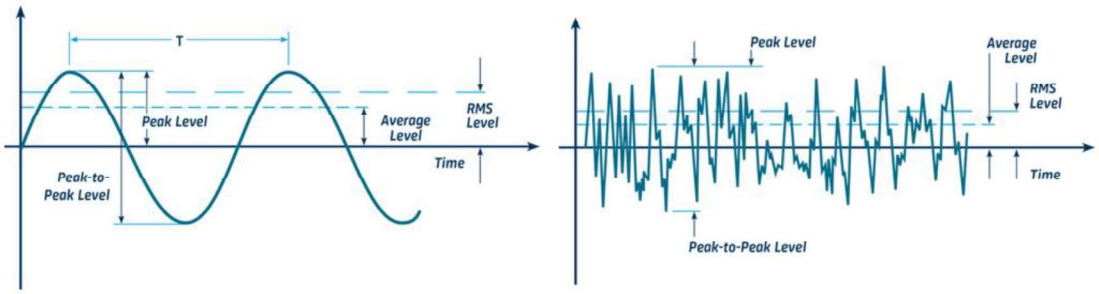

Figure 5.1 RMS and Peak-to-peak Definitions on a Sine Wave and a Random Signal [3]

Kurtosis is indicator of peakedness. It is sensitive to the impulsive content of the signal meaning it is sensitive to the vibrations at generated by localized bearing faults. Because of this critical property, kurtosis is widely used at fault detection especially at early stages [74]. On the other hand, it is not useful for tracking the condition since as condition of bearing gets worse vibration data becomes more random and impulsive nature of the signal disappears while noise increases. The kurtosis increased at early stages of fault, starts to decrease. The value of kurtosis of the vibration signal generated by bearings at good condition is three [75] [76].

5.1.1 Vibration Data Evaluation Standards for Detecting Fault

All the machines with rotating parts, work with a specific vibration signature. It is possible to determine condition of a machine with vibration data measured at working conditions. There are several standards that used in industry for detecting condition of machines. Since every kind of machine has different vibration signatures, there are different standards for different machine types. Note that, after getting enough data from a machine, generating an evaluating chart specific for the machine is more favorable. Standards are generally better for getting an insight before the evaluation.

Vibration of a rotating machine can be measured basically from two different points: on rotating parts and on non-rotating parts. ISO 7919 and ISO 10816 are standards according to measuring location of vibration data. ISO 7919 defines requirements

and criteria based on measurements made on the rotating shaft and ISO 10816 is for measurements made on non-rotating parts.

ISO 10816 is comprised of six parts which is are specialized for different kind of rotating machines. Part 3 is suitable for spindles operating up to 15000 rpm. ISO 10816 separates machines into 4 groups considering machine type, shaft length or rated power. The standard classifies machines mounting to its environment into two: flexible and rigid. The condition of the machine is also divided into 4 zones. Zone A and B are good, Zone C is unsatisfactory, but maintenance is not urgent, and Zone D means urgent maintenance is necessary. Displacement RMS and velocity RMS of the vibration data taken form the machine is evaluated using these zones. Zone boundaries differ according to the classification of the machine. One of classification tables can be seen in Figure 5.2. This table is for medium size machines with rated power above 15 kW up to 300 kW [77].

Support class	Zone boundary	R.m.s. displacement μm	R.m.s. velocity mm/s
Rigid	A/B	22	1,4
	B/C	45	2,8
	C/D	71	4,5
Flexible	A/B	37	2,3
	B/C	71	4,5
	C/D	113	7,1

Figure 5.2 Evaluation Table from ISO 10816 (Table A.2) [77]

There are also specialized standards for machines. ISO 17243 is a standard for evaluating vibrations of machine tool spindles by measuring vibration data on non-rotating parts. ISO 17243 also has different parts separated according to drive type of the spindle. This standard uses acceleration RMS and velocity RMS for evaluating vibrations considering operating rotational speed of the spindle. An evaluation table from ISO 17243 can be seen in Figure 5.3.

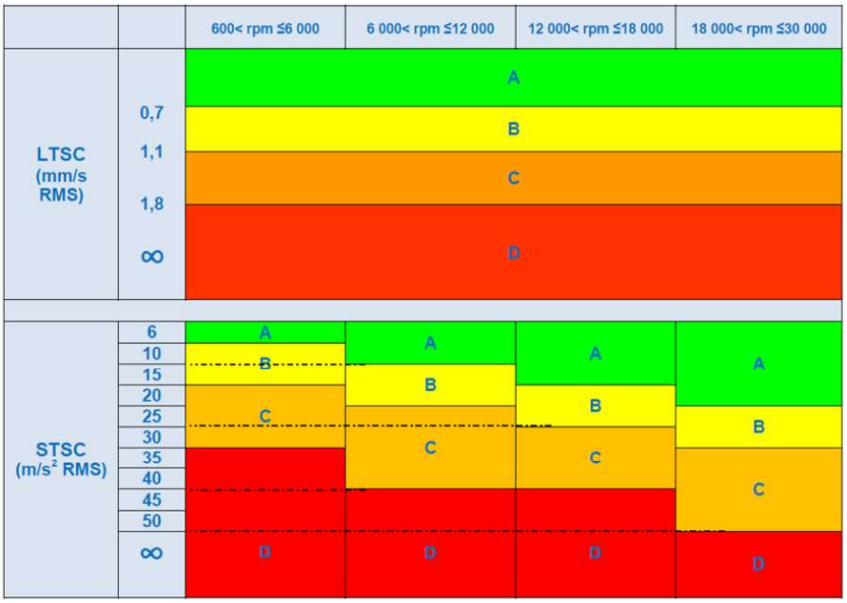

Figure 5.3 Evaluation Table from IS0 17243 [78]

5.1.2 Data Acquisition for Fault Detection at Operating Conditions

The vibration data which will be used for fault detection of the spindle, is collected with the data acquisition system in Figure 5.4. Getac computer and Siemens LMS SCADAS recorder is used for data acquisition and recording. As sensors PCB 352A24 accelerometers are used.

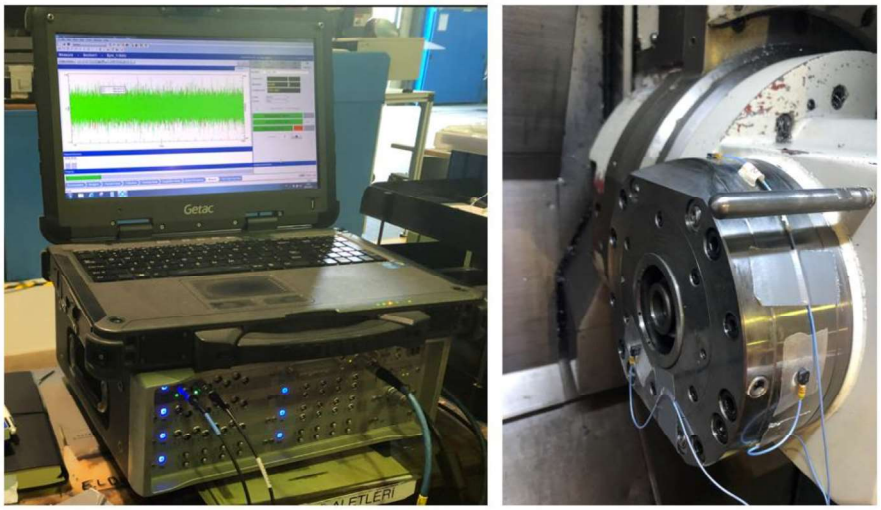

Figure 5.4 Vibration Data Acquisition System

Vibration data is collected from spindle at different rotational speed. While data is collected, holder and tool are not clamped to the spindle. The data is collected at steady state working conditions.

5.1.3 Evaluation of Vibration Data with Time-Domain Approach

Using vibration data collected from spindles while spindles are operating at different rotational speeds, condition of the spindles is determined. Five spindles are analyzed.

5.1.3.1 Spindle 1

The vibration data is taken after a maintenance while the spindle is working without a problem. The vibration data is taken from the spindle at two rotational speeds. RMS, kurtosis, and peak-to-peak values are calculated from the collected data and given in Table 16.

Table 13 RMS, Kurtosis and Peak-to-peak values of Spindle 1 at Different Rotational Speeds

Rotational speed of the Spindle (Hz)	**50**	**66,6**	**83,3**	**100,0**	**133,3**	**166,7**
Displacement Overall RMS (mm)	0,014	0,026	0,013	0,013	0,024	0,019
Velocity Overall RMS (mm/s)	0,329	0,343	0,276	0,244	0,516	0,587
Acceleration Overall GRMS	0,126	0,14	0,154	0,167	0,329	0,282
Kurtosis	2,81	2,91	3,01	3,00	2,26	2,70
Peak-to-Peak (g)	0,97	1,10	1,24	1,51	2,25	2,28

RMS values are in Zone A according to tables given in previous sections, indicating that the spindle is newly commissioned. Kurtosis values are three or lower than three. Peak-to-peak magnitude is low. All the indicators point that the spindle is at good condition.

5.1.3.2 Spindle 2

Acceleration data is collected from the spindle at three different rotational speeds. RMS values for acceleration, velocity, and displacement and Kurtosis and Peak-to-peak values at these rotational speeds, are given in Table 14.

Table 14 RMS, Kurtosis and Peak-to-peak values of Spindle 2 at Different Rotational Speeds

Rotational speed of the Spindle (Hz)	**133,3**	**166,7**	**200,0**
Displacement Overall RMS (mm)	0,0271	0,0537	0,062
Velocity Overall RMS (mm/s)	0,806	2,56	2,3
Acceleration Overall GRMS	0,645	0,607	1,19
Kurtosis	2,99	2,90	4,01
Peak-to-Peak (g)	5,45	4,59	13,12

Comparing values given in Table 14 with standards given in previous sections. Displacement RMS values at 200 Hz lie in the Zone C and velocity RMS of the same rotational speed is in Zone D. Kurtosis values of 133 Hz and 166 Hz are normal but kurtosis of 200 Hz indicates there is a fault at the bearings. Peak-to-peak values are high compared to good-conditioned spindle.

5.1.3.3 Spindle 3

Acceleration data is collected at 4000 rpm, 8000 rpm and 12000 rpm. RMS, Kurtosis and Peak-to-peak values of the data can be seen in Table 15.

Table 15 RMS, Kurtosis and Peak-to-peak values of Spindle 3 at Different Rotational Speeds

Rotational speed of the Spindle (Hz)	**66,7**	**133,3**	**200,0**
Displacement Overall RMS (mm)	0,0123	0,0344	0,053
Velocity Overall RMS (mm/s)	0,0298	1,25	0,782
Acceleration Overall GRMS	0,756	1,73	1,70
Kurtosis	3,06	3,04	2,75
Peak-to-Peak (g)	6,20	14,16	12,11

Acceleration RMS values are at Zone B and displacement RMS of 200 Hz spindle is at Zone C. 200 Hz velocity RMS of the spindle lie in the Zone C. Kurtosis values are in the limits, but peak-to-peak values are 8-9 times larger good-conditioned spindle.

5.1.3.4 Spindle 4

Vibration data collected at two different rotational speed which are 3000 rpm and 5000 rpm, are analyzed. Displacement RMS, velocity RMS and acceleration RMS, Kurtosis and Peak-to-peak values are given in Table 16.

Table 16 RMS, Kurtosis and Peak-to-peak values of Spindle 4 at Different Rotational Speeds

Rotational speed of the Spindle (Hz)	**50,00**	**83,33**
Displacement Overall RMS (mm)	0,0458	0,0647
Velocity Overall RMS (mm/s)	0,395	0,542
Acceleration Overall GRMS	1,52	2,55
Kurtosis	3,26	3,23
Peak-to-Peak (g)	16,76	27,97

Acceleration RMS Value taken from 83 Hz (5000 rpm) are in Zone C meaning condition of the spindle is unsatisfactory and spindle can operate for a period until maintenance. Kurtosis values are not out of charts but above the limits. Peak-to-peak values are arrestingly large.

5.1.3.5 Spindle 5

Acceleration data is collected at 6000 rpm, 8000 rpm and 12000 rpm. RMS, Kurtosis and Peak-to-peak values of the data can be seen in Table 17.

Table 17 RMS, Kurtosis and Peak-to-peak values of Spindle 5 at Different Rotational Speeds

Rotational speed of the Spindle (Hz)	**100**	**133,33**	**200**
Displacement Overall RMS (mm)	0,006	0,004	0,0173
Velocity Overall RMS (mm/s)	0,541	0,666	1,4
Acceleration Overall GRMS	1,34	1,01	1,27
Kurtosis	2,79	2,89	2,98
Peak-to-Peak (g)	10,7	8,58	9,49

As seen from Table 17, GRMS values of 100 Hz and 200 Hz lays in the Zone B while velocity RMS of 200 Hz lays in the zone C. This indicates there is nothing urgent, but a maintenance need to be planned it the near future. Kurtosis values do not indicate any fault, but peak-to-peak values are significantly large compared to good-conditioned spindle.

5.2 Frequency Domain Analysis

5.2.1 Bearing Defect Frequencies

Every time a local defect on an element engages with its opposing element, sudden changes occur at the contact stresses that creates a pulse with low duration. This pulse generates vibration and noise which can be detected by sensors. Even a bearing in good condition generate vibration, but the presence of defects dramatically increases vibration levels [11].

Each bearing element (inner race, outer race, cage, ball spinning etc.) has its own characteristic. If there is a defect at a particular bearing element, vibration energy associated with the frequency increases. These characteristic defect frequencies can be calculated using kinematic considerations: rotational speed and geometry of the bearing [79].

Cutaway view of a bearing and a ball of a bearing can be seen at Figure 5.5

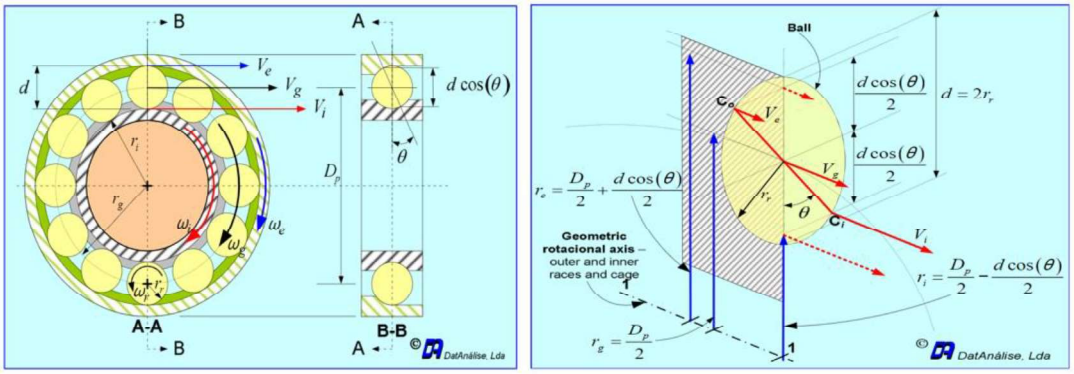

Figure 5.5 Bearing Geometry - Section View [80]

Angular speeds of the cage, outer race and inner race are:

$$\omega_g = \frac{V_g}{r_g} \tag{5.1}$$

$$\omega_e = \frac{V_e}{r_e} \tag{5.2}$$

$$\omega_i = \frac{V_i}{r_i} \tag{5.3}$$

Assuming there is no sliding, cage linear speed is:

$$V_g = \frac{V_i + V_e}{2} = \frac{\omega_i r_i + \omega_e r_e}{2} \tag{5.4}$$

From Figure 5.5, following can be written,

$$r_g = \frac{D_p}{2} \tag{5.5}$$

$$r_i = \frac{D_p}{2} - \frac{d\cos(\Theta)}{2} \tag{5.6}$$

$$r_e = \frac{D_p}{2} + \frac{d\cos(\Theta)}{2} \tag{5.7}$$

$$r_r = \frac{d}{2} \tag{5.8}$$

Putting all the results together, angular speed of cage is:

$$\omega_g = \frac{1}{2}\left[\omega_i\left(1 - \frac{d\cos(\Theta)}{D_p}\right) + \omega_e\left(1 + \frac{d\cos(\Theta)}{D_p}\right)\right] \tag{5.9}$$

Being $\omega_g = 2\pi f_g$, equation can be written in [Hz] as follows,

$$f_g = FTF = \frac{1}{2}\left[f_i\left(1 - \frac{d\cos(\Theta)}{D_p}\right) + f_e\left(1 + \frac{d\cos(\Theta)}{D_p}\right)\right] \tag{5.10}$$

Ball passing frequency of the outer race can be expressed as,

$$BPFO = N(\omega_g - \omega_e) \tag{5.11}$$

$$BPFO = N\left\{\frac{1}{2}\left[f_i\left(1 - \frac{d\cos(\Theta)}{D_p}\right) + f_e\left(1 + \frac{d\cos(\Theta)}{D_p}\right)\right] - f_e\right\} \tag{5.12}$$

With mathematical manipulation expression can be written as,

$$BPFO = \frac{N}{2}(f_i - f_e)\left(1 - \frac{d\cos(\Theta)}{D_p}\right) \tag{5.13}$$

Ball passing frequency of inner race can be calculated by multiplying number of balls with difference of angular speeds of inner race and cage as,

$$BPFI = N(\omega_i - \omega_g) \tag{5.14}$$

$$BPFI = \frac{N}{2}(f_i - f_e)\left(1 + \frac{dcos(\Theta)}{D_p}\right) \tag{5.15}$$

Balls spin frequency can be defined as,

$$\omega_r = \frac{V_r}{r_r} \tag{5.16}$$

Assuming only pure rotation exists and there is no sliding, the tangential speed of the ball and inner race at the contact point can be expressed as,

$$V_r = (\omega_i - \omega_g)r_i \tag{5.17}$$

$$\omega_r = \frac{(\omega_i - \omega_g)r_i}{r_r} \tag{5.18}$$

Putting equations together ball spin frequency can be written as,

$$BSF = f_r = \frac{D_p}{2d}(f_i - f_e)\left(1 - \left(\frac{dcos(\Theta)}{D_p}\right)^2\right) \tag{5.19}$$

When outer race of the bearing is considered stationary, defect frequencies can be written as follows,

$$FTF = \frac{1}{2}\left[f_i\left(1 - \frac{dcos(\Theta)}{D_p}\right)\right] \tag{5.20}$$

$$BPFO = \frac{N}{2}\left[f_i\left(1 - \frac{dcos(\Theta)}{D_p}\right)\right] \tag{5.21}$$

$$BPFI = \frac{N}{2}\left[f_i\left(1 + \frac{dcos(\Theta)}{D_p}\right)\right] \tag{5.22}$$

$$BSF = \frac{D_p}{2d}(f_i)\left(1 - \left(\frac{dcos(\Theta)}{D_p}\right)^2\right) \tag{5.23}$$

where f_i is the shaft rotation frequency in rad/s, D_p is the bearing pitch diameter, d is the rolling element diameter, N is number of rolling elements, θ is the contact angle.

These equations are valid under pure rotation condition. Sliding motion can occur which causes minor shift of bearing defect frequencies. For this reason, these formulations should be used as approximations.

If the number of known parameters are not enough for using mathematical model, empirical model can also be used. The following equations compute approximate values for frequencies transmitted from faulty bearing. [80].

$$FTF = 0.4 f_i \tag{5.24}$$

$$BPFO = 0.4 N f_i \tag{5.25}$$

$$BPFI = 0.6 N f_i \tag{5.26}$$

5.2.2 Shaft Faults

Frequency spectrum gives information about different component frequencies. By identifying and tracking specific frequencies, faults at the shaft of the spindle can be recognized before failure occurs. Monitoring magnitude of identified frequencies under same operating conditions can give information about severity of the fault. Most common faults that occur at the shaft of the spindle are misalignment, unbalance, and mechanical looseness.

5.2.2.1 Misalignment

Misalignment happens when centerlines of couplings, bearings or shaft are not along with each other. Misalignment can be angular, parallel or both. Some of typical reasons of misalignment:

- improper installation of spindle

- irregular foundation, offsetting of foundation

- changing dimensions due to cooling or heating of the components, can happen sometime after installation

Misalignment itself decreases spindle precision and most of the time causes bearing to carry more load than design criteria. So, it causes early bearing failures because of fatigue. [81]

Misalignment can be detected by looking ratio of magnitudes between 1x and 2x of the rotational speed of the spindle. If magnitudes of 2x of the rotational speed at the spectrum is less than 50% of 1x of the rotational speed, this spindle will operate without problem for long time. If this ratio is larger the 150%, the spindle should be repaired at the first possible time.[81]. If ratio is in between these percentages spindle should be monitored frequently.

5.2.2.2 Unbalance

Unbalance take place when the shafts geometric and mass centerlines do not coincide with each other. Unbalance is one of the common faults that occur at the spindle. Unbalance can be static, coupled or both (dynamic). Main reasons of the unbalance are irregular machining of components and improper balancing operation .

Pure unbalance is at sinusoidal waveform happening once at every rotation. By looking at the FFT spectrum it comes out as more than normal amplitude of 1x of the rotational speed of the spindle . Most of the time amplitude of unbalance increases with increasing rotational speed. Spectrum generally does not involve harmonics of the unbalance. If magnitude of the harmonics of the 1x of the rotational speed is less than 15% , there is probably unbalance.

Unbalance cause nearby bearings to carry more load than expected so , like misalignment , decreases lifespan of the bearings.

5.2.2.3 Mechanical Looseness

Spindle getting loose from its mounting , damaged mounting or a component of a spindle getting loose can cause mechanical looseness. For instance, an over clearance at the mounting of a bearing can cause mechanical looseness. If looseness is caused form a component of the spindle, most of the time it causes a secondary damage.

Mechanical looseness appear at the FFT at harmonics and ½ harmonics of the rotational speed of the spindle. if magnitudes of the harmonics which can be unorganized and random, are more than 20% of the 1x of the rotational speed of the spindle, it can be said that there is a mechanical looseness or inappropriate fit between component.

5.2.3 Evaluation of Vibration Data with Frequency-Domain Approach

Same five spindles evaluated using time-domain methods will be analyzed using frequency-domain methods.

5.2.3.1 Spindle 1

Bearing dimensions that needed to calculate bearing defect frequencies are given in Table 18 and bearing defect frequencies calculated using the and rotational speeds is given in Table 19.

Table 18 Bearing Dimensions of Spindle 1

Pitch diameter (mm)	Ball diameter (mm)	Number of balls	Contact Angle
102,5	11,7	18	18

Table 19 Bearing Defect Frequencies of Spindle 1

Rotational speed of the Spindle (Hz)	**100,0**	**166,7**
Outer race defect frequency (Hz)	801,0	1334,9
Inner race defect frequency (Hz)	999,0	1664,9
Ball defect Frequency (Hz)	432,0	720,0
Cage defect frequency (Hz)	44,0	73,3

FRF of the vibration data taken from spindles at 6000 rpm and 10000 rpm rotational speeds can be seen in Figure 5.6 and Figure 5.7, respectively.

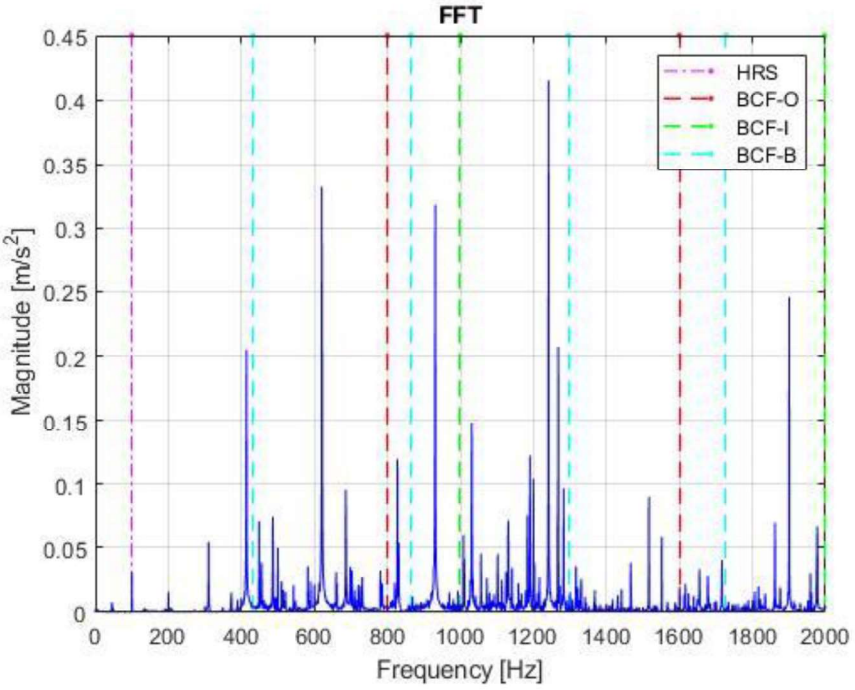

Figure 5.6 FFT of Spindle 1 Rotating at 100 Hz

As seen from Figure 5.6, none of bearing defect frequencies are distinguishable. There is no sign of unbalance, misalignment, or mechanical looseness. Magnitude levels of FRF is relatively low compared to the previous cases. Low RMS and peak-to-peak values have already indicated this outcome.

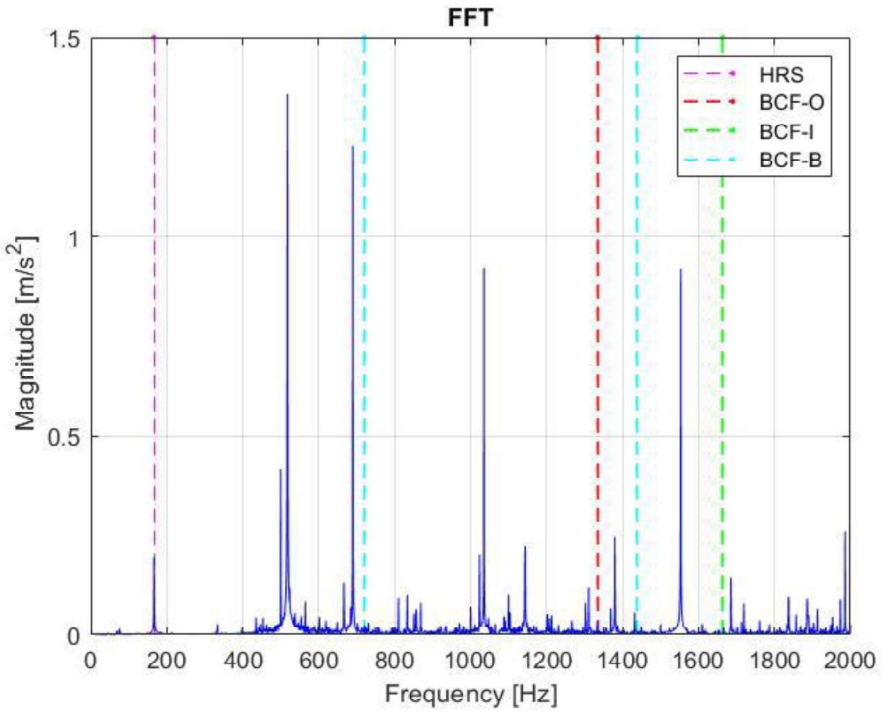

Figure 5.7 FFT of Spindle 1 Rotating at 166,7 Hz

Even dough magnitudes at the FRF are comparable with other spindles, this only by itself does not mean that the bearing is defected. But none of bearing defect frequencies can be detected from the FRF. Shaft faults occurring at the low frequencies are not visible. Frequency domain analysis cannot detect a fault. In the previous section, time domain analysis alco could not detect a defect. So, the spindle is in good condition.

5.2.3.2 Spindle 2

Bearing dimensions that are needed to calculate the bearing defect frequencies are given in Table 20. Bearing defect frequencies calculated using these dimensions at different rotational speeds in given in Table 21.

Table 20 Bearing Dimensions of Spindle 2

Pitch diameter (mm)	Ball diameter (mm)	Number of balls	Contact Angle
85	7,8	22	18

Table 21 Bearing Defect Frequencies of Spindle 2

Rotational speed of the Spindle (Hz)	**133,3**	**166,7**	**200,0**
Outer race defect frequency (Hz)	1338,6	1673,4	2008,0
Inner race defect frequency (Hz)	1594,6	1993,4	2392,0
Ball defect Frequency (Hz)	720,0	900,0	1080,0
Cage defect frequency (Hz)	60,0	75,0	90,0

FFT calculated using vibration data taken from spindle 2 at 8000 rpm, 10000 rpm and 12000 rpm are given in Figure 5.8, Figure 5.9 and Figure 5.11, respectively.

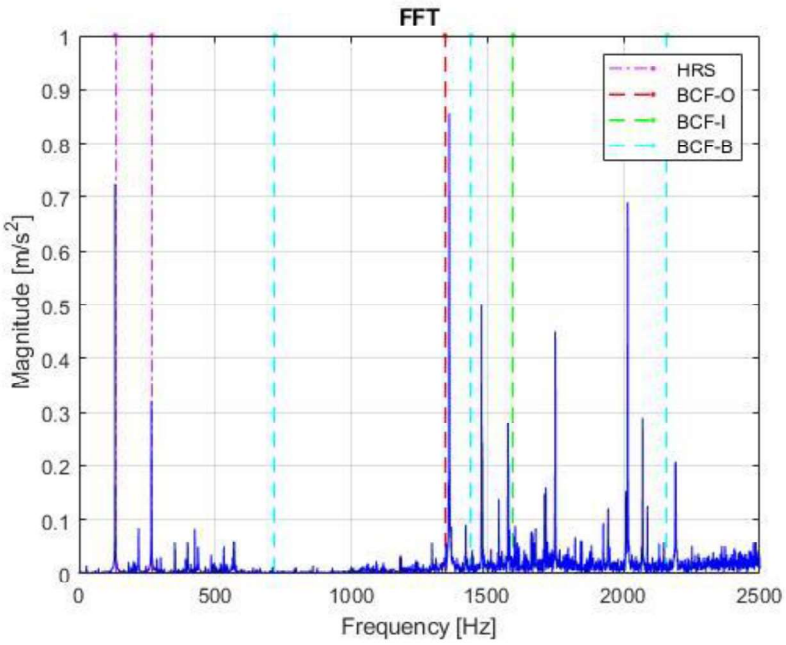

Figure 5.8 FFT of Spindle-2 Rotating at 133,3 Hz

As seen from Figure 5.8, there is a peak at the 1359 Hz which is close to bearing defect frequency calculated at this rotational speed.

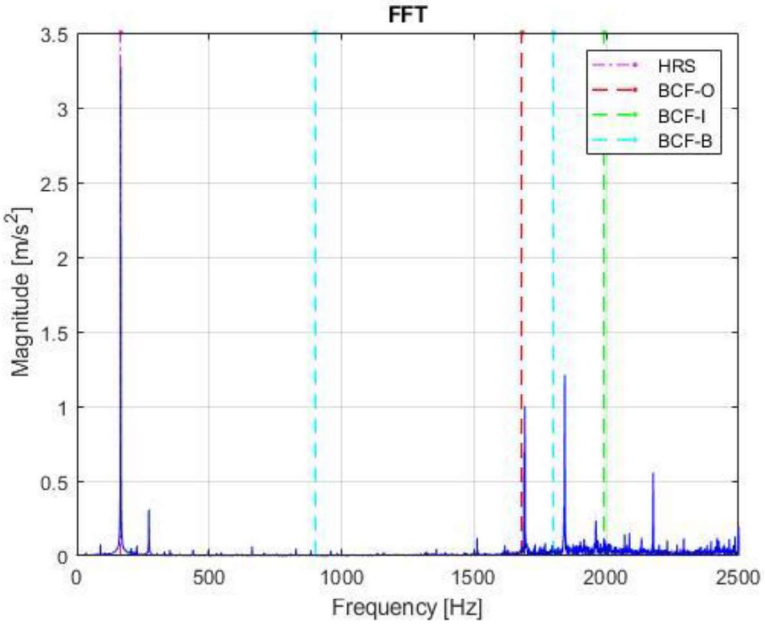

Figure 5.9 FFT of Spindle-2 Rotating at 166,7 Hz

As seen from Figure 5.9 there is a sharp increase at the FFT at the outer race defect frequency. Value is not directly same because of assumptions made while calculating bearing defect frequencies. The main assumption is no slippage. Slippage of surfaces directly changes defect frequencies. Magnitude of the 1x of the rotational speed is large and there are no harmonics of the rotational speed. This is an indication of unbalance at the shaft. For better interpretation, FFT of velocity should be investigated. FFT of velocity data can be seen in Figure 5.10

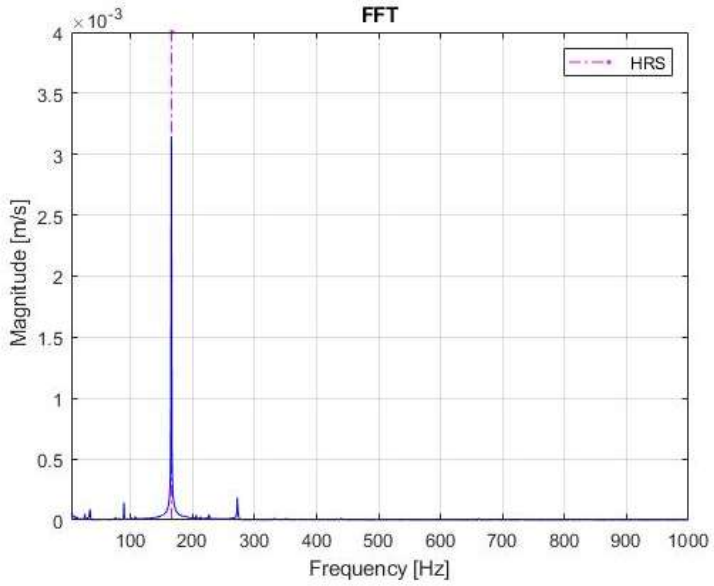

Figure 5.10 FFT obtained from Velocity Data of Spindle-2 Rotating at 166,7 Hz

As seen from Figure 5.10, there magnitude of the FFT at the rotational speed is significantly larger than magnitudes at other frequencies. This shows unbalance at the shaft of the spindle.

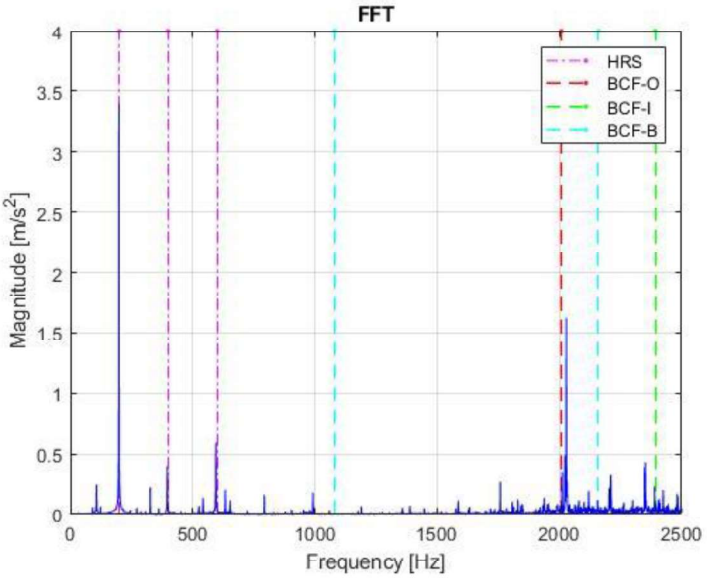

Figure 5.11 FFT of Spindle-2 Rotating at 200 Hz

As seen from Figure 5.11, the frequency corresponding outer race defect frequency is again large. This shows that there is a localized defect at the outer race at bearing of the spindle. 1x harmonic of the rotational speed is very large compared to its other harmonics. If second harmonic of the rotational speed is less than 15% of the first, this indicates unbalance at the shaft. To investigate unbalance, FFT obtained from velocity should be analyzed. FFT obtained from FFT at 12000 rpm can be seen in Figure 5.12.

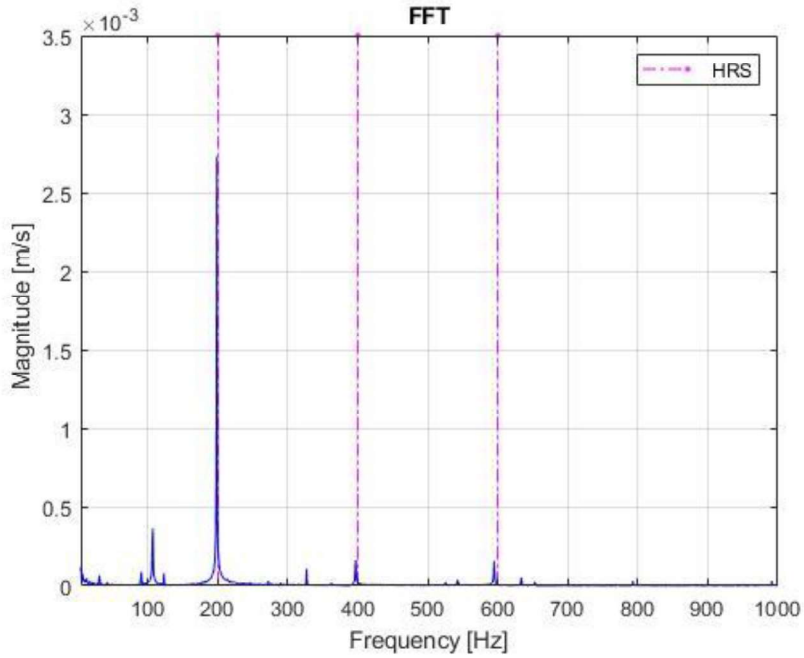

Figure 5.12 FFT Obtained from Velocity Data of Spindle-2 Rotating at 200 Hz

As seen from Figure 5.12, magnitude at the 1x of the rotational speed is incomparably large, meaning there is an unbalance at the shaft of the spindle.

Considering the FFT's, it can be concluded that spindle 2 has an outer race defect at the bearing and unbalance at the shaft. Time domain metrics indicate a fault at the spindle. When time domain metrics of spindle 2 are compared with the good, conditioned spindle, at the same frequencies, is can be seen that RMS values of good conditioned are smaller than spindle 2. Biggest difference at RMS values are at velocity RMS. RMS of velocity gives information about low frequency faults. After

frequency domain analysis, it is known that there is an unbalance at the shaft of the spindle, and this explains the significant difference of velocity RMS values. Kurtosis, acceleration RMS and peak-to-peak metrics suddenly increases at 200 Hz. This shows that peakedness and energy content of the signal is increased at 200 Hz.

5.2.3.3 Spindle 3

Bearing dimensions can be seen in Table 22. Bearing defect frequencies calculated using bearing dimensions at different rotational speeds is given in Table 23.

Table 22 Bearing Dimensions of Spindle 3

Pitch diameter (mm)	Ball diameter (mm)	Number of balls	Contact Angle
77,5	7,94	25	25

Table 23 Bearing Defect Frequencies of Spindle 3

Rotational speed of the Spindle (Hz)	**66,7**	**133,3**	**200,0**
Outer race defect frequency (Hz)	755,3	1510,6	2266,0
Inner race defect frequency (Hz)	910,6	1821,3	2732,0
Ball defect Frequency (Hz)	322,0	644,0	966,0
Cage defect frequency (Hz)	30,0	60,0	90,0

FFT of acceleration data collected at 4000 rpm, 8000 rpm and 12000 rpm can be seen in Figure 5.13, Figure 5.14 and Figure 5.15, respectively.

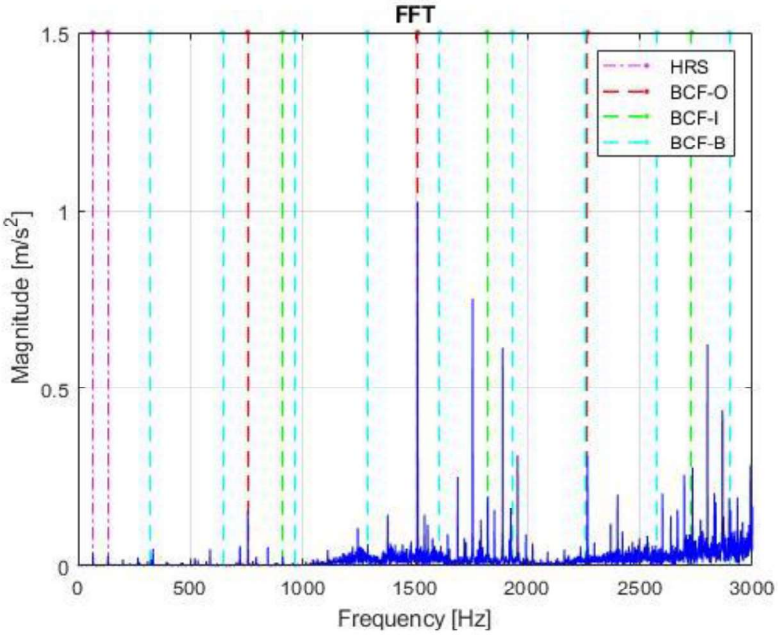

Figure 5.13 FFT of Spindle-3 Rotating at 66,7 Hz

As seen in Figure 5.13, there is an increase at the magnitude of the FFT at the outer race defect and its second and third harmonic.

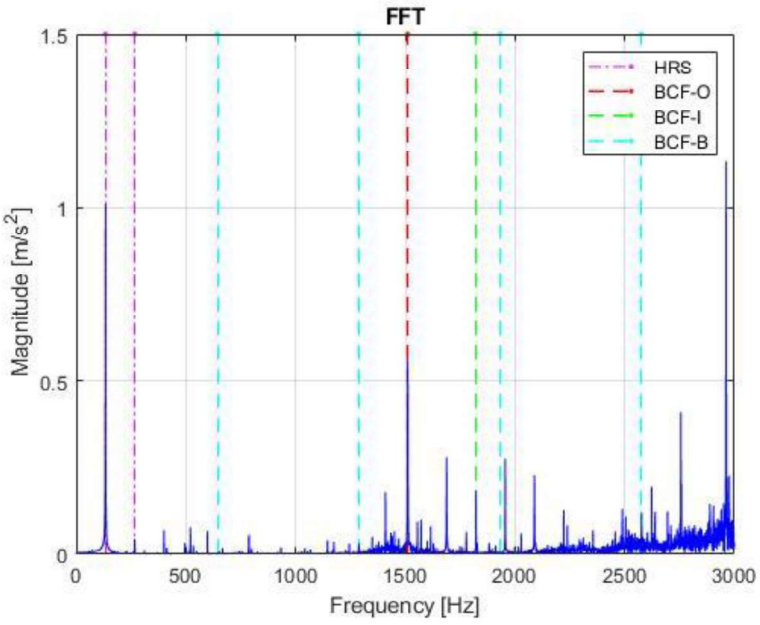

Figure 5.14 FFT of Spindle-3 Rotating at 133,3 Hz

Outer race defect frequency is again distinguishable among other frequencies. Note that, magnitude of the 1x harmonic of the rotational speed is large compared to its harmonics. This normally indicates that there is an unbalance at the shaft of the spindle but FFT's calculated at other rotational speeds does not support this.

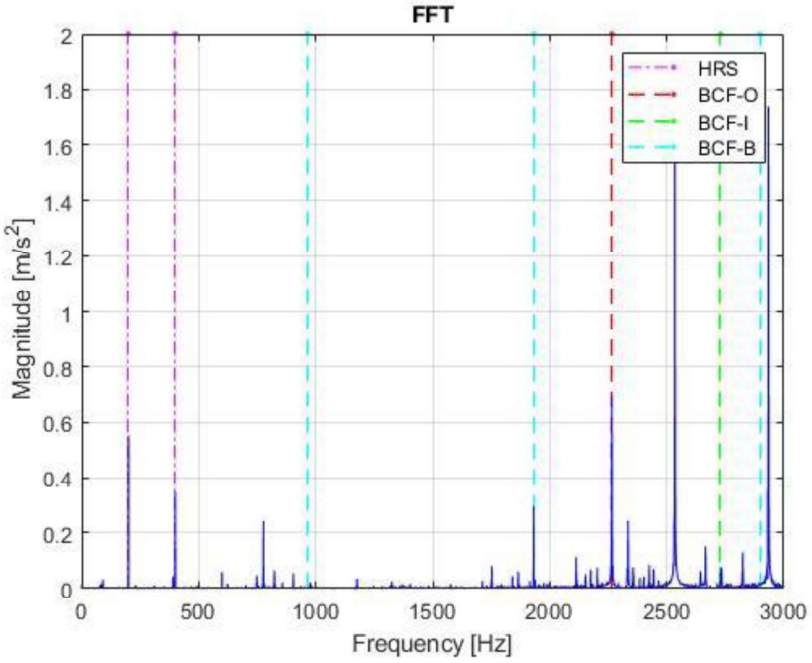

Figure 5.15 FFT of Spindle-3 Rotating at 200 Hz

As seen in Figure 5.15, outer race defect frequency calculated for 200 Hz rotational speed of the spindle is present at the FFT. Seeing outer race defect frequency at every FFT shows that there is a localized defect at the outer race. Time domain indicators are also shows that the spindle has a defect. 133 Hz velocity RMS is absurdly high. The reason of this can also be seen in FFT graph of the spindle 3 at 133 Hz. Magnitude of first harmonic of the rotational speed is large compared to rest of the graph. This magnitude difference at the 133 Hz graph can nor be seen at the other FFT's as in velocity RMS of the same spindle.

5.2.3.4 Spindle 4

Bearing dimensions needed to calculate bearing defect frequencies are given Table 24. The bearing defect frequencies which are calculated for different rotational speeds using information in Table 24, are given in Table 25.

Table 24 Bearing Dimensions of Spindle 4

Pitch diameter (mm)	Ball diameter (mm)	Number of balls	Contact Angle
97,5	17,7	15	25

Table 25 Bearing Defect Frequencies of Spindle 4

Rotational speed of the Spindle (Hz)	**50,00**	**83,33**
Outer race defect frequency (Hz)	313,3	521,9
Inner race defect frequency (Hz)	436,7	727,5
Ball defect Frequency (Hz)	133,9	223,2
Cage defect frequency (Hz)	20,9	34,8

FFT of the vibration data collected at 3000 rpm and 5000 rpm rotational speeds can be seen in Figure 5.16 and Figure 5.17, respectively.

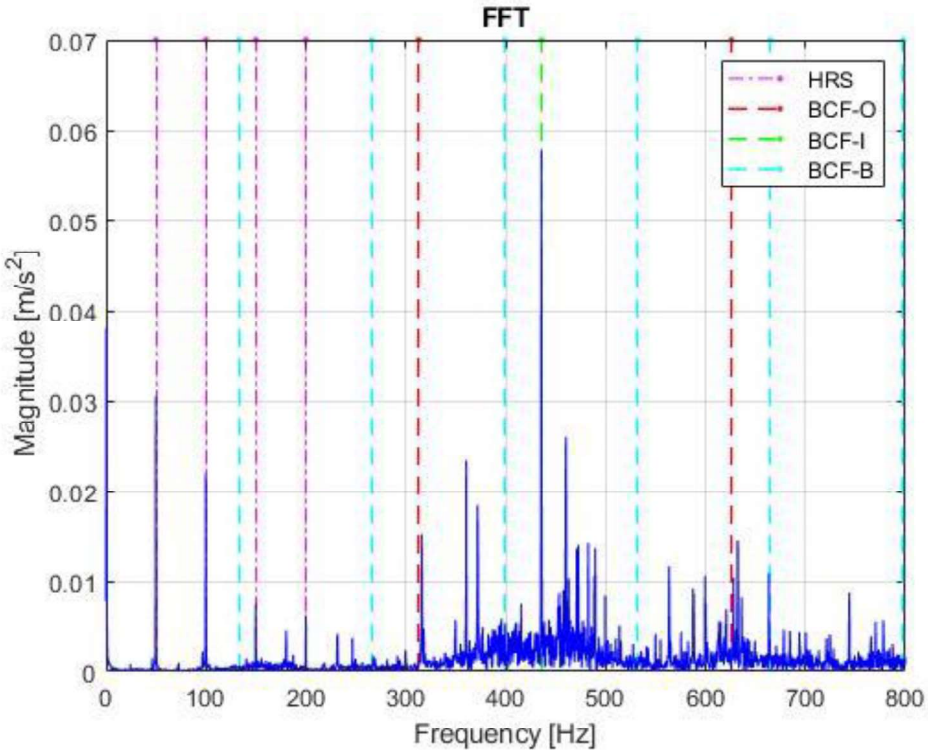

Figure 5.16 FFT of Spindle-4 Rotating at 50 Hz

As seen from Figure 5.16, FFT of the spindle running at 50 Hz contains inner and outer race bearing defect frequencies given in Table 25. Note that, magnitude of the FFT also increases at the rotational speed and its harmonics and increases at first harmonic of the outer race defect.

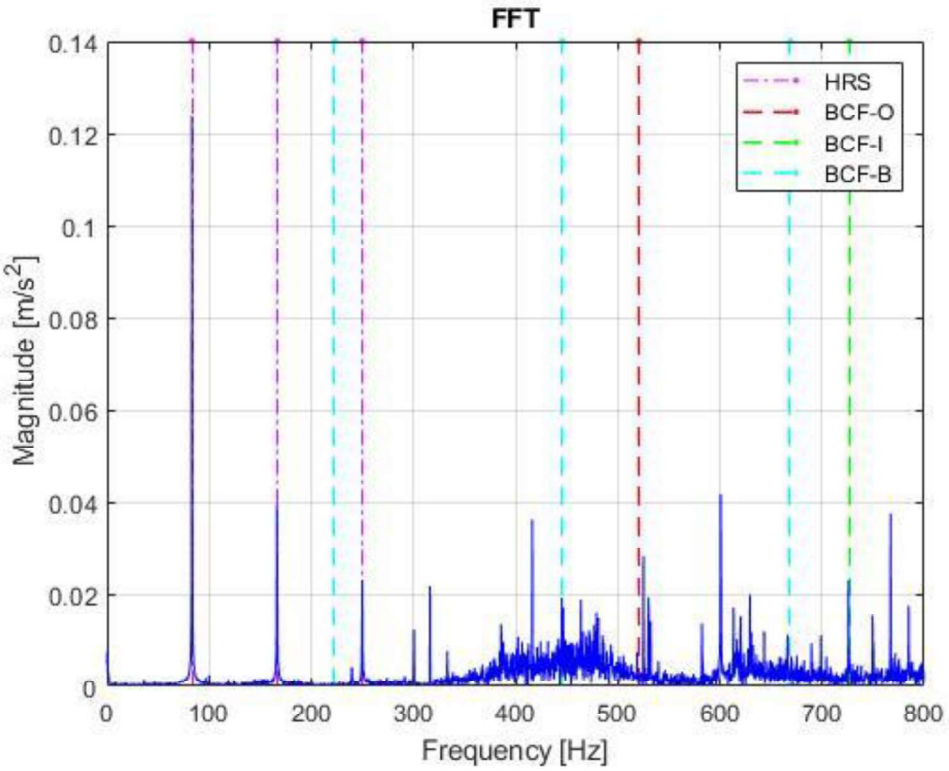

Figure 5.17 FFT of Spindle-4 Rotating at 83,3 Hz

As seen from Figure 5.17, FFT of spindle-1 running at 83,3 Hz contains inner and outer race defect frequencies given in Table 25. Frequencies are not directly equal but there are 3-4 Hz difference between calculations and FFT. This is because of slippage occurring while bearing rotate which is not considered while calculating bearing defect frequencies. Encountering bearing defect frequencies at two different rotational speeds means there are local defects at inner and outer race of the bearings between shaft and housing of the spindle.

In contrary to other data collected from other spindles, data of spindle 4 is collected while this spindle is still attached to the CNC machine. At other spindles, sensors are attached on the housing right on top of bearings and there are no joints that damp the vibrations. This is the reason of low amplitudes. Time domain metrics of spindle 4 is larger that spindle 1 but acceleration RMS is especially remarkable. Acceleration RMS shows energy level of the signal focusing on high frequencies. This spindle has bearing defects reasoning this drastic increase at the spindle.

5.2.3.5 Spindle 5

Bearing dimensions are given in Table 26 and bearing defect frequencies calculated using the and rotational speeds is given in Table 27.

Table 26 Bearing Dimensions of Spindle 5

Pitch diameter (mm)	Ball diameter (mm)	Number of balls	Contact Angle
85	7,8	22	18

Table 27 Bearing Defect Frequencies of Spindle 5

Rotational speed of the Spindle (Hz)	**100,0**	**133,33**	**200**
Outer race defect frequency (Hz)	1004,0	1338,6	2008,0
Inner race defect frequency (Hz)	1196,0	1594,6	2392,0
Ball defect Frequency (Hz)	540,0	720,0	1080,0
Cage defect frequency (Hz)	45,0	60,0	90,0

FRF of the vibration data taken from the spindle at 6000 rpm can be seen in Figure 5.18.

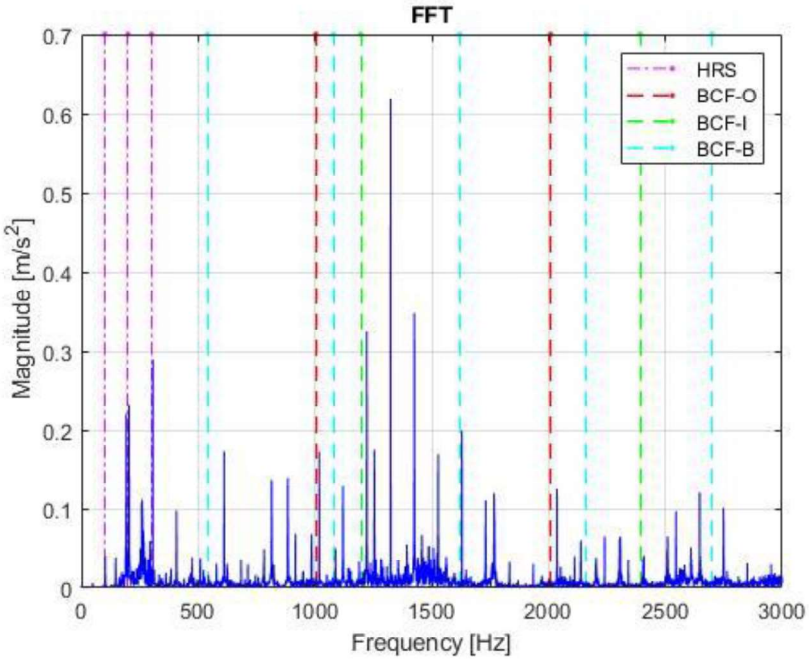

Figure 5.18 FFT of Spindle-5 Rotating at 100 Hz

As seen from Figure 5.18, bearing defect frequencies are not distinguishable at the plot. 2x, 2½x and 3x harmonics of rotational speeds magnitude are larger than the rotational speed harmonic. These point to the misalignment or mechanical looseness faults. To make better comments, FFT of velocity must be investigated. Velocity FFT of spindle 5 can be seen in Figure 5.19.

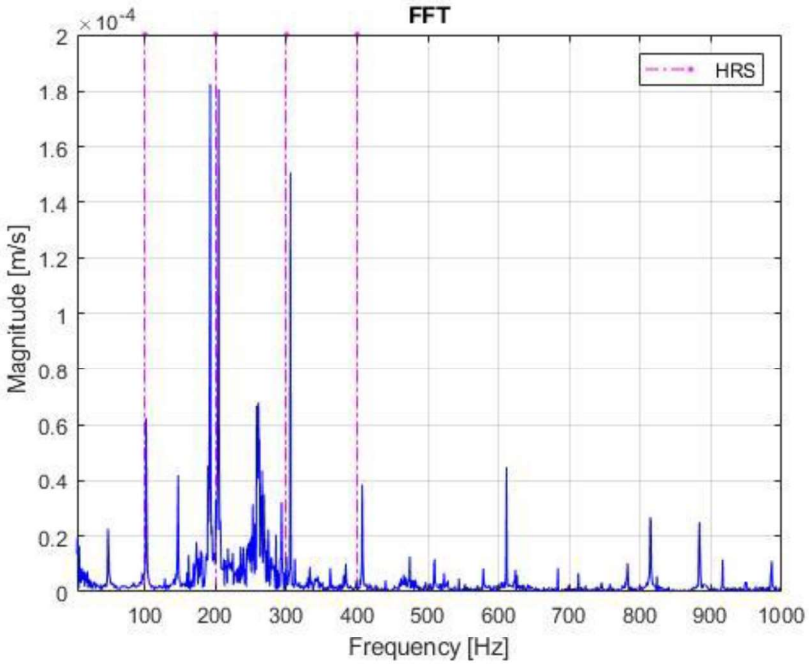

Figure 5.19 FFT Obtained from Velocity Data of Spindle-5 Rotating at 100 Hz

As seen from Figure 5.19, magnitude of 2x of the rotational speed is 2 times more than rotational speed. This indicates a misalignment fault at the spindle. Magnitudes ½x, 1½x, 2½ of the rotational speeds are also high compared to magnitude of 100 Hz, meaning that there is mechanical looseness.

FFT of the vibration data taken from the spindle at 8000 rpm can be seen in Figure 5.20.

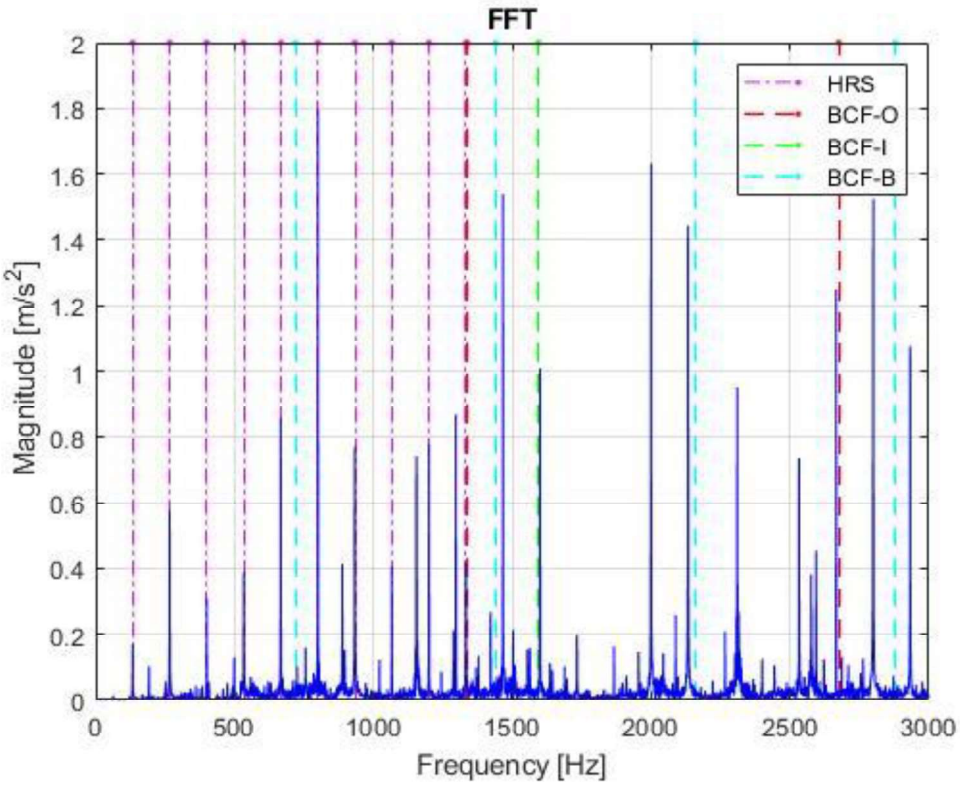

Figure 5.20 FFT of Spindle-5 Rotating at 133 Hz

Harmonics of rotational speed are eye catching. Magnitudes of them are more than magnitude of 1x of the rotational speed. This indicates mechanical looseness. FFT of velocity will be investigated for further information. Bearing defect frequencies are not stand out. FFT of vibration of velocity can be seen in Figure 5.21.

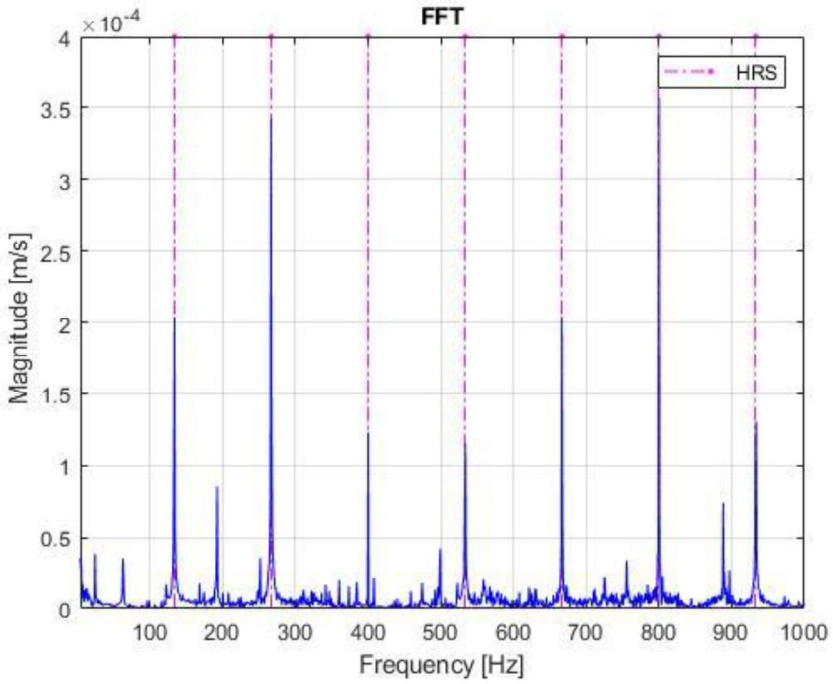

Figure 5.21 FFT Obtained from Velocity Data of Spindle-5 Rotating at 133 Hz

As seen from the Figure 5.21, 2x, 3x, 4x, 5x, 6x and 7x harmonics and 1½ harmonic of the rotational speed are noticeable. This FFT is a powerful indication of mechanical looseness. Magnitude of 2x harmonic of the rotational speed is again larger than magnitude of 1x harmonic so there can also be misalignment.

FFT of the vibration data taken from the spindle at 12000 rpm can be seen in Figure 5.22.

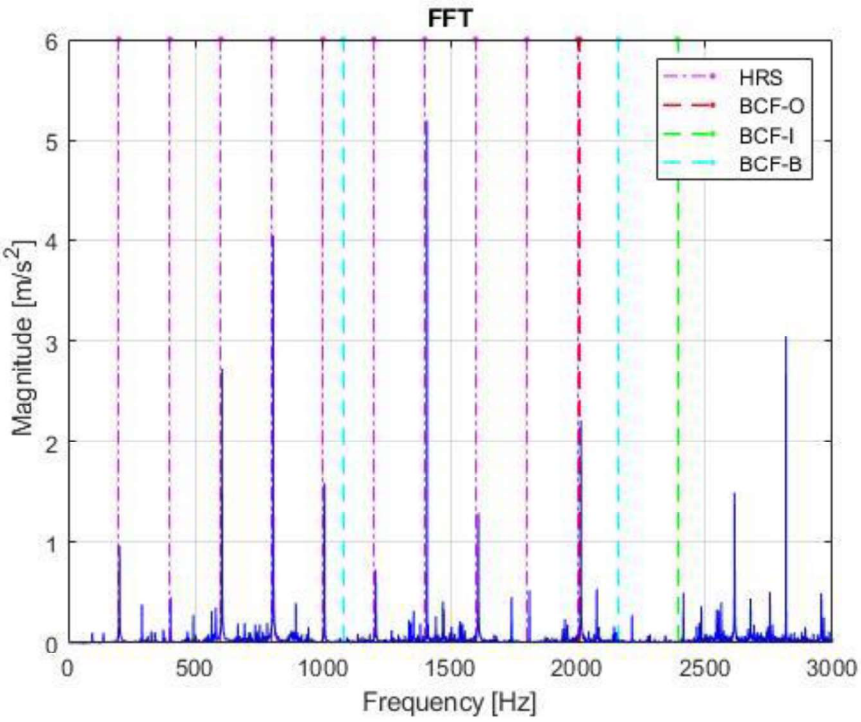

Figure 5.22 FFT of Spindle-5 Rotating at 200 Hz

As seen from Figure 5.22, outer race defect frequency can be detected at the FFT. At the other rotational speeds, this was not the case, so this do not indicate a defect at the outer race. Again, harmonics of the rotational speed are dominant so velocity FFT will be investigated. FFT of velocity vibration can be seen in Figure 5.22.

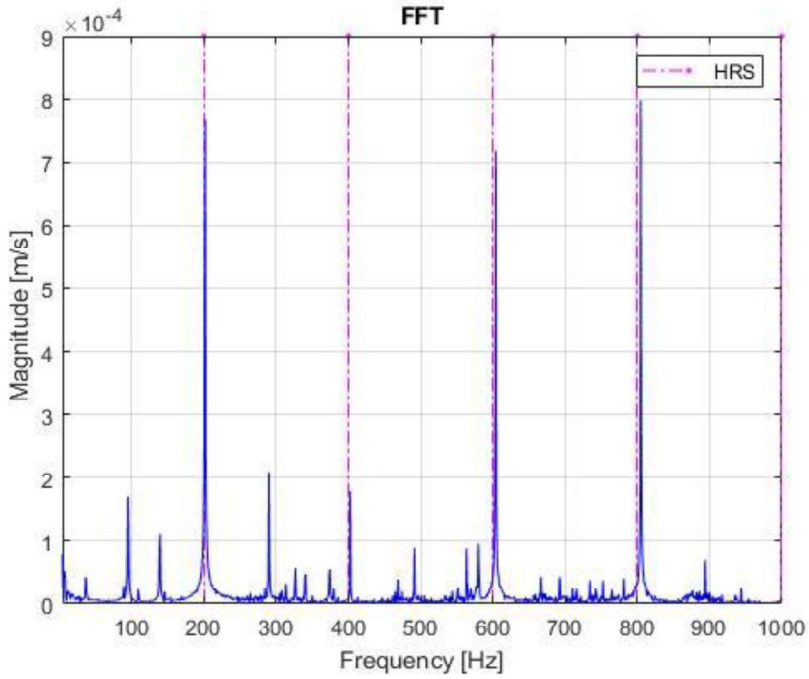

Figure 5.23 FFT Obtained from Velocity Data of Spindle-5 Rotating at 200 Hz

As seen from Figure 5.23, magnitude of ½x, 1½x, harmonics and 2x, 4x, 6x, 8x harmonics of the rotational speed are higher than a good-conditioned spindle compared to the magnitude of 1x of the rotational speed. This shows mechanical looseness fault and since all previous also indicate this faith, it can be concluded that spindle has mechanical looseness. In contrary to previous FFT's, magnitude of 2x harmonic of the rotational speed is not high so there is no misalignment fault at the shaft of the spindle.

FFT's of the spindle 5 indicated that there is mechanical looseness between components of the spindle. Time domain metrics also indicate that there are defects at the spindle. Acceleration and peak-to-peak values of the time-domain analysis are high compared to other metrics. This shows that there is a problem at the high frequency range. At the frequency domain analysis part, all type of the faults that may show itself at the high frequency range, are not shown. Some examples of these faults are waviness, surface roughness, uneven balls, misaligned races. Note that, most of bearing faults shows themselves at high frequencies.

CONCLUSION

6.1 Conclusions

In this thesis, effects of defects at bearings on spindles are studied and faults at the spindles are detected from the vibration data collected at operating condition. An analytical model that calculates stiffness values of bearing considering defects is created. Using these stiffnesses, a finite element model is generated and effect of bearings defects on tool point FRF of spindle is investigated. Results are compared with experiments. In addition, using vibration data gathered at operating conditions, faults at the spindle are detected.

A comprehensive literature review is conducted. Types and importance of maintenance and condition monitoring is explained. Criticality of spindle to CNC lathe and bearing to spindle system is interpreted. Varsal information about bearings, types of defects at bearings is give with explanatory visuals. Leading varying stiffness models in the literature are explained. Model that considers defects are further expounded. After that landmark spindle models on the literature are introduced. Some of them are given under the name of rotor-bearing systems. Bearing fault detection methods are presented under time domain and frequency domain approaches.

Varying stiffness model considering a defect at the outer race is generated. Hertz contact is introduced and applied to a ball bearing. Formulation needed to calculate stiffness of an angular contact ball bearing is demonstrated with all details. Using formulation given, an analytical model is generated and by comparing the outputs of the model with a well-excepted paper, the model is validated. After that, some of input parameters like defect depth and angle, preload and direction of the radial force are changed and graphs of stiffness versus these parameters are plotted. Effect of changes of these parameters to stiffness are discussed.

Finite element analysis of a spindle is conducted. Dimensions of the shaft and bearings of a Royal Spindle is measured, and solid model of the shaft is created. Effect of bearings on the shaft is modeled as springs. Stiffness values of bearings are calculated using analytical model presented in chapter 2, using dimensions and material properties as inputs to the model. Stiffness values of the bearing at different conditions are calculated. Using these results, different condition cases for the spindle are generated. Frequency response functions of these cases are compared and discussed. After that, a holder and two different tools are modeled and added to the spindle model. Point FTF at the tool tip is generated for two different tools at different conditions of the spindle.

Maintenance of a spindle is executed, and impact hammer test is conducted before and after the maintenance. Test setup is explained in detail and results are presented. A system identification study is conducted. Results of finite element model and experiment are compared. Outputs of FEM is found to be inconsistent with the experimental results and using trial-and-error method stiffness values for getting a convenient result from FEM is found. Assumptions of FEM are interrogated and reasons of inconsistency between finite model and experimental results are explained.

Fault detection for spindles is investigated using time-domain and frequency-domain methods. Popular time-domain methods used in the industry are introduced. Data acquisition system for fault detection is shown. Standards used in the industry are presented. Five spindles are analyzed at different rotational speeds, using given methods. In addition, bearing defect frequencies are introduced, assumptions and formulation is given. Common faults at shaft of the spindle and ways to detect them from the spectrum is explained. Same spindles analyzed using time domain results are again analyzed using frequency-domain methods. It is seen that, using only time domain methods or only frequency-domain methos is not enough for fault detection. They are powerful tools when used together. Time-domain methods are easy apply, but they do not give information about the type of fault at the spindle. Frequency-

domain methods are useful if what to search is known. They point the type of fault at the spindle.

6.2 Suggestions for Future Work

The analytical varying stiffness bearing model used in the study only considers outer race defects. Other types of localized defects can be added to the model like inner race defect, ball defect. A square shaped defect is assumed, and formulations are done accordingly. Actual shape of localized defects can be projected to the model. There are more parameters effecting the stiffness of bearings that are not investigated in the thesis but considered at the model. Effect of change of these parameters to the spindle can be studied.

Some parts of the spindle that vibrate with the shaft, like inner rings of the bearings and spacers and drawbar, are not considered at the finite element model. These parts can be added to the model. Three different bearing conditions are used to generate five different case studies to see the effect of change of bearing stiffness changes on spindle. Palette of conditions of bearings can be increased and number of cases can be increased accordingly.

Connections between inner race of the bearing and shaft, outer race of the bearing housing are assumed to be rigid. There connections could also be modelled in the FEM. By this way, results of finite element model and experiment would be in better harmony.

While performing the impact hammer test, number of sensors attached to the spindle can be increased. By this way system identification can be also done for other directions other than y axis. Housing of the spindle was not attached to the ground but was standing on the table with its own weight. Attaching the housing to the ground could increase reliability of the test.

FFT’s generated which are used for fault detection includes several peaks apart from fault frequencies. These peaks can be identified and can be eliminated if they do not indicate other type of faults.

REFERENCES

[1] R. Yan, R. X. Gao, and X. Chen, “Wavelets for fault diagnosis of rotary machines : A review with applications,” *Signal Processing*, vol. 96, pp. 1–15, 2014, doi: 10.1016/j.sigpro.2013.04.015.

[2] P. W. Tse and D. P. Atherton, “Prediction of machine deterioration using vibration based fault trends and recurrent neural networks,” *Journal of Vibration and Acoustics, Transactions of the ASME*, vol. 121, no. 3, pp. 355–362, 1999, doi: 10.1115/1.2893988.

[3] Brüel and Kjaer, “Using Vibration Measurements.”

[4] J. Lee, F. Wu, W. Zhao, M. Ghaffari, L. Liao, and D. Siegel, “Prognostics and health management design for rotary machinery systems - Reviews, methodology and applications,” *Mech Syst Signal Process*, vol. 42, no. 1–2, pp. 314–334, 2014, doi: 10.1016/j.ymssp.2013.06.004.

[5] L. Wang and A. Y. C. Nee, *Collaborative Design and Planning for Digital Manufacturing*. London: Springer London, 2009. doi: 10.1007/978-1-84882-287-0.

[6] N. M. Thoppil, V. Vasu, and C. S. P. Rao, “On the Criticality Analysis of Computer Numerical Control Lathe Subsystems for Predictive Maintenance,” *Arab J Sci Eng*, vol. 45, no. 7, pp. 5259–5271, 2020, doi: 10.1007/s13369-020-04397-7.

[7] H.-X. Chen, Y.-Q. Gong, Baosiriguleng, and W.-L. Qi, “Fuzzy FMECA for CNC machine tool spindle system,” *IOP Conf Ser Mater Sci Eng*, vol. 1043, no. 2, p. 022037, 2021, doi: 10.1088/1757-899x/1043/2/022037.

[8] C. V. Garzón, G. B. Moncayo, D. H. Alcantara, and R. Morales-Menendez, “Fault Detection in Spindles using Wavelets - State of the Art ∗,” Jan. 2018, vol. 51, no. 1, pp. 450–455. doi: 10.1016/j.ifacol.2018.05.075.

[9] Tedric A Harris and Michael N. Kotzalas, *Rolling Bearing Analysis, Essential Concepts of Bearing Technology*, 5th ed. Taylor & Francis Group, 2006.

[10] J. Ali Downtown, C. NSK Polska Sp oo, S. Africa, and S. NSK Spain, "MACHINE TOOL SPINDLE BEARING SELECTION & MOUNTING GUIDE," 2012. [Online]. Available: www.nskeurope.com

[11] P. Gupta and M. K. Pradhan, "Fault detection analysis in rolling element bearing: A review," 2017. [Online]. Available: www.sciencedirect.comwww.materialstoday.com/proceedings

[12] SKF Bearing Faults, "Bearing damage and failure analysis."

[13] M. Sartor and J. Guillot, "Calculation of the Stiffness Matrix of Angular Contact Ball Bearings by Using the Analytical Approach," 2000. [Online]. Available: http://asmedigitalcollection.asme.org/mechanicaldesign/article-pdf/122/1/83/5797094/83_1.pdf

[14] T. C. Lim and R. Singh, "VIBRATION TRANSMISSION THROUGH ROLLING ELEMENT BEARINGS, PART I: BEARING STIFFNESS FORMULATION," 1990.

[15] R. Aini, H. Rahnejat, and R. Gohar, "A FIVE DEGREES OF FREEDOM ANALYSIS OF VIBRATIONS IN PRECISION SPINDLES," 1990.

[16] Y. Kang, C. C. Huang, C. S. Lin, P. C. Shen, and Y. P. Chang, "Stiffness determination of angular-contact ball bearings by using neural network," *Tribol Int*, vol. 39, no. 6, pp. 461–469, Jun. 2006, doi: 10.1016/j.triboint.2005.02.005.

[17] Y. Guo and R. G. Parker, "Stiffness matrix calculation of rolling element bearings using a finite element/contact mechanics model," *Mech Mach Theory*, vol. 51, pp. 32–45, May 2012, doi: 10.1016/j.mechmachtheory.2011.12.006.

[18] D. Petersen, C. Howard, and Z. Prime, “Varying stiffness and load distributions in defective ball bearings: Analytical formulation and application to defect size estimation,” *J Sound Vib*, vol. 337, pp. 284–300, 2015, doi: 10.1016/j.jsv.2014.10.004.

[19] H. Xu, D. He, H. Ma, K. Yu, X. Zhao, and Y. Yang, “A method for calculating radial time-varying stiffness of flexible cylindrical roller bearings with localized defects,” *Eng Fail Anal*, vol. 128, Oct. 2021, doi: 10.1016/j.engfailanal.2021.105590.

[20] J. Liu, Y. Shao, and W. D. Zhu, “A new model for the relationship between vibration characteristics caused by the time-varying contact stiffness of a deep groove ball bearing and defect sizes,” *J Tribol*, vol. 137, no. 3, Jul. 2015, doi: 10.1115/1.4029461.

[21] D. Petersen, C. Howard, N. Sawalhi, A. Moazen Ahmadi, and S. Singh, “Analysis of bearing stiffness variations, contact forces and vibrations in radially loaded double row rolling element bearings with raceway defects,” *Mech Syst Signal Process*, vol. 50–51, pp. 139–160, 2015, doi: 10.1016/j.ymssp.2014.04.014.

[22] W. R. Wang, G. Student, and C. N. Chang, “Dynamic Analysis and Design of a Machine Tool Spindle-Bearing System,” 1994. [Online]. Available: http://asmedigitalcollection.asme.org/vibrationacoustics/article-pdf/116/3/280/5613749/280_1.pdf

[23] H. Li and Y. C. Shin, “Integrated dynamic thermo-mechanical modeling of high speed spindles, part 1: Model development,” *J Manuf Sci Eng*, vol. 126, no. 1, pp. 148–158, 2004, doi: 10.1115/1.1644545.

[24] Y. Cao and Y. Altintas, “Modeling of spindle-bearing and machine tool systems for virtual simulation of milling operations,” *Int J Mach Tools Manuf*, vol. 47, no. 9, pp. 1342–1350, Jul. 2007, doi: 10.1016/j.ijmachtools.2006.08.006.

[25] H. Cao, B. Li, and Z. He, “Finite element model updating of machine-tool spindle systems,” *Journal of Vibration and Acoustics, Transactions of the ASME*, vol. 135, no. 2, 2013, doi: 10.1115/1.4023045.

[26] H. Cao, L. Niu, and Z. He, “Method for vibration response simulation and sensor placement optimization of a machine tool spindle system with a bearing defect,” *Sensors (Switzerland)*, vol. 12, no. 7, pp. 8732–8754, Jul. 2012, doi: 10.3390/s120708732.

[27] S. Xi, H. Cao, X. Chen, and L. Niu, “Dynamic modeling of machine tool spindle bearing system and model based diagnosis of bearing fault caused by collision,” in *Procedia CIRP*, 2018, vol. 77, pp. 614–617. doi: 10.1016/j.procir.2018.08.197.

[28] C. K. Babu, N. Tandon, and R. K. Pandey, “Vibration modeling of a rigid rotor supported on the lubricated angular contact ball bearings considering six degrees of freedom and waviness on balls and races,” *Journal of Vibration and Acoustics, Transactions of the ASME*, vol. 134, no. 1, 2012, doi: 10.1115/1.4005140.

[29] S. Jiang and S. Zheng, “A modeling approach for analysis and improvement of spindle-drawbar-bearing assembly dynamics,” *Int J Mach Tools Manuf*, vol. 50, no. 1, pp. 131–142, Jan. 2010, doi: 10.1016/j.ijmachtools.2009.08.010.

[30] X. Zhang, Q. Han, Z. Peng, and F. Chu, “Stability analysis of a rotor-bearing system with time-varying bearing stiffness due to finite number of balls and unbalanced force,” *J Sound Vib*, vol. 332, no. 25, pp. 6768–6784, Dec. 2013, doi: 10.1016/j.jsv.2013.08.002.

[31] A. K. Rahman, R. Aini, and R. Gohar, “On the performance of multi-support spindle-bearing assemblies.”

[32] N. Lynagh, H. Rahnejat, M. Ebrahimi, and R. Aini, “Bearing induced vibration in precision high speed routing spindles,” 2000.

[33] M. Ritou, C. Rabréau, S. le Loch, B. Furet, and D. Dumur, “Influence of spindle condition on the dynamic behavior,” *CIRP Annals*, vol. 67, no. 1, pp. 419–422, Jan. 2018, doi: 10.1016/j.cirp.2018.03.007.

[34] C. W. Lin, Y. K. Lin, and C. H. Chu, “Dynamic models and design of spindle-bearing systems of machine tools: A review,” *International Journal of Precision Engineering and Manufacturing*, vol. 14, no. 3. SpringerOpen, pp. 513–521, Mar. 01, 2013. doi: 10.1007/s12541-013-0070-6.

[35] H. Cao, L. Niu, S. Xi, and X. Chen, “Mechanical model development of rolling bearing-rotor systems: A review,” *Mech Syst Signal Process*, vol. 102, pp. 37–58, 2018, doi: 10.1016/j.ymssp.2017.09.023.

[36] B. R. Jorgensen Graduate Research Assistant and Y. C. Shin Professor, “Dynamics of Spindle-Bearing Systems at High Speeds Including Cutting Load Effects,” 1998. [Online]. Available: http://www.asme.org/about-asme/terms-of-use

[37] F. M. A. El-Saeidy, “Time-varying total stiffness matrix of a rigid machine spindle-angular contact ball bearings assembly: Theory and analytical/experimental verifications,” *Shock and Vibration*, vol. 18, no. 5, pp. 641–670, 2011, doi: 10.3233/SAV-2010-0577.

[38] S. Saravanan, G. S. Yadava, and P. v. Rao, “Condition monitoring studies on spindle bearing of a lathe,” *International Journal of Advanced Manufacturing Technology*, vol. 28, no. 9, pp. 993–1005, Apr. 2006, doi: 10.1007/s00170-004-2449-0.

[39] H. D. M. de Azevedo, A. M. Araújo, and N. Bouchonneau, “A review of wind turbine bearing condition monitoring: State of the art and challenges,” *Renewable and Sustainable Energy Reviews*, vol. 56. Elsevier Ltd, pp. 368–379, Apr. 01, 2016. doi: 10.1016/j.rser.2015.11.032.

[40] D. S. Shah and V. N. Patel, “A Review of Dynamic Modeling and Fault Identifications Methods for Rolling Element Bearing,” *Procedia Technology*, vol. 14, pp. 447–456, 2014, doi: 10.1016/j.protcy.2014.08.057.

[41] P. P. Kharche Sharad V Kshirsagar PG Student Guide and A. Professor, “IJIRAE::Review of Fault Detection in Rolling Element Bearing Vibrat ional Analysis in Condit ion Monit oring and fault s Diagnosis of Rot at ing Shaft-Over View IJAERS Journal An Overview on Vibrat ion Analysis Techniques for t he Diagnosis of Rolling Element Bearing Fault s Review of Fault Detection in Rolling Element Bearing,” 2014.

[42] A. Kumar and R. Kumar, “Role of Signal Processing, Modeling and Decision Making in the Diagnosis of Rolling Element Bearing Defect: A Review,” *Journal of Nondestructive Evaluation*, vol. 38, no. 1. Springer Science and Business Media, LLC, Mar. 01, 2019. doi: 10.1007/s10921-018-0543-8.

[43] P. H. Jain and S. P. Bhosle, “A Review on Vibration Signal Analysis Techniques Used for Detection of Rolling Element Bearing Defects,” *International Journal of Mechanical Engineering*, vol. 8, no. 1, pp. 14–29, Jan. 2021, doi: 10.14445/23488360/ijme-v8i1p103.

[44] N. I. Azeez and A. C. Alex, “Detection of rolling element bearing defects by vibration signature analysis: A review,” in *2014 Annual International Conference on Emerging Research Areas: Magnetics, Machines and Drives, AICERA/iCMMD 2014 - Proceedings*, Sep. 2014. doi: 10.1109/AICERA.2014.6908270.

[45] D. Dyer and R. M. Stewart, “Detection of Rolling Element Bearing Damage by Statistical Vibration Analysis,” 1978. [Online]. Available: https://mechanicaldesign.asmedigitalcollection.asme.org

[46] Y. Shao and K. Nezu, “15 A-2 Bearing Fault Detection Using Laser Displacement Sensor.”

[47] IEEE Region 10. Colloquium (3rd : 2008 : Indian Institute of Technology Kharagpur), Institute of Electrical and Electronics Engineers. Kharagpur Section., IEEE Sri Lanka Section., and Damodar Valley Corporation., *IEEE Region 10 Colloquium and Third International Conference on Industrial and Information Systems : ICIIS-2008, December 8-10, 2008 : theme: "Real-time communicative intelligence for tomorrow's industry" : e-proceedings*. IEEE, 2008.

[48] O. G. Gustafsson and T. Tallian, "Detection of damage in assembled rolling element bearings," *ASLE Transactions*, vol. 5, no. 1, pp. 197–209, 1962, doi: 10.1080/05698196208972466.

[49] J. I. Taylor, "Identification of Bearing Defects by Spectral Analysis," 1980. [Online]. Available: http://www.asme.org/about-asme/terms-of-use

[50] D. W. Thomas, "Effect of Inter-Modulation and Quasi-Periodic Instability in the Diagnosis of Rolling Element Incipient Defect," 1982. [Online]. Available: http://www.asme.org/

[51] L. Niu, H. Cao, Z. He, and Y. Li, "A systematic study of ball passing frequencies based on dynamic modeling of rolling ball bearings with localized surface defects," *J Sound Vib*, vol. 357, pp. 207–232, Nov. 2015, doi: 10.1016/j.jsv.2015.08.002.

[52] S. Braun and B. Datner, "Analysis of Roller/Ball Bearing Vibrations," 1979. [Online]. Available: http://www.asme.org/about-asme/terms-of-use

[53] P. D. Mcfadden and J. D. Smith, "Vibration monitoring of rolling element bearings by the high-frequency resonance technique a review," 1984.

[54] K. F. Martin and P. Thorpe, "Normalised spectra in monitoring of rolling bearing elements," 1992.

[55] O. Rioul and M. Vetierli, "~ velets and Signal Processing," no. October, pp. 14–38, 1991, doi: 10.1109/79.91217.

[56] Z. K. Peng and F. L. Chu, “Application of the wavelet transform in machine condition monitoring and fault diagnostics : a review with bibliography,” vol. 18, pp. 199–221, 2004, doi: 10.1016/S0888-3270(03)00075-X.

[57] K. Mori, N. Kasashima, T. Yoshioka, and Y. Ueno, “Prediction of spalling on a ball bearing by applying the discrete wavelet transform to vibration signals,” 1996.

[58] B. Liu, S. F. Ling, and Q. Meng, “Machinery diagnosis based on wavelet packets,” *JVC/Journal of Vibration and Control*, vol. 3, no. 1, pp. 5–17, 1997, doi: 10.1177/107754639700300102.

[59] B. A. P and I. I. E, “ARTIFICIAL NEURAL NETWORK BASED FAULT DIAGNOSTICS OF ROTATING MACHINERY USING WAVELET TRANSFORMS AS A PREPROCESSOR,” 1997.

[60] N. G. Nikolaou and I. A. Antoniadis, “Rolling element bearing fault diagnosis using wavelet packets.” [Online]. Available: www.elsevier.com/locate/ndteint

[61] C. J. Li and J. Ma, “Wavelet decomposition of vibrations for detection of bearing-localized defects,” *NDT and E International*, vol. 30, no. 3, pp. 143–149, 1997, doi: 10.1016/s0963-8695(96)00052-7.

[62] S. Prabhakar, A. R. Mohanty, and A. S. Sekhar, “Application of discrete wavelet transform for detection of ball bearing race faults,” 2002. [Online]. Available: www.elsevier.com/locate/triboint

[63] D. F. Shi, W. J. Wang, and L. S. Qu, “Defect detection for bearings using envelope spectra of wavelet transform,” *Journal of Vibration and Acoustics, Transactions of the ASME*, vol. 126, no. 4, pp. 567–573, Oct. 2004, doi: 10.1115/1.1804995.

[64] L. Zhang, R. X. Gao, and K. B. Lee, “Spindle health diagnosis based on analytic wavelet enveloping,” *IEEE Trans Instrum Meas*, vol. 55, no. 5, pp. 1850–1858, Oct. 2006, doi: 10.1109/TIM.2006.880261.

[65] C. Wang and R. X. Gao, “Wavelet transform with spectral post-processing for enhanced feature extraction,” in *Conference Record - IEEE Instrumentation and Measurement Technology Conference*, 2002, vol. 1, pp. 315–320. doi: 10.1109/imtc.2002.1006860.

[66] Z. K. Zhu, R. Yan, L. Luo, Z. H. Feng, and F. R. Kong, “Detection of signal transients based on wavelet and statistics for machine fault diagnosis,” *Mech Syst Signal Process*, vol. 23, no. 4, pp. 1076–1097, May 2009, doi: 10.1016/j.ymssp.2008.06.012.

[67] R. Yan and R. X. Gao, “An efficient approach to machine health diagnosis based on harmonic wavelet packet transform,” in *Robotics and Computer-Integrated Manufacturing*, Aug. 2005, vol. 21, no. 4–5, pp. 291–301. doi: 10.1016/j.rcim.2004.10.005.

[68] C. K. E. Nizwan, S. A. Ong, M. F. M. Yusof, and M. Z. Baharom, “A wavelet decomposition analysis of vibration signal for bearing fault detection,” *IOP Conf Ser Mater Sci Eng*, vol. 50, no. 1, 2013, doi: 10.1088/1757-899X/50/1/012026.

[69] P. K. Kankar, S. C. Sharma, and S. P. Harsha, “Rolling element bearing fault diagnosis using wavelet transform,” *Neurocomputing*, vol. 74, no. 10, pp. 1638–1645, May 2011, doi: 10.1016/j.neucom.2011.01.021.

[70] R. Kumar and M. Singh, “Outer race defect width measurement in taper roller bearing using discrete wavelet transform of vibration signal,” *Measurement (Lond)*, vol. 46, no. 1, pp. 537–545, 2013, doi: 10.1016/j.measurement.2012.08.012.

[71] H. Cheng, Y. Zhang, W. Lu, and Z. Yang, “Effect of boundary position and defect shape on the mechanical properties of ball bearings,” *Mechanics Based*

Design of Structures and Machines, 2021, doi: 10.1080/15397734.2021.1875329.

[72] H. V. Liew and T. C. Lim, "Analysis of time-varying rolling element bearing characteristics," *J Sound Vib*, vol. 283, no. 3–5, pp. 1163–1179, May 2005, doi: 10.1016/j.jsv.2004.06.022.

[73] B. J. Schwarz and M. H. Richardson, "EXPERIMENTAL MODAL ANALYSIS," 1999.

[74] C. K. Mechefske, "Machine Condition Monitoring and Fault Diagnostics."

[75] T. Karacay and N. Akturk, "Experimental diagnostics of ball bearings using statistical and spectral methods," *Tribol Int*, vol. 42, no. 6, pp. 836–843, Jun. 2009, doi: 10.1016/j.triboint.2008.11.003.

[76] Y. Wang, J. Xiang, R. Markert, and M. Liang, "Spectral kurtosis for fault detection, diagnosis and prognostics of rotating machines: A review with applications," *Mechanical Systems and Signal Processing*, vol. 66–67. Academic Press, pp. 679–698, 2016. doi: 10.1016/j.ymssp.2015.04.039.

[77] ISO 10816-3, "Mechanical vibration-Evaluation of machine vibration by measurements on non-rotating parts," 1998.

[78] ISO/TR 17243-1, "Machine tool spindles — Evaluation of machine tool spindle vibrations by measurements on spindle housing — Part 1: Spindles with rolling element bearings and integral drives operating at speeds between 600 min-1 and 30 000 min-1," 2014.

[79] P. W. Tse, "Wavelet Analysis and Envelope Detection For Rolling Element Bearing Fault Diagnosis — Their Effectiveness and Flexibilities," vol. 123, no. July, pp. 303–310, 2001, doi: 10.1115/1.1379745.

[80] A. A. Roque, T. A. N. Silva, J. M. F. Calado, and J. C. Q. Dias, "An approach to fault diagnosis of rolling bearings," *WSEAS Transactions on Systems and Control*, vol. 4, no. 4, pp. 188–197, 2009.

[81] J. Mais, “Spectrum Analysis The key features of analyzing spectra.”